Scuola Dottorale in Scienze Matematiche e Fisiche

XXVIII Ciclo di Dottorato

Study of $(W/Z)H$ production using $H \rightarrow WW^*$ decays with the ATLAS detector at LHC

Candidato:

Daniele Puddu ______________ *firma*

Docente Guida:

Prof.ssa Domizia Orestano ______________ *firma*

Coordinatore:

Prof. Roberto Raimondi ______________ *firma*

Un bel dì, vedremo
levarsi un fil di fumo
dall'estremo confin del mare.
E poi la nave appare.
Poi la nave bianca
entra nel porto,
romba il suo saluto.

Madama Butterfly, G. Puccini

UNIVERSITÀ DEGLI STUDI ROMA TRE

Abstract

Dipartimento di Matematica e Fisica Roma Tre

Doctor of Philosophy

Study of $(W/Z)H$ production using $H\to WW^{*}$ decays with the ATLAS detector at LHC

by Daniele Puddu

A search for the Higgs boson associated production modes WH and ZH is performed in the Higgs boson decay channel $H\to WW^{*}$, with the data collected by the ATLAS experiment at the LHC in 2011 and 2012, at $\sqrt{s} = 7$ TeV and 8 TeV, respectively. For the WH associated production the three-leptons final state, in which three W bosons decay to leptons, and two-leptons final state, in which one W boson decays to hadrons, are studied. The four-leptons final state is used to search for the ZH production.

Introduction

The Standard Model describes the interactions at microscopic level between the subatomic particles: strong, weak and electromagnetic. Among the successes of this theory we can recall the prediction of the existence of vector bosons W and Z and of the Higgs boson recently observed. Open issues still remain uncovered, theories beyond Standard Model have been developed to address them and particle interactions at high energies are explored to test their prediction or to observe unexpected effects.
The Large Hadron Collider (LHC) is the largest and most powerful particle accelerator ever built, thanks to the highest design energy in the centre-of-mass, 14 TeV, and thanks to the high design luminosity, 10^{34} cm^{-2}s^{-1}, it allows to investigate very rare processes and new phenomena.
ATLAS is one of the two multi-purpose detectors installed at LHC, its capability to measure precisely the particles produced in a collision, even in the challenging high luminosity environment, led to announce on 4 July 2012, together with the CMS Experiment, the discovery of the Higgs boson.
The properties of the Higgs boson are still under investigation. Increasing the precision of the measurements will allow stringent tests of the Standard Model and will provide constraints on New Physics.
In this thesis Higgs boson production in association with a W or Z boson, followed by $H \to WW^*$ decay, is searched for using events with two, three or four charged leptons (electrons and muons) in the final state, collected by ATLAS during Run-1.

This dissertation is organised as follows. In Chapter 1 the Higgs boson is described in the context of the Standard Model, in Chapter 2 the LHC complex and the ATLAS detector with its sub-detectors are introduced. The objects used in the analysis are described in Chapter 3 and the analysis is explained in Chapter 4. The entire Chapter 5 is devoted to the results and to the statistical tools employed in the analysis. The current developing analysis for the Run-2 of LHC is then presented in Chapter 6. Finally Chapter 7 summarises the conclusions.

Contents

Physical constants, units and definitions

Planck constant, reduced	$\hbar$	$=$	$1.054\ 571\ 628(53) \times 10^{-34}$ J s
			or $6.582\ 118\ 99(16) \times 10^{-22}$ MeV s
Speed of Light	c	$=$	$2.997\ 924\ 58 \times 10^{8}$ ms^{-1} (exact)
Natural Units (widely used in HEP)			$\hbar \equiv c \equiv 1$
Fermi coupling constant	G_{F}	$=$	$1.166\ 364(5) \times 10^{-5}$ GeV^{-2}
Z boson mass	$m_{\mathbf{Z}}$	$=$	$91.1876(21)$ GeV
Cross Section	barn	$=$	$10^{-28}\mathrm{m}^2$
Fermi	fm	$=$	$10^{-15}\mathrm{m}$
Momentum of the particle	$\mathbf{p}$	$=$	$(p_{\mathrm{x}}, p_{\mathrm{y}}, p_{\mathrm{z}})$[1]
Transverse Momentum	p_{T}	$=$	$\sqrt{\mathbf{p}^2 - p_{\mathrm{z}}^2}$
Rapidity	y	$=$	$\frac{1}{2}\ln\left(\frac{E+p_{\mathrm{z}}}{E-p_{\mathrm{z}}}\right)$
Pseudorapidity	η	$=$	$-\ln\left[\tan\left(\frac{\theta}{2}\right)\right]$ or $\frac{1}{2}\ln\left(\frac{\lvert\mathbf{p}\rvert+p_{\mathrm{z}}}{\lvert\mathbf{p}\rvert-p_{\mathrm{z}}}\right)$
	$\mathbf{\Delta R}$	$=$	$\sqrt{\Delta^2\eta + \Delta^2\phi}$
Significance (used in cutflow tables)		$=$	$\sqrt{2((s+b)\ln(1+\frac{s}{b}) - s)}$

[1]The beam direction defines the z-axis, and the x-y plane is the plane transverse to the beam direction. The positive x-axis is defined as pointing from the interaction point to the centre of the LHC ring, and the positive y-axis is pointing upwards. The azimuthal angle ϕ is measured around the beam axis, and the polar angle θ is the angle from the beam axis.

Dedicated to Antonietta

Chapter 1

The Higgs boson and the Standard Model

Among the questions disturbing the sleep of mankind such as “Why are we here?” or “What is the destiny of the world?” or “Will I be in time at work tomorrow?”... we can find also “What is the world made of?” and “How these things interact between them?”. Finding an answer to these questions is sometime impossible[1] but some other time we can investigate and find something that could satisfy our curiosity as much as possible.

The Standard Model (SM) of Particle Physics has been tested in the second half of the 20th century, and it is nowadays the most complete and confirmed theory that explains what is the matter made of and how the nature behaves at short distances. Unresolved issues still remain and more general Theories Beyond the SM (BSM) have been developed to address the open questions, but no experimental confirmation has been found up to now.

An overview of the SM and a brief look at the critical aspects will be given in this Chapter.

1.1 Particle physics phenomenology

At microscopic level three fundamental forces govern the interactions, these are called *strong*, *electromagnetic*, and *weak* [1, 2, 3]. We can see a manifestation of electromagnetic force everywhere light is present. Deeper into the atomic structure, the repulsive electromagnetic force between protons is overcome by strong interaction and the existence

[1] I'm in time at work! At least today.

of the nuclei is then permitted. The weak force causes for example the beta radioactivity of some nuclei. In Tab. 1.1 the main properties of these interactions are summarised, such as the range of interaction; the typical lifetime when a decay process occurs; the cross section of interaction and the coupling constant.

Interaction	Range (m)	Typical Lifetime (sec)	Typical Cross Section (mb)	Typical Coupling α_i
Strong	10^{-15}	10^{-23}	10	1
Electromagnetic	∞	$10^{-20} - 10^{-16}$	10^{-3}	10^{-2}
Weak	10^{-18}	10^{-12}	10^{-11}	10^{-6}

TABLE 1.1: Main properties of the SM interactions.

In the picture of the SM the bricks of the matter are half-integer spin particles (fermions) divided into three families of coloured quarks (Sec. 1.2.1) and three families of colourless leptons (Tab. 1.2). Strong interactions are possible only between quarks and gluons. Forces are mediated by bosons (integer-spin): eight massless gluons coloured for the strong interaction, three massive vector bosons for the weak interaction and the massless photon for the electromagnetic interaction. The Higgs boson is the particle that confirms the mechanism responsible for the existence of the masses.

1.2 The Standard Model: a gauge theory

The natural context where interactions between particles could be described is relativistic quantum field theory [6], taking into account

- space–time symmetry in terms of Lorentz invariance, as well as internal symmetries like gauge symmetries,
- causality,
- local interactions.

Each particle is described by a field:

- spin-0 particles, described by scalar fields $\phi(x)$;
- spin-1 particles, described by vector fields $A_\mu(x)$;
- spin-1/2 fermions, described by spinor fields $\psi(x)$.

			Name	Symbol	Charge $[e]$	Mass
Fermions	**Leptons**	$J^P = 1/2^+$	Electron neutrino	ν_e	0	< 2 eV
			Electron	e	-1	0.511 MeV
			Muon neutrino	ν_μ	0	< 0.19 MeV
			Muon	μ	-1	105.7 MeV
			Tau neutrino	τ_ν	0	< 18.2 MeV
			Tau	τ	-1	1.777 GeV
	Quarks	$J^P = 1/2^+$	Up	u	$+2/3$	$2.3^{\pm 0.7}_{-0.5}$ MeV
			Down	d	$-1/3$	$4.8^{\pm 0.5}_{-0.3}$ MeV
			Charm	c	$+2/3$	1.275 ± 0.025 GeV
			Strange	s	$-1/3$	95 ± 5 MeV
			Top	t	$+2/3$	173.21 ± 0.87 GeV
			Bottom	b	$-1/3$	4.18 ± 0.03 GeV
Bosons	**Vector**	$J^P = 1^-$	Gluon	g	0	0
			Photon	γ	0	$< 1 \times 10^{-18}$ eV
			W boson	$W^\pm$	± 1	80.385 ± 0.015 GeV
			Z boson	Z	0	91.1876 ± 0.0021 GeV
	Scalar	$J^P = 0^+$	Higgs boson	H	0	125.7 ± 0.4 GeV

TABLE 1.2: Particles of the Standard Model. J denotes the spin and P the parity of the particle. The masses are taken from Ref. [4], the table from Ref. [5]. The uncertainties for the charged lepton masses are below 0.01%.

The global Lagrangian must respect the $SU(3)_C \times SU(2)_L \times U(1)_Y$ symmetry, $SU(3)_C$ is associated to Quantum-Chromodynamics (QCD) colour symmetry, $SU(2)_L$ to the weak isospin symmetry, and $U(1)_Y$ is the hypercharge symmetry. In the framework of the SM, classical electrodynamics [7] is a limit of Quantum Electrodynamics (QED), for small momentum and energy transfers and large average numbers of virtual or real photons. Quantum electrodynamics, in turn, is a consequence of a spontaneously broken symmetry in a theory in which initially the weak and electromagnetic interactions are unified and the force carriers of both are massless. The symmetry breaking leaves the electromagnetic force carrier (photon) massless with a Coulomb's law of infinite range, while the weak force carriers acquire masses of the order of $80 - 90$ GeV with a weak interaction at low energies of extremely short range.

Because of the origins in a unified theory, the range and strength of the weak interaction are related to the electromagnetic coupling. Despite the presence of a rather large number of quantities that must be taken from experiments, the SM (together with general relativity at large scales) provides a highly accurate description of nature in all its aspects, from far inside the nucleus, to microelectronics, to tables and chairs, to the most remote galaxy. Many of the phenomena are classical or explicable with non-relativistic quantum mechanics, of course, but the precision of the agreement of the SM with experiment in atomic and particle physics where relativistic quantum mechanics rules is truly astounding.

1.2.1 Quantum Chromodynamics

QCD is the theory describing the strong force, which acts on colour-charged particles, mediated by gluons [2, 3, 8]. The QCD theory of strong interactions is an unbroken gauge theory based on the group $SU(3)$ of colour. The eight massless gauge bosons are the gluons g_μ^A and the matter fields are colour triplets of quarks q_i^a (in different flavours i). Quarks and gluons are the only fundamental fields of the Standard Model with strong interactions (hadrons).
The statement that QCD is a gauge theory based on the group $SU(3)$ with colour triplet quark matter fields fixes the QCD lagrangian density to be:

$$\mathcal{L}_{\mathrm{QCD}} = -\frac{1}{4}\sum_{A=1}^{8} F^{A\mu\nu}F^{A}_{\mu\nu} + \sum_{j=1}^{n_{\mathrm{f}}} \bar{q}_j(i\not{D} - m_j)q_j, \tag{1.1}$$

where q_j are the quark fields (of n_{f} different flavours) with mass m_j; $\not{D} = D_\mu\gamma^\mu$ and γ^μ are the Dirac matrices and D_μ is the covariant derivative:

$$D_\mu = \partial_\mu - \imath e_s \sum_{A=1}^{8} t^A g_\mu^A; \tag{1.2}$$

e_s is the gauge coupling in analogy with QED:

$$\alpha_s = \frac{e_s^2}{4\pi}, \tag{1.3}$$

A are the gluon fields and t^A are the $SU(3)$ group generators in the triplet representation of quarks (i.e. t_A are 3x3 matrices acting on q); the generators obey the commutation relations $[t^A, t^B] = iC_{ABC}t^C$ where C_{ABC} are the complete anti-symmetric structure constants of $SU(3)$ (the normalisation of C_{ABC} and of e_s is specified by $Tr[t^A t^B] = \delta^{AB}/2$);

$$F^A_{\mu\nu} = \partial_\mu g^A_\nu - \partial_\nu g^A_\mu - e_s C_{ABC} g^B_\mu g^C_\nu \tag{1.4}$$

An interesting property of the strong interaction is the confinement: no isolated coloured charge can exist but only colour singlet particles [8, 9]. The strong potential has the form:

$$V(r) \approx -\frac{4}{3}\frac{\alpha_s}{r} + kr \text{ with } k \approx 1 \text{ GeV/fm}. \tag{1.5}$$

The linear term prevents the separation of two quarks. Increasing the distance leads to the creation of $q\bar{q}$ pqirs in a more stable energetic configuration.
Another interesting property of the strong interaction is the "asymptotic" freedom. The coupling of the interaction (α_s) depends on the energy (q^2) of the interactions following the relation:

$$\alpha_s(q^2) = \frac{12\pi}{(33 - 2n_f)\ln(q^2/\Lambda^2_{QCD})}, \tag{1.6}$$

where Λ_{QCD} is the typical energy scale of the strong interaction and n_f the number of quarks with mass up to $\sqrt{q^2}$. At high energy a perturbative treatment of the strong interaction is possible.
The proton is a bound state of quarks and gluons, the total momentum of the proton is shared among its constituents [10]. Cross sections of processes depend on the parton distribution functions (PDF), describing the probability in a hard interaction at a scale μ^2 to find a parton of a particular flavour with x fraction of the momentum of the proton. Fig. 1.1 shows the PDF (multiplyed by x) for quarks and gluons at $\mu^2 = 10$ GeV^2 (a) and at $\mu^2 = 10^2$ GeV^2 (b).

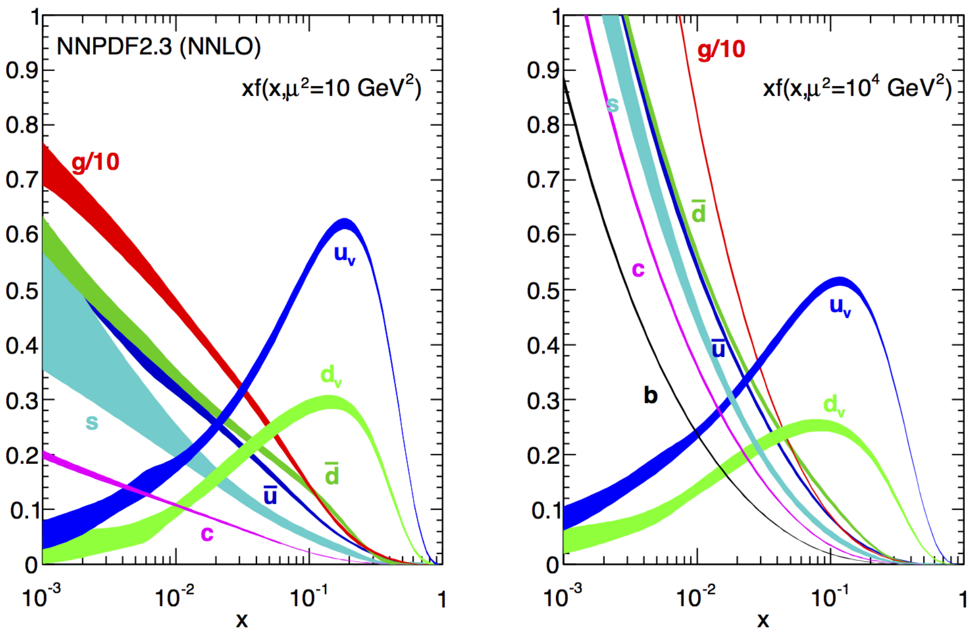

FIGURE 1.1: Fraction of energy x carried by the parton times the parton distribution function $f(x;\mu^2)$ for protons at scales $\mu^2 = 10$ GeV^2 and 10^4 GeV^2 [10, 11].

1.2.2 The Electroweak Standard Model

It is possible to group the fermions families of leptons and quarks into left-handed doublets and right-handed singlets under $SU(2)_L \times U(1)_Y$ transformation (Tab. 1.3).

	Left	Right
Leptons	$\begin{pmatrix} e \\ \nu_e \end{pmatrix}_L, \begin{pmatrix} \mu \\ \nu_\mu \end{pmatrix}_L, \begin{pmatrix} \tau \\ \nu_\tau \end{pmatrix}_L$	e_R, μ_R, τ_R
Quarks	$\begin{pmatrix} u \\ d \end{pmatrix}_L, \begin{pmatrix} c \\ s \end{pmatrix}_L, \begin{pmatrix} t \\ b \end{pmatrix}_L$	$u_R, d_R, c_R, s_R, t_R, b_R$

TABLE 1.3: Fields of the fermions of the Standard Model.

A classification is possible using the weak isospin (t, t^3) and the hypercharge (Y). These quantum numbers are related to the electric charge according to the Gell-Mann-Nishijima formula that is the same for left-hand and right-hand components:

$$Q = t^3 + \frac{Y}{2}, \tag{1.7}$$

where t^3 is the third component of isospin.

	ν_L	e_L	e_R	u_L	d_L	u_R	d_R
t^3	+1/2	-1/2	0	+1/2	-1/2	0	0
Y	-1	-1	-2	+1/3	+1/3	+4/3	-2/3
Q	0	-1	-1	+2/3	-1/3	+2/3	-1/3

TABLE 1.4: Fermionic fields classification: t, t^3, Y

Since the first observations it was clear that massless vector bosons were strongly discouraged by the experimental measurements [12], the Englert-Brout-Higgs [13, 14, 15, 16] mechanism was introduced in the framework of SM in order to explain the masses of the particles, including the vector bosons as well. It is possible to express the electroweak (EW) Lagrangian as the sum of two terms [17]:

$$\mathcal{L} = \mathcal{L}_{\text{gauge}} + \mathcal{L}_{\text{Higgs}}, \tag{1.8}$$

where the Higgs term is responsible for the non vanishing masses of vector bosons and fermions.

The gauge sector describes the interactions among fermions and gauge bosons:

$$\mathcal{L}_{\text{gauge}} = -\frac{1}{4}\sum_{A=1}^{3} \boldsymbol{F}^{A}_{\mu\nu}\boldsymbol{F}^{A\mu\nu} - \frac{1}{4}\boldsymbol{B}_{\mu\nu}\boldsymbol{B}^{\mu\nu} + \bar{\psi}_L \imath\boldsymbol{\gamma}^{\mu}\boldsymbol{D}_{\mu}\psi_L + \bar{\psi}_R \imath\boldsymbol{\gamma}^{\mu}\boldsymbol{D}_{\mu}\psi_R, \tag{1.9}$$

where $\boldsymbol{B}_{\mu\nu} = \partial_\mu \boldsymbol{B}_\nu - \partial_\nu \boldsymbol{B}_\mu$ and $\boldsymbol{F}^A_{\mu\nu} = \partial_\mu \boldsymbol{W}^A_\nu - \partial_\nu \boldsymbol{W}^A_\mu - g\varepsilon_{ABC}\boldsymbol{W}^B_\mu \boldsymbol{W}^C_\nu$ are the gauge anti-symmetric tensors constructed out of the gauge field $\boldsymbol{B}_\mu$ associated with $U(1)$, and $\boldsymbol{W}^A_\mu$ corresponding to the three $SU(2)$ generators, ε_{ABC} are the group structure constants for $SU(2)$, g is the gauge coupling.

The fermion fields are described through their left-hand and right-hand components:

$$\psi_{L,R} = [(1 \mp \gamma_5)/2]\psi, \quad \bar{\psi}_{L,R} = \bar{\psi}[(1 \pm \gamma_5)/2];$$

with γ_5 and other Dirac matrices defined as in Ref. [18]. The standard EW theory is a chiral theory, in the sense that ψ_L and ψ_R behave differently under the gauge group (so that parity and charge conjugation non conservation are made possible in principle). Thus, mass terms for fermions (of the form $\bar{\psi}_L\psi_R + \text{h.c.}$) are forbidden in the symmetric limit. In the absence of mass terms, there are only vector and axial vector interactions in the Lagrangian and those have the property of not mixing ψ_L and ψ_R. The covariant derivatives $D_\mu\psi_{L,R}$ are explicitly given by

$$D_\mu\psi_{L,R} = [\partial_\mu + \imath g\sum_{A=1}^{3} t^A_{L,R}\boldsymbol{W}^A_\mu + \imath g'\frac{1}{2}Y_{L,R}\boldsymbol{B}_\mu]\psi_{L,R} \tag{1.10}$$

where $t^A_{L,R}$ and $\frac{1}{2}Y_{L,R}$ are the $SU(2)$ and $U(1)$ generators, respectively and g' is again a gauge coupling. Note that $t^i_R\psi_R = 0$, given that, for all known quark and leptons, ψ_R is a singlet.

All fermion couplings of the gauge bosons can be derived directly from Eq. 1.9 and Eq. 1.10. The charged $\boldsymbol{W}_\mu$ fields are described by $\boldsymbol{W}^{1,2}_\mu$, while the photon $\boldsymbol{A}_\mu$ and weak neutral gauge boson $\boldsymbol{Z}_\mu$ are obtained from combinations of $\boldsymbol{W}^3_\mu$ and $\boldsymbol{B}_\mu$. The $\boldsymbol{W}^{1,2}_\mu$ terms in Eq. 1.9 and Eq. 1.10 can be written as:

$$g(t^1\boldsymbol{W}^1_\mu + t^2\boldsymbol{W}^2_\mu) = g\{[(t^+\boldsymbol{W}^-_\mu)/2] + \text{h.c.}\}, \tag{1.11}$$

where $t^\pm = t^1 \pm \imath t^2$ and $\boldsymbol{W}^\pm = (\boldsymbol{W}^1 \pm \imath\boldsymbol{W}^2)/\sqrt{2}$.

By applying this generic relation to L and R fermions separately, the vertex $V_{\bar{\psi}\psi\boldsymbol{W}}$ is described by:

$$V_{\bar{\psi}\psi\boldsymbol{W}} = g\bar{\psi}\gamma_\mu[(t^+_L/\sqrt{2})(1-\gamma_5)/2) + (t^+_R/\sqrt{2})(1-\gamma_5)/2)]\psi\boldsymbol{W}^-_\mu + \text{h.c.} \tag{1.12}$$

As a consequence of $t_R = 0$ being null in the SM, the charged current is pure $V - A$.

On the other hand, in the neutral-current sector, the physical fields associated to the photon ($\boldsymbol{A}_\mu$) and the one associated the neutral weak boson ($\boldsymbol{Z}_\mu$) are orthogonal and are normalised linear combinations of $\boldsymbol{B}_\mu$ and $\boldsymbol{W}^3_\mu$:

$$\begin{aligned} \boldsymbol{A}_\mu &= \cos\theta_W \boldsymbol{B}_\mu + \sin\theta_W \boldsymbol{W}^3_\mu, \\ \boldsymbol{Z}_\mu &= -\sin\theta_W \boldsymbol{B}_\mu + \cos\theta_W \boldsymbol{W}^3_\mu, \end{aligned} \tag{1.13}$$

where θ_W is the weak mixing angle.
Using Eq. 1.9, Eq. 1.10 and Eq. 1.7 it is possible to write:

$$\begin{aligned} gt^3\boldsymbol{W}^3_\mu + g'Y/2\boldsymbol{B}\mu = \quad & [gt^3\sin\theta_W + g'(Q-t^3)\cos\theta_W]\boldsymbol{A}_\mu + \\ & +[gt^3\cos\theta_W - g'(Q-t^3)\sin\theta_W]\boldsymbol{Z}_\mu. \end{aligned} \tag{1.14}$$

In order to preserve the classical behaviour, i.e. same coupling of the photon field to L and R component driven by the charge of the fermionic field, it is straightforward to impose:

$$g\sin\theta_W = g'\cos\theta_W = e \quad \text{and} \quad \mathrm{tg}\theta_W = g'/g. \tag{1.15}$$

Using Eq. 1.15 the $\boldsymbol{Z}$ vertex ($V_{\bar{\psi}\psi\boldsymbol{Z}}$) becomes:

$$V_{\bar{\psi}\psi\boldsymbol{Z}} = \frac{g}{2\cos\theta_W}\bar{\psi}\gamma_\mu[t^3_L(1-\gamma_5) + t^3_R(1+\gamma_5) - 2Q\sin^2\theta_W]\psi\boldsymbol{Z}^\mu. \tag{1.16}$$

The Higgs Lagrangian ($\mathcal{L}_{\text{Higgs}}$) is responsible for the spontaneous symmetry breaking and the masses of particles:

$$\mathcal{L}_{\text{Higgs}} = (D_\mu\phi)^\dagger(D^\mu\phi) - V(\phi^\dagger\phi) - \bar{\psi}_L\Gamma\psi_R\phi - \bar{\psi}_R\Gamma\psi_L\phi \tag{1.17}$$

where ϕ is a column vector including all Higgs fields; it transforms as a reducible representation of the gauge group. The quantities Γ (which include all coupling constants) are matrices that make the Yukawa couplings invariant under the Lorentz and gauge groups. The Higgs field can be written in the form:

$$\phi(x) = \begin{pmatrix} \phi^+(x) \\ \phi^0(x) \end{pmatrix} = \begin{pmatrix} \phi_1(x) + \imath\phi_2(x) \\ \phi_3(x) + \imath\phi_4(x) \end{pmatrix}. \tag{1.18}$$

The potential $V(\phi^\dagger\phi)$, symmetric under $SU(2)\times U(1)$, contains, at most, quartic terms in ϕ so that the theory is renormalisable:

$$V(\phi^\dagger\phi) = -\mu^2\phi^\dagger\phi + \frac{1}{2}\lambda(\phi^\dagger\phi)^2, \tag{1.19}$$

where μ^2 and λ are constants. The potential has a parabolic shape for $\mu^2 > 0$, while it asseumes the shape of a Mexican hat for $\mu^2 < 0$, as pictured in Fig. 1.2, which is minimised by all non-vanishing field configurations with $\phi^\dagger\phi = 2\mu^2/\lambda$. In this case the

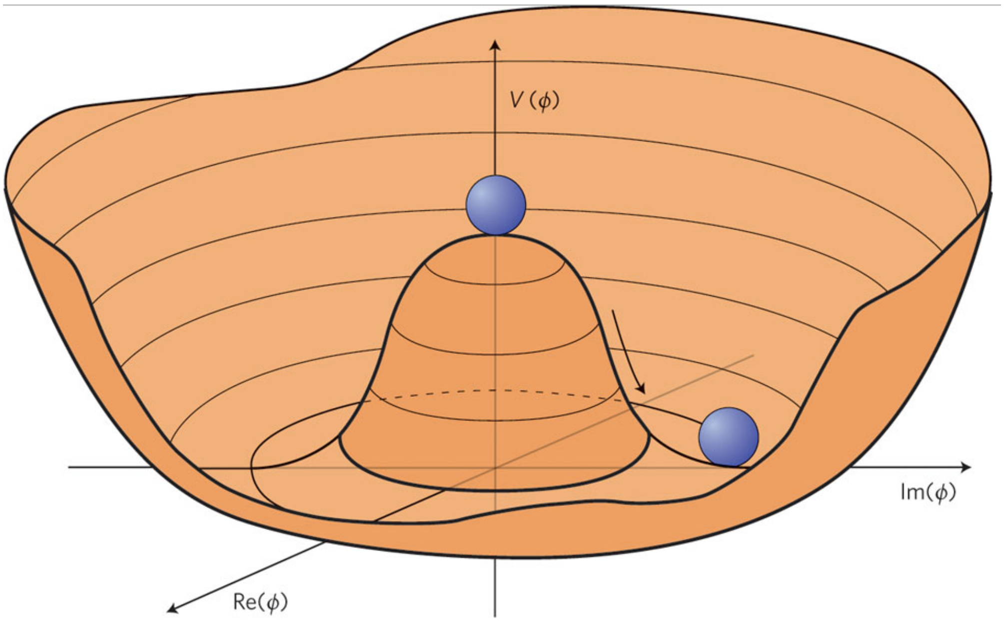

FIGURE 1.2: Shape of the Higgs potential for $\mu^2 < 0$ [19].

Vacuum Expectation Value (VEV) of the Higgs field, denoted with ν, is non vanishing:

$$\langle 0|\phi(x)|0\rangle = \nu = \begin{pmatrix} 0 \\ \nu \end{pmatrix} \neq 0, \tag{1.20}$$

it should be clear from the context whether ν denotes the doublet or the only non zero component of the same doublet.

The fermion mass matrix is obtained by replacing $\phi(x)$ by ν in the Yukawa couplings:

$$M = \bar{\psi}_L \Gamma \nu \psi_R + \bar{\psi}_R \Gamma \nu \psi_L, \tag{1.21}$$

Γ is Hermitian and can always be diagonalised through a suitable change of basis if left fermions are doublets and right fermions are singlets. Each fermion mass term (m_{f}) can be written as:

$$m_{\mathrm{f}} = g_{\phi\bar{\mathrm{f}}\mathrm{f}}\nu, \tag{1.22}$$

where $g_{\phi ff}$ is the Yukawa coupling of the fermion f.

The the $(D_\mu\phi)^\dagger(D^\mu\phi)$ term in Eq. 1.17 leads to the mechanism responsible for the masses of vector boson, where:

$$D_\mu\phi = [\partial_\mu + \imath g \sum_{A=1}^{3} t^A \boldsymbol{W}_\mu^A + \imath g'(Y/2)\boldsymbol{B}_\mu]\phi. \tag{1.23}$$

The choice in Eq.1.20 preserves $U(1)$ symmetry related to the charge operator Q:

$$Q|\nu\rangle = (t^3 + \frac{1}{2}Y)|\nu\rangle = 0 \tag{1.24}$$

then the vacuum is electrically neutral and the particle related to the photon field remains massless.
The charged $\boldsymbol{W}$ mass term is:

$$m^2_{\boldsymbol{W}} \boldsymbol{W}^+_\mu \boldsymbol{W}^{-\mu} = g^2|(t^+\nu/\sqrt{2})|^2 \boldsymbol{W}^+_\mu \boldsymbol{W}^{-\mu}, \tag{1.25}$$

and the neutral $\boldsymbol{Z}$ mass term is:

$$\frac{1}{2}m^2_{\boldsymbol{Z}} \boldsymbol{Z}_\mu \boldsymbol{Z}^\mu = |(g\cos\theta_W t^3 - g'\sin\theta_W (Y/2))\nu|^2 \boldsymbol{Z}_\mu \boldsymbol{Z}^\mu, \tag{1.26}$$

where the factor of $1/2$ on the left-hand side is the correct normalisation for the definition of the mass of a neutral field. Expanding the action of t^3, t^+ and Y on ν [17] and using Eq. 1.15, the mass terms are:

$$m^2_{\mathbf{W}} = \frac{1}{2}g^2\nu^2, \quad m^2_{\mathbf{Z}} = \frac{1}{2}g^2\nu^2/\cos^2\theta_W, \tag{1.27}$$

ν is linked to the Fermi coupling constant (G_F) by means of $m_{\boldsymbol{W}}$ [1], and its value is:

$$\nu = 2m^2_{\mathbf{W}}/g^2 = 2^{-3/4}G_\mathrm{F}^{-1/2} = 174.1 \text{ GeV}. \tag{1.28}$$

The physical Higgs particle H can be introduced as a deviation from the vacuum:

$$\phi(x) = \begin{pmatrix} \phi^+(x) \\ \phi^0(x) \end{pmatrix} \rightarrow \begin{pmatrix} 0 \\ \nu + (H/\sqrt{2}) \end{pmatrix}. \tag{1.29}$$

The interactions with other bosons, obtained from the $(D_\mu\phi)^\dagger(D^\mu\phi)$ term in Eq. 1.17 are:

$$\begin{aligned} \mathcal{L}[H,\boldsymbol{W},\boldsymbol{Z}] = g^2\frac{v}{\sqrt{2}}\boldsymbol{W}^+_\mu \boldsymbol{W}^{-\mu}H + \frac{g^2}{4}\boldsymbol{W}^+_\mu \boldsymbol{W}^{-\mu}H^2 + \\ + g^2\frac{v}{2\sqrt{2}\cos^2\theta_W}\boldsymbol{Z}_\mu \boldsymbol{Z}^\mu H + \frac{g^2}{8\cos^2\theta_W}\boldsymbol{Z}_\mu \boldsymbol{Z}^\mu H^2 \ . \end{aligned} \tag{1.30}$$

According to Eq. 1.27, the explicit dependency on the masses is:

$$\begin{aligned} \mathcal{L}[H,\boldsymbol{W},\boldsymbol{Z}] = gm_{\boldsymbol{W}}\boldsymbol{W}^+_\mu \boldsymbol{W}^{-\mu}H + \frac{g^2}{4}\boldsymbol{W}^+_\mu \boldsymbol{W}^{-\mu}H^2 + \\ + \frac{gm_{\boldsymbol{Z}}}{2\cos^2\theta_W}\boldsymbol{Z}_\mu \boldsymbol{Z}^\mu H + \frac{g^2}{8\cos^2\theta_W}\boldsymbol{Z}_\mu \boldsymbol{Z}^\mu H^2. \end{aligned} \tag{1.31}$$

The generic coupling of H to a fermion of type f is given (after diagonalisation as in Eq. 1.22) by:

$$\mathcal{L}[H, \bar{\psi}, \psi] = \frac{g_{\mathrm{f}}}{\sqrt{2}} \bar{\psi}\psi H, \tag{1.32}$$

with

$$\frac{g_{\mathrm{f}}}{\sqrt{2}} = \frac{m_{\mathrm{f}}}{\sqrt{2}\nu} = 2^{1/4} G_{\mathrm{F}}^{1/2} m_{\mathrm{f}}. \tag{1.33}$$

The potential in Eq. 1.19 is minimum considering the replacement in Eq. 1.29, when:

$$v = \sqrt{\frac{\mu^2}{\lambda}}, \tag{1.34}$$

and its value is:

$$V = -\mu^2 (v + \frac{H}{\sqrt{2}})^2 + \frac{\mu^2}{2v^2}(v + \frac{H}{\sqrt{2}})^4 = -\frac{\mu^2 v^2}{2} + \mu^2 H^2 + \frac{\mu^2}{\sqrt{2}v} H^3 + \frac{\mu^2}{8v^2} H^4 \tag{1.35}$$

The mass term is then:

$$m_H^2 = 2\mu^2 = 2\lambda v^2 \tag{1.36}$$

1.3 Higgs boson physics

The decays of the Higgs boson are driven by Eq. 1.31 and Eq. 1.32. The (lowest-order) expressions for the dominant Higgs decay rates to fermion and vector boson pairs are [2]:

$$\begin{aligned} \Gamma(H \to f\bar{f}) &= N_C \frac{G_F m_H\, m_f^2}{4\pi\sqrt{2}} \sqrt{1 - \frac{4m_f^2}{m_H^2}} \;\; \text{with} \;\; N_C = 3\,(1) \text{ for } f = q\,(\ell), \\ \Gamma(H \to VV) &= \frac{G_F m_H^3}{16\pi\sqrt{2}} R_V(x_V), \quad x_V = \frac{M_V^2}{m_H^2}, \qquad (V = W, Z) \end{aligned} \tag{1.37}$$

with

$$R_Z = R(x_Z), \quad R_W = 2\,R(x_W), \quad R(x) = \sqrt{1-4x}\,(1 - 4x + 12x^2)\,. \tag{1.38}$$

A mass of about 125 GeV was measured by experiments (Sec. 1.3.1), this value provides an excellent opportunity to explore the Higgs couplings to many SM particles. In particular the dominant decay modes are $H \to b\bar{b}$ and $H \to WW^*$, followed by $H \to gg$, $H \to \tau^+\tau^-$, $H \to c\bar{c}$ and $H \to ZZ^*$. With much smaller rates follow the decays $H \to \gamma\gamma$, $H \to Z\gamma$ and $H \to \mu^+\mu^-$. Since the decays to gluons, di-photons and $Z\gamma$ are loop induced, they provide indirect information on the Higgs to WW, ZZ and $t\bar{t}$ couplings in different combinations [4]. The predicted branching ratios for the dominant Higgs decay processes are reported in Fig. 1.3 for a wide range of m_H.

The total predicted width of a 125 GeV SM Higgs boson is $\Gamma_H = 4.07 \times 10^{-3}$ GeV, with a relative uncertainty of $^{+4.0\%}_{-3.9\%}$ [20].

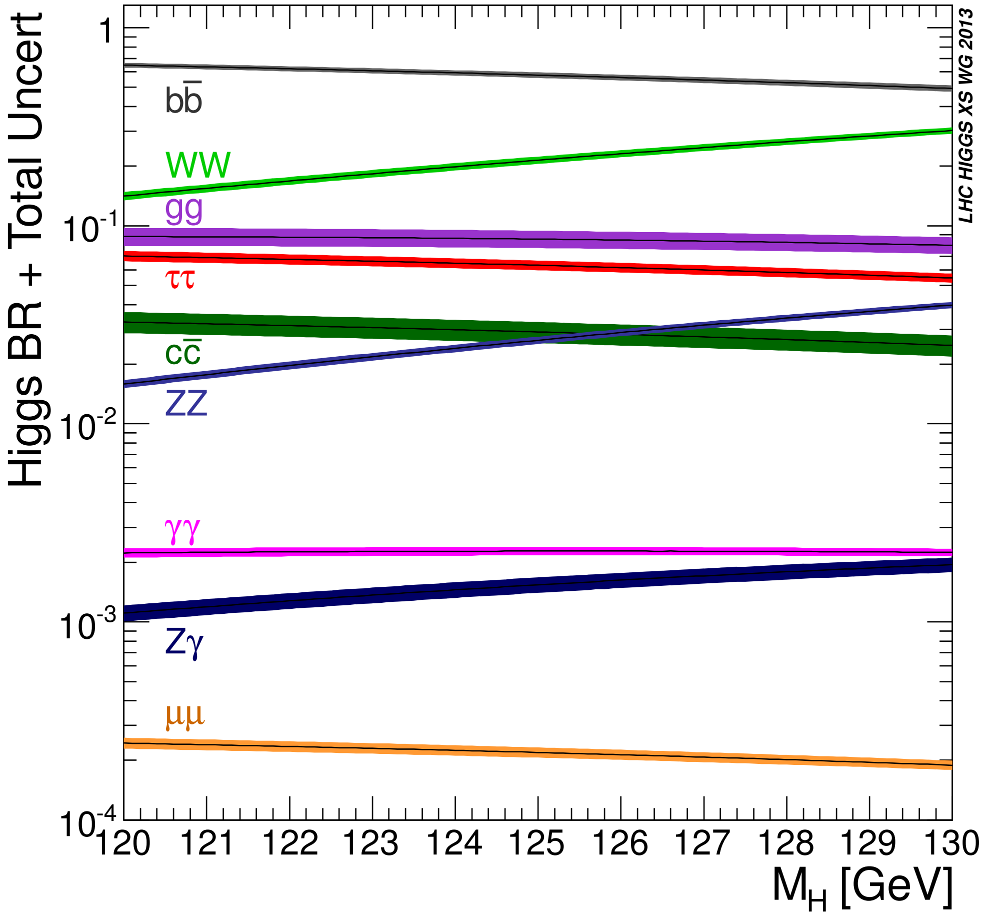

FIGURE 1.3: The branching ratios for the main decays of the SM Higgs boson near $m_H = 125$ GeV. The theoretical uncertainties are indicated as a band [20, 21].

At high-energy proton-proton colliders, the Higgs boson production mechanism [4, 20] with the largest cross section is the gluon-fusion process (ggF), $gg \to H + X$, mediated by the exchange of a virtual quark. Since contributions from light quarks propagating in the loop are suppressed proportionally to m_q the leading contribution arises from a top quark.

The SM Higgs production mode with the second-largest cross section at the LHC is the vector boson fusion (VBF). Higgs production via VBF, $qq \to qqH$, proceeds by the scattering of two (anti-)quarks, mediated by t- or u-channel exchange of a W or Z boson, with the Higgs boson radiated off the weak-boson propagator. The scattered quarks give rise to two hard jets in the forward and backward regions of the detector. Because of the colour-singlet nature of the weak-gauge boson exchange, gluon radiation from the central-rapidity regions is strongly suppressed. These characteristic features of VBF processes can be exploited to distinguish them from a priori overwhelming QCD

backgrounds, but also from gluon-fusion induced Higgs + 2 jet production, and from s-channel WH or ZH production with a hadronically decaying weak boson. Experimentally the VBF channel can be distinguished from other background processes by mean of a selection on kinematic properties of the events that lead to a particularly clean environment not only for Higgs searches but also for the determination of Higgs boson couplings.
The next most relevant Higgs boson production mechanisms are associated production with W and Z gauge bosons ($(W/Z)H$) originated from the processes $pp \to VH + X$, with $V = W^{\pm}, Z$.
Higgs production from $t\bar{t}$ fusion ($t\bar{t}H$), $pp \to t\bar{t}H$, can provide important information on the the top-Higgs Yukawa coupling. The cross sections for the dominant Higgs production processes for $m_H = 125$ GeV are presented in Fig. 1.5.

Fig. 1.4 represents diagrams for these dominant Higgs production processes.

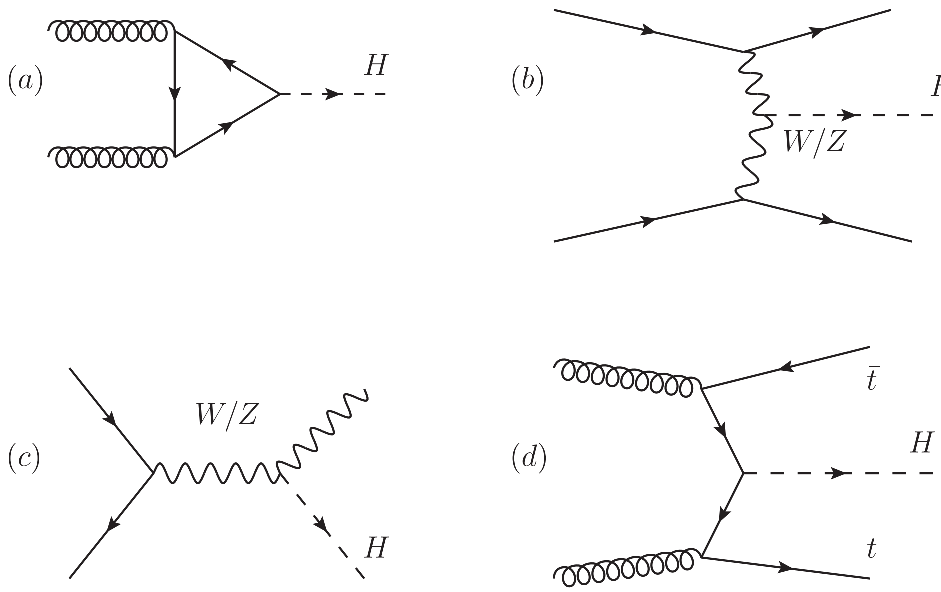

FIGURE 1.4: Higgs production channels: (a) gluon-gluon fusion, (b) vector boson fusion, (c) $(W/Z)H$ associated productions and (d) $t\bar{t}H$ associated production [22].

Fig. 1.6 shows the dependency of the production cross section on the mass of the Higgs boson for 7 TeV and 8 TeV energy in the centre-of-mass.

1.3.1 The long way to the discovery

The mass of the Higgs boson is a fundamental unpredictible parameter of the SM. An upper limit can be obtained from the partial-wave unitarity condition for a tree diagram

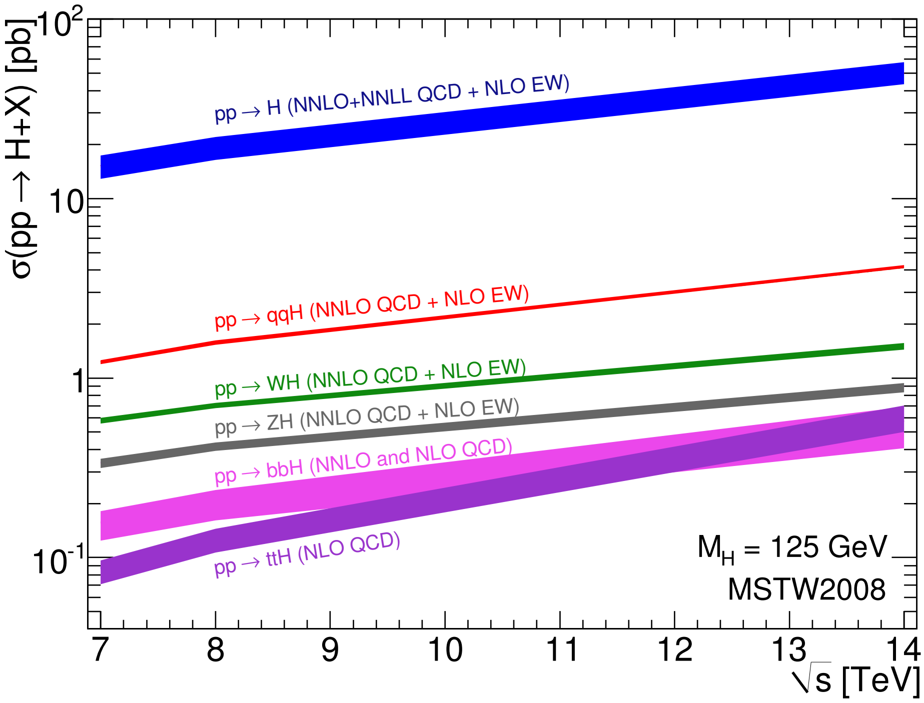

FIGURE 1.5: The SM Higgs boson production cross sections as a function of the centre-of-mass energy, $\sqrt{s}$, for pp collisions. The theoretical uncertainties are indicated as a band [20, 21].

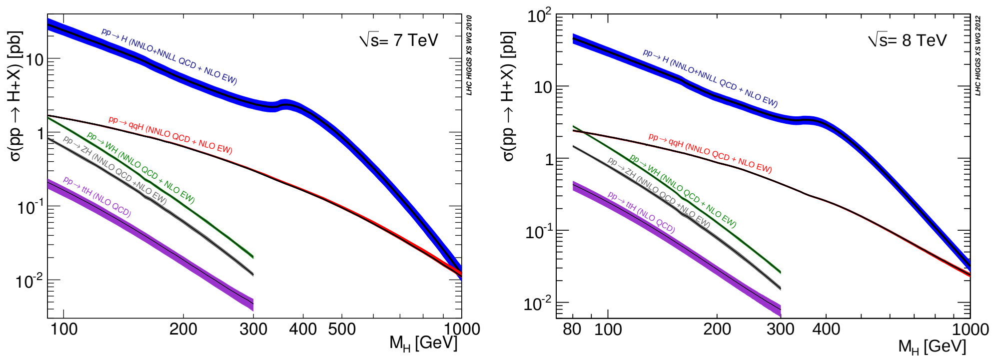

FIGURE 1.6: Standard Model Higgs boson production cross sections at a centre-of-mass energy (a) $\sqrt{s} = 7$ TeV and (b) 8 TeV [20, 21].

describing the two-body scattering of gauge bosons [23]:

$$m_H \lesssim \sqrt{8\pi\frac{\sqrt{2}}{3}G_{\mathrm{F}}} \sim 1 \text{ TeV}, \tag{1.39}$$

while a lower bound of 114.4 GeV resulted from the searches at LEP, summarised in Ref. [24]. In a such wide range of possible values the properties of the Higgs boson are strongly dependent on its mass value, in particular the total decay width (Γ_H) and the preferred decay channels as reported in Fig. 1.7. The decay of the Higgs boson is governed, at the leading order, by Eq. 1.37. For $m_H \lesssim 2m_{\mathbf{W}}$ the Higgs boson decays

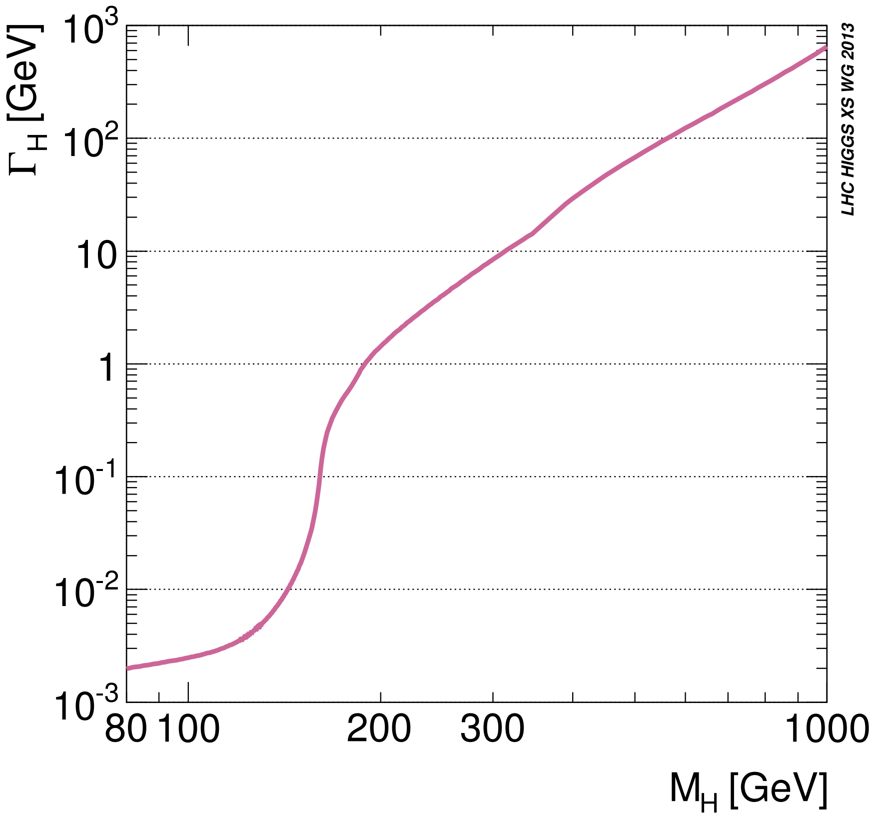

(a)

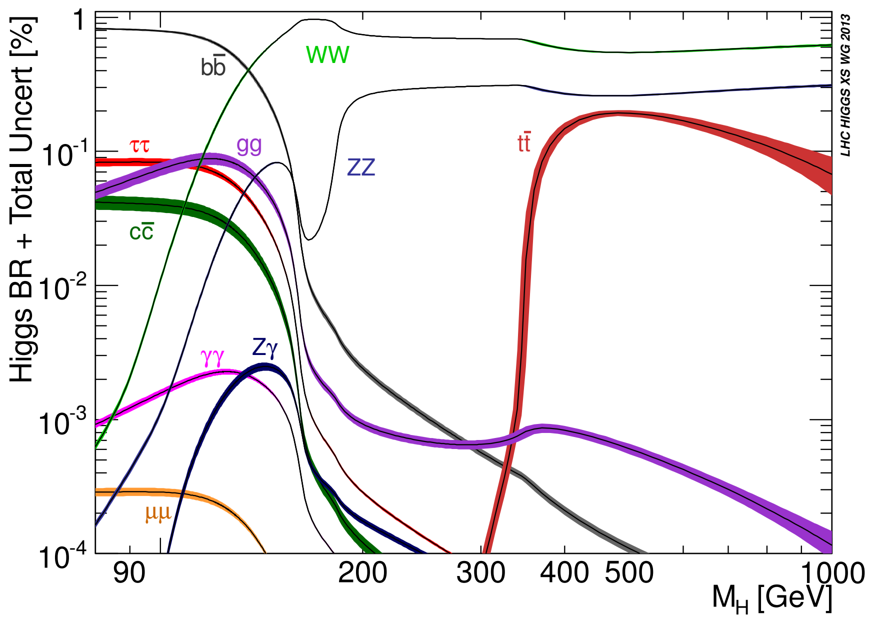

(b)

FIGURE 1.7: (a) Standard Model Higgs boson total width and (b) decay branching ratios [20, 21].

mainly to fermions with the higher mass accessible, with a proportionality $\Gamma_H \sim m_H$ and it is a narrow resonance. For $m_H \gtrsim 2m_{\mathbf{W}}$ the Higgs boson decays mainly to vector bosons, the total decay width rapidly increases as $\Gamma_H \sim m_H^3$ and the Higgs boson behaves as a broad resonance. For a Higgs boson with $m_H \gtrsim 2m_t$ the decay to t-quarks is accessible but the branching ratio is still disadvantaged with respect to the decay to vector bosons.
The Standard Model Higgs boson was searched for at the LHC in various decay channels, the choice of which was given by the signal rates and the signal-to-background ratios in the different mass regions [25]:

- $\boldsymbol{H \to ZZ^*}$ decays,
  the decay channel $H \to ZZ^* \to \ell\ell\,\ell\ell$ provides a rather clean signature in the intermediate mass region 115 GeV $< m_H < 2m_{\mathbf{Z}}$. In addition to the irreducible backgrounds from ZZ^* and $Z\gamma^*$ production, there are large reducible backgrounds from $t\bar{t}$ and $Zb\bar{b}$ production. Due to the large production cross section, the $t\bar{t}$ events dominate at production level, whereas the $Zb\bar{b}$ events contain a genuine Z boson in the final state and are therefore more difficult to reject. In addition, there is background from ZZ continuum production, where one of the Z bosons decays to a τ pair, with subsequent leptonic decays of the τ leptons, and the other Z decays to an electron or muon pair. Calorimeter and track isolation together with impact parameter measurements can be used to achieve the necessary background rejection. For Higgs boson masses in the range 180 GeV $< m_H <$ 700 GeV, the $H \to 4\ell$ decay mode is the most reliable one for the discovery of a Standard Model Higgs boson at the LHC. The expected background, which is dominated by the continuum production of Z boson pairs, is smaller than the signal. For larger values of m_H, the Higgs boson signal becomes very broad and the signal rate drops rapidly.

- $\boldsymbol{H \to \gamma\gamma}$ decays,
  the decay $H \to \gamma\gamma$ is a rare decay mode, which is only detectable in a limited Higgs boson mass region between 80 and 150 GeV, where both the production cross section and the decay branching ratio are relatively large. Excellent energy and angular resolution are required to observe the narrow mass peak above the irreducible prompt $\gamma\gamma$ continuum. In addition, there is a large reducible background resulting from direct photon production or from two-jet production via QCD processes.

- $\boldsymbol{H \to WW^*}$ decays,
  the dominant process for Higgs boson masses $m_H >$ 170 GeV, in the decay $H \to WW^* \to \ell\nu\,\ell\nu$ is possible to observe a peak in the distribution of the

transverse mass, M_T[2], computed from the leptons and the missing transverse momentum, even though the Higgs mass peak is not accessible because of the presence of undetected neutrinos. The non resonant WW, $t\bar{t}$ and single-top production processes constitute severe backgrounds and the signal significance depends critically on their absolute knowledge. In addition, it is possible to require that there is no jet activity in the central region of the detector (jet veto).

A specific requirement on the production mode can be considered, the most clear production mode is vector boson fusion. In vector boson fusion events, the Higgs boson is accompanied by two jets in the forward regions of the detector, originating from the initial quarks that emit the vector bosons. On the other hand, central jet activity is suppressed due to the lack of colour exchange between the initial state quarks. This is in contrast with most background processes, where colour flow appears in the t-channel. Jet tagging in the forward region of the detector together with a veto of jet activity in the central region are therefore powerful tools to enhance the signal-to-background ratio.
The first bound to the mass of the Higgs boson was obtained at LEP [24], the main production mode was the ZH associated production because of the e^+e^- colliding beams. The maximum centre-of-mass energy was $\sim$ 206 GeV and the low mass region for the Higgs boson was accessible, where the $H \to b\bar{b}$ decay is dominant. Multi-jets backgrounds were very low because of the leptonic nature of the colliding beams. A lower bound of 114.4 GeV was obtained from the combinaton of the four experiments hosted at LEP.
The second important step in the search for the Higgs boson was achieved at Tevatron [26]. In the $p\bar{p}$ Tevatron collider at a centre-of-mass energy of 1.96 TeV, all the production modes were accessible but the dominant one was the associated production with a vector boson. The Higgs boson decay modes studied were $H \to b\bar{b}$, $H \to W^+W^-$, $H \to ZZ$, $H \to \tau^+\tau^-$ and $H \to \gamma\gamma$. The regions $100 < m_H < 120$ GeV and $139 < m_H < 184$ GeV were excluded and an excess corresponding to a local significance of $\sim$ 3.0 standard deviations was found for $m_H \sim 120$ GeV,

Finally , the Higgs boson was found at the LHC by the ATLAS and CMS experiments [27, 28]. The main production channel was ggF but VBF was also sizeable. The main contribution to the discovery was due to the $H \to \gamma\gamma$ and $H \to ZZ^*$ decays. As reported in Fig. 1.8, the probability for an excess as large as or larger than that observed in the first 10 fb^{-1}by each experiment to arise from a statistical fluctuation of the background was very low. The excess was then interpreted as the observation of a new particle with a mass near 125 GeV. The decays to two photons or to ZZ^*

[2] $M_T = \sqrt{2p_{\mathrm{T}}^{\ell\ell}E_{\mathrm{T}}^{\mathrm{miss}}(1-\cos\Delta\phi_{\ell\ell})}$.

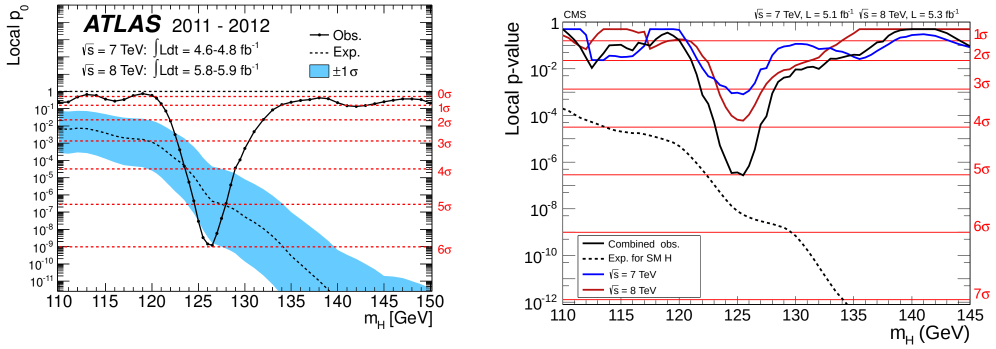

(a) (b)

FIGURE 1.8: (a) The ATLAS observed (solid) local p_0 as a function of m_H in the low mass range. The dashed curve shows the expected local p_0 under the hypothesis of a SM Higgs boson signal at that mass with its $\pm 1\sigma$ band. The horizontal dashed lines indicate the p-values corresponding to significances of 1 to 6 σ [27]. (b) The CMS observed local p-value for 7 TeV and 8 TeV data, and their combination as a function of the SM Higgs boson mass. The dashed line shows the expected local p-values for a SM Higgs boson with a mass m_H [28].

indicated that the new particle was a boson; the two-photon decay implied that its spin was different from one.

The combination of the ATLAS and CMS mass measurement of the Higgs boson was performed in Ref. [29], the result is

$$m_H = 125.09 \pm 0.24 \quad \text{GeV}.$$

1.4 Limitations of the Standard Model

The discovery of the Higgs boson is the latest great success of the Standard Model of particle physics. The Higgs' mechanism is a cornerstone of the SM, with its elegant way of breaking symmetry it makes possible for the elementary particles to acquire masses. Over forty years, the SM has passed a series of increasingly stringent tests. As the parameters of the model became better defned and its predictions tested more incisively, points of disagreement between theory and experiment have faded away. Now the last elementary particle predicted by this model has been observed. Is it the last discovery of the SM?

There are many arguments outside the domain of the Higgs boson that support the idea that Standard Model is incomplete as a description of nature [3, 30]. It is possible to summarise the open issues in eleven items [31]:

1. How do we understand the Higgs boson? What principle determines its couplings to quarks and leptons? Why does it condense and acquire a vacuum value throughout the Universe? Is there one Higgs particle or many? Is the Higgs particle elementary or composite?

2. What principle determines the masses and mixings of quarks and leptons? Why is the mixing pattern apparently different for quarks and leptons? Why is there CP violation in quark mixing? Do leptons violate CP?

3. Why are neutrinos so light compared to other matter particles? Are neutrinos their own antiparticles? Are their small masses connected to the presence of a very high mass scale? Are there new interactions that are invisible except through their role in neutrino physics?

4. What mechanism produced the excess of matter over anti-matter that we see in the Universe? Why are the interactions of particles and antiparticles not exactly mirror opposites?

5. Dark matter is the dominant component of mass in the Universe. What is the dark matter made of? Is it composed of one type of new particle or several? What principle determined the current density of dark matter in the Universe? Are the dark matter particles connected to the particles of the Standard Model, or are they part of an entirely new dark sector of particles?

6. What is dark energy? Is it a static energy per unit volume of the vacuum, or is it dynamical and evolving with the Universe? What principle determines its value?

7. What did the Universe look like in its earliest moments, and how did it evolve to contain the structures we observe today? The inflationary Universe model requires new fields active in the early Universe. Where did these come from, and how can we probe them today?

8. Are there additional forces that we have not yet observed? Are there additional quantum numbers associated with new fundamental symmetries? Are the four known forces unified at very short distances? What principles are involved in this unification?

9. Are there new particles at the TeV energy scale? Such particles are motivated by the problem of the Higgs boson, and by ideas about space-time symmetry such as supersymmetry and extra dimensions. If they exist, how do they acquire mass, and what is their mass spectrum? Do they provide new sources of quark and lepton mixing and CP violation?

10. Are there new particles that are light and extremely weakly interacting? Such particles are motivated by many issues, including the strong CP problem, dark matter, dark energy, inflation, and attempts to unify the microscopic forces with gravity. What experiments can be used to find evidence for these particles?

11. Are there extremely massive particles to which we can only couple indirectly at currently accessible energies? Examples of such particles are seesaw heavy neutrinos or grand unified scale particles mediating proton decay. How can we demonstrate that these particles exist?

Answers to these questions may be found through the observation of new phenomena hopefully in the near future.

Chapter 2

ATLAS and LHC

ATLAS is a particle physics detector at the Large Hadron Collider at CERN. LHC is the world's largest and most powerful particle accelerator, it is located in the tunnel (27 km) that hosted LEP, in the border between France and Switzerland close to Geneve. LHC first started up on 10 September 2008, and remains the latest addition to the accelerator complex at CERN. Inside the accelerator, two high-energy particle beams travel at close to the speed of light before they are made to collide at four locations around the accelerator ring, corresponding to the positions of four particle detectors: ATLAS [32], CMS [33], ALICE [34] and LHCb [35]. ATLAS is located at the Interaction Point One.

An overview of the LHC Complex and a description of the ATLAS detector will be given in this Chapter.

2.1 The Large Hadron Collider

The aim of the LHC [36] is to reveal and study very rare physics processes such as processes involving the Higgs boson or BSM processes.
The number of events per second generated in the LHC collisions is given by (N_{event}):

$$N_{\text{event}} = L\sigma_{\text{event}}, \tag{2.1}$$

where σ_{event} is the total inelastic cross section and L the machine luminosity. Assuming Gaussian beam distributions, the luminosity is:

$$L = \frac{N_b^2 n_b f_{\text{rev}} \gamma_r}{4\pi\varepsilon_n\beta^*} F, \tag{2.2}$$

where N_b is the number of particles per bunch, n_b the number of bunches per beam, f_{rev} the revolution frequency, γ_r the relativistic gamma factor, ε_n the normalised transverse beam emittance [37], β^* the beta function [37] at the collision point and F the generic geometric luminosity reduction factor [36] due to the crossing angle at the interaction point, which is about 0.9 at the LHC [38].
In order to reach 7 TeV per beam in the LHC ring, a complex accelerating system is adopted (Fig. 2.1), it is constituted by: Linac2, Proton Synchrotron Booster, Proton Synchrotron, Super Proton Synchrotron. The main LHC parameters are summarised

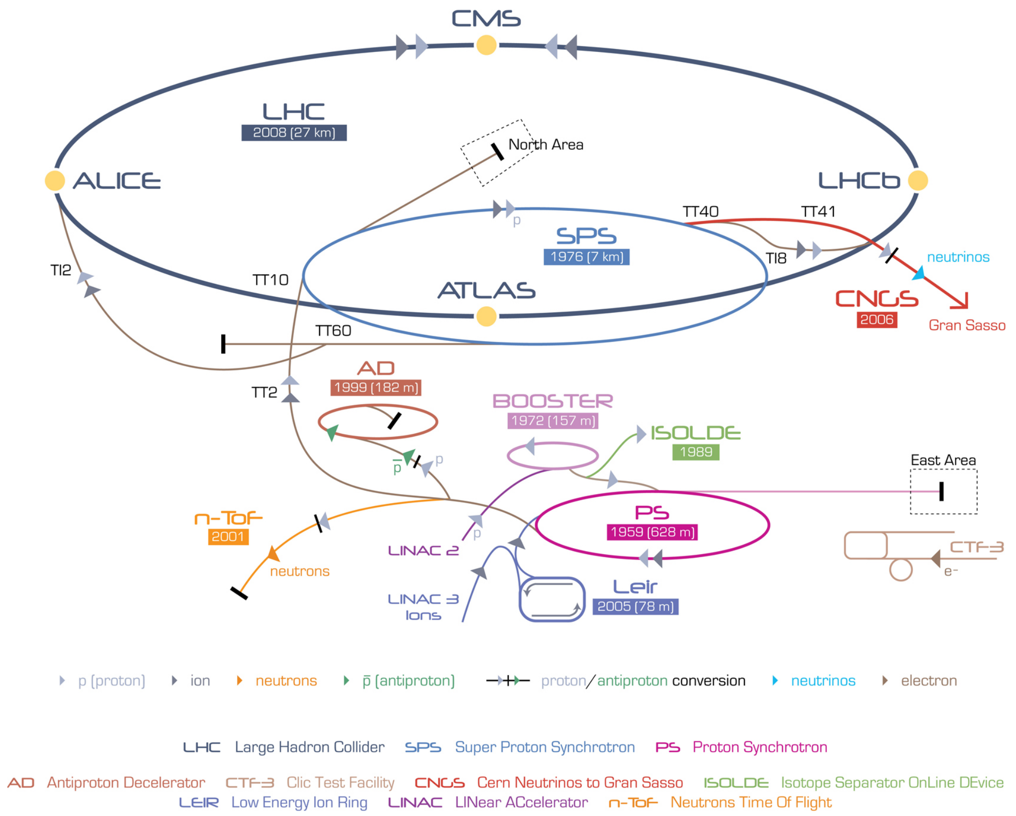

FIGURE 2.1: The LHC accelerator complex. [39].

in Tab. 2.1. The proton-proton integrated luminosity ($L_{\text{int}} = \int L dt$) collected in Run-1 of LHC by the ATLAS detector is reported in Fig. 2.2 as well as the luminosity peak of each operation day. Thanks to the good operation of the detector, almost the full intensity delivered by LHC was recorded by ATLAS experiment and it is available for physics analyses.

Parameter	2011	2012	Design
Beam Energy [TeV]	3.5	4	7
Max Number of Bunches colliding	1854	1380	2808
Bunch Intensity [10^{11}]	1.5	1.48	1.15
Bunch Spacing [ns]	50	50	25
Peak Inst. Lumi. [10^{33} cm^{-2} s^{-1}]	3.65	7.73	10
Avg. Inelastic Interactions per crossing $\langle\mu\rangle$	9.1	20.7	19
Peak Inelastic Interactions per crossing	34	72	
Trans. Norm. Emittance [μm]	1.9-2.3	2.6	3.75
Longitudinal Emittance [eV s]			2.5
β^* [m]	1	0.60	0.55
IP Beam Spot [μm]	$\approx$25	19	16.7
Beam Current [A]	0.38	0.41	0.582
RMS Bunch Length [cm]		$\geq$9	7.55
Crossing Angle [μrad]	240	290	285

Table 2.1: LHC main parameters [40].

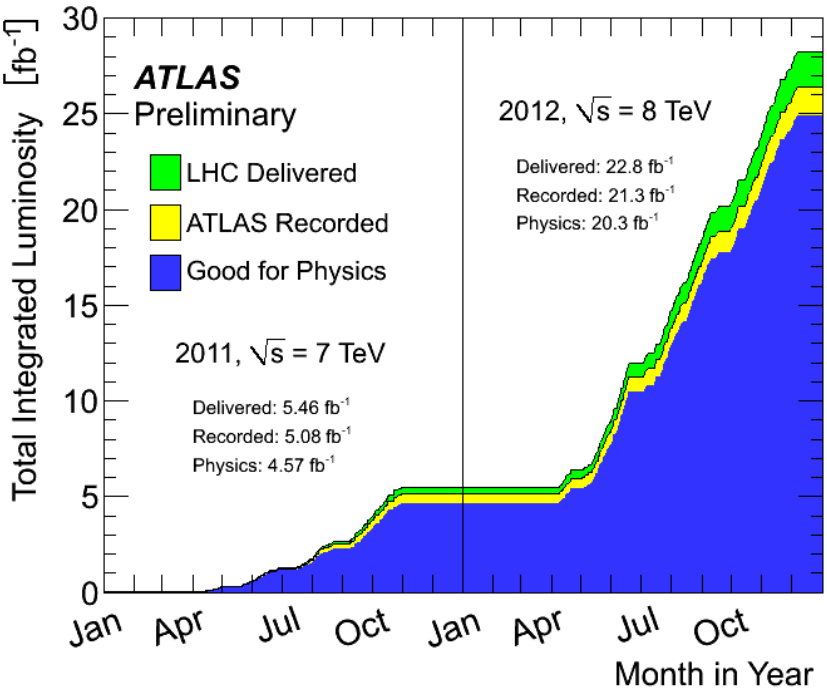

(a)

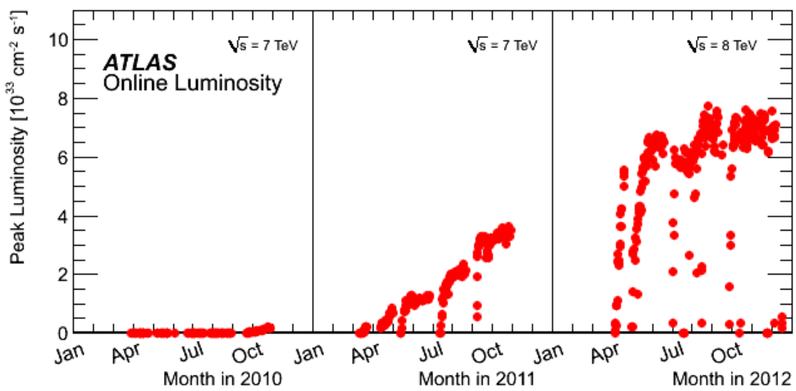

(b)

FIGURE 2.2: (a) ATLAS integrated luminosity ($L_{\text{int}} = \int L\mathrm{d}t$) for proton-proton collisions; (b) ATLAS peak luminosity per day [41, 42].

As reported in Tab. 2.1 multiple beam-beam interaction occurs in a collision, Fig. 2.3 shows the distributions of the mean number of interactions per bunch crossing for the Run-1 of LHC.

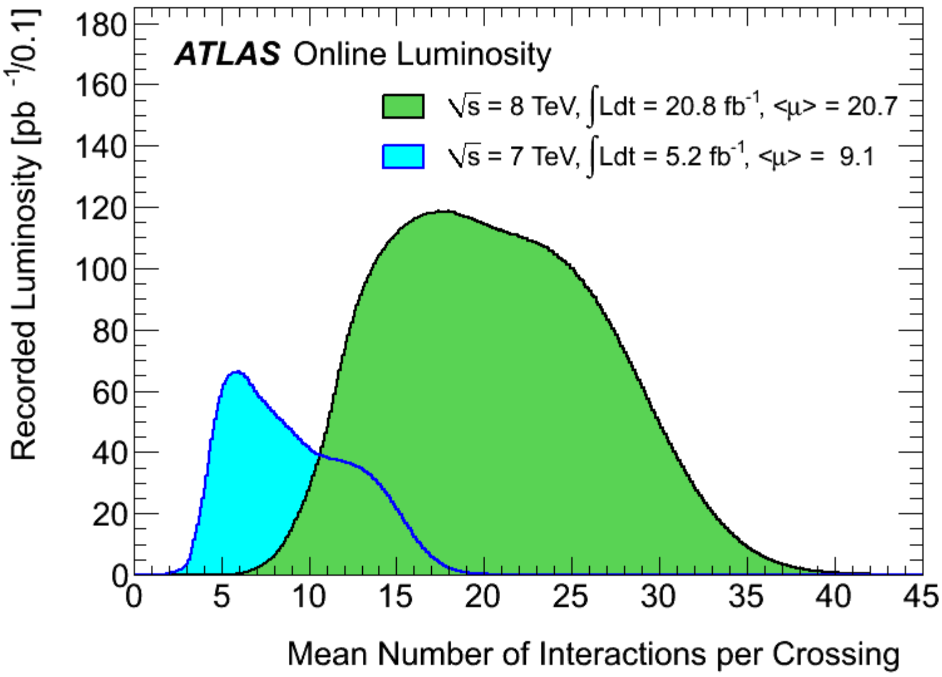

FIGURE 2.3: Mean number of interactions per bunch crossing for the Run-1 of LHC (ATLAS) [42].

2.2 ATLAS

ATLAS [32, 43] is a multi-purpose particle physics detector with a forward-backward symmetric cylindrical geometry and close to 4π coverage in solid angle. From the innermost part to the outermost ATLAS presents the typical structure of a HEP detector allowing to identify and measure the properties of the particles produced in a collision as shown in Fig 2.4. The ATLAS detector (Fig. 2.5) consists of an inner tracking detector (ID) surrounded by a thin 2 T superconducting solenoid, electromagnetic (EMCal) and hadronic calorimeters (HCal), and a muon spectrometer (MS) incorporating three large superconducting toroid magnets, each with eight coils. The main performance goals of the ATLAS detector are listed in Tab. 2.2. A three-level trigger system is used.

2.2.1 Inner Detector

The Inner Detector [45, 46] covers the pseudorapidity range $|\eta| < 2.5$ and consists of multiple layers of silicon pixel and micro-strip detectors (SCT), and a straw-tube transition radiation tracker (TRT).
The Inner Detector consists of three sub-detectors. The envelope of each sub-detector is listed in Tab. 2.3 and shown in Fig. 2.6. At inner radii, high-resolution pattern

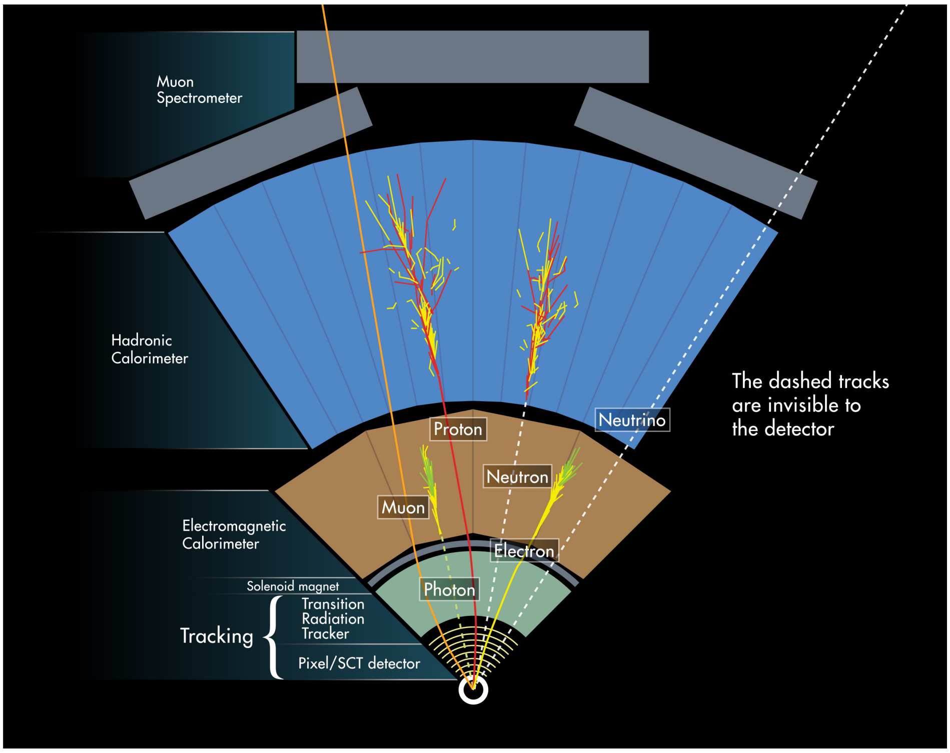

FIGURE 2.4: The typical structure of a HEP particle detector. From the interaction point to the outermost part of the detector the sub-detectors are: Tracking System, Calorimeters, Muon Spectrometer. [44].

Detector component	**Required resolution**	**η coverage**	
		Measurement	Trigger
Tracking	$\sigma_{p_T}/p_T = 0.05\% p_T \oplus 1\%$	± 2.5	
EMCal	$\sigma_E/E = 10\%/\sqrt{E} \oplus 0.7\%$	± 3.2	± 2.5
HCal (jets)			
barrel and end cap	$\sigma_E/E = 50\%/\sqrt{E} \oplus 3\%$	± 3.2	± 3.2
forward	$\sigma_E/E = 100\%/\sqrt{E} \oplus 10\%$	$3.1 < \lvert\eta\rvert < 4.9$	$3.1 < \lvert\eta\rvert < 4.9$
Muon Spectrometer	$\sigma_{p_\mathrm{T}} = 10\%$ @ $p_\mathrm{T} = 1$ TeV	± 2.7	± 2.4

TABLE 2.2: General performance goals of the ATLAS detector. Note that, for high-p_T muons, the muon-spectrometer performance is independent of the inner-detector system. E and p_T are expressed in GeV [32].

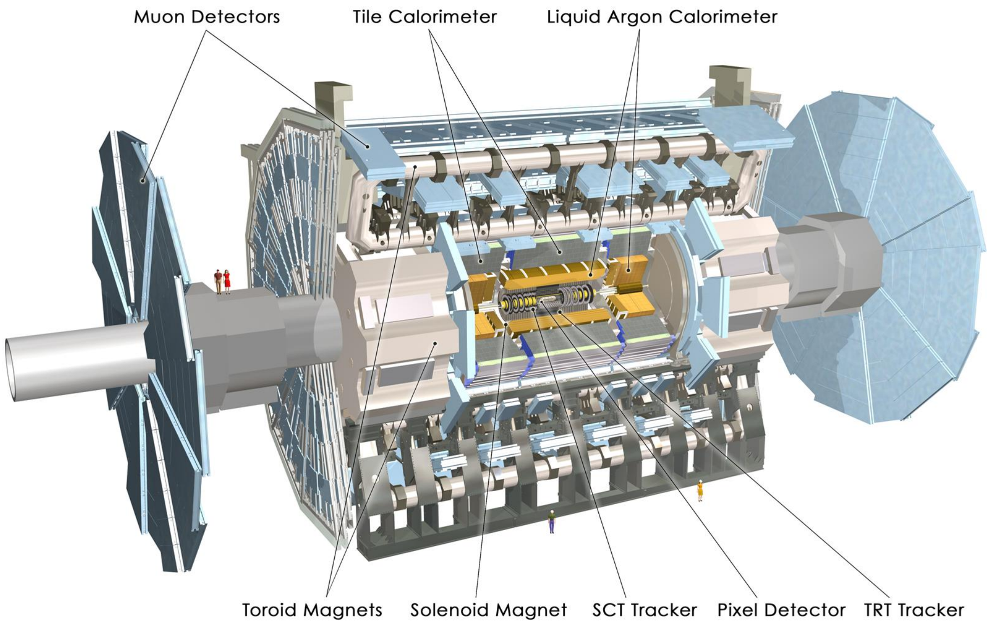

FIGURE 2.5: Cut-away view of the ATLAS detector. The dimensions of the detector are 25 m in height and 44 m in length. The overall weight of the detector is approximately 7000 tonnes [44].

recognition capabilities are available using discrete space-points from silicon pixel layers and stereo pairs of silicon micro-strip layers. At larger radii, the transition radiation tracker comprises many layers of gaseous straw tube elements interleaved with transition radiation material. With an average of 36 hits per track, it provides continuous tracking to enhance the pattern recognition and improve the momentum resolution over $|\eta| < 2.0$ and electron identification complementary to that of the calorimeter over a wide range of energies.

2.2.2 Calorimetry

Calorimeters [47] must provide good measurement and good containment for electromagnetic and hadronic showers, and must also limit punch-through into the muon system. Hence, calorimeter depth is an important design consideration. The total thickness of the EM calorimeter is greater than 22 radiation lengths ($\boldsymbol{X}_0$) in the barrel and greater than 24 $\boldsymbol{X}_0$ in the end caps. The approximate 9.7 interaction lengths (λ) of hadronic active calorimeter in the barrel (10 λ in the end caps) are adequate to provide good resolution for high-energy jets.
The calorimeter system covers the pseudorapidity range $|\eta| < 4.9$.

- The EM calorimeter is divided into a barrel part ($|\eta| < 1.475$) and two end-cap components ($1.375 < |\eta| < 3.2$), each housed in their own cryostat. The EM

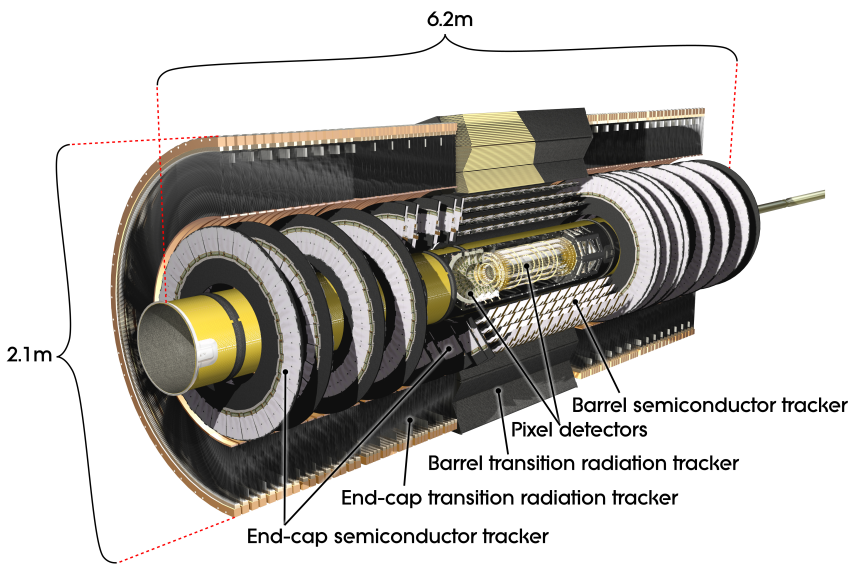

(a)

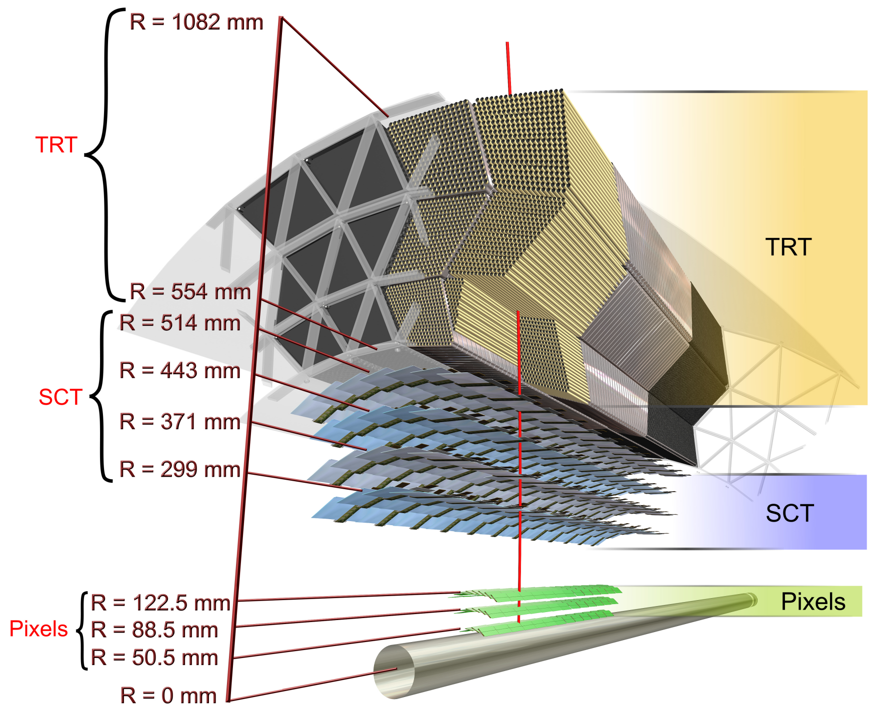

(b)

FIGURE 2.6: (a) Cut-away view of the ATLAS Inner Detector and (b) zoom on the barrel components [44].

Item		Radial extension (mm)	Length (mm)
overall ID envelope		$0 < R < 1150$	$0 < \|z\| < 3512$
beam-pipe		$29 < R < 36$	
Pixel	overall	$45.5 < R < 242$	$0 < \|z\| < 3092$
3 cylindrical layers	barrel	$50.5 < R < 122.5$	$0 < \|z\| < 400.5$
2×3 disks	end cap	$88.8 < R < 149.6$	$495 < \|z\| < 650$
SCT	overall	$255 < R < 549$ (barrel)	$0 < \|z\| < 805$
		$251 < R < 610$ (end cap)	$0 < \|z\| < 2797$
4 cylindrical layers	barrel	$299 < R < 514$	$0 < \|z\| < 749$
2×9 disks	end cap	$275 < R < 560$	$839 < \|z\| < 2735$
TRT	overall	$554 < R < 1082$ (barrel)	$0 < \|z\| < 780$
		$617 < R < 1082$ (end cap)	$0 < \|z\| < 2744$
73 straw planes	barrel	$563 < R < 1066$	$0 < \|z\| < 712$
160 straw planes	end cap	$644 < R < 1004$	$848 < \|z\| < 2710$

Table 2.3: Main parameters of the inner-detector system [32].

calorimeter is a lead-LAr detector with accordion-shaped kapton electrodes and lead absorber plates over its full coverage. In the region of $|\eta| < 1.8$, a presampler detector is used to correct for the energy lost by electrons and photons upstream of the calorimeter. The presampler consists of an active LAr layer of thickness 1.1 cm (0.5 cm) in the barrel (end-cap) region.

- The Hadronic Calorimeter consists of Tile Calorimeter, LAr Hadronic End-cap Calorimeter, LAr Forward Calorimeter.

  The Tile Calorimeter is placed directly outside the EM calorimeter envelope. Its barrel covers the region $|\eta| < 1.0$, and its two extended barrels the range $0.8 < |\eta| < 1.7$. It is a sampling calorimeter using steel as absorber and scintillating tiles as active material. Radially, the Tile Calorimeter extends from an inner radius of 2.28 m to an outer radius of 4.25 m.

  The Hadronic End-cap Calorimeter consists of two independent wheels per end-cap, located directly behind the end-cap electromagnetic calorimeter and sharing the same LAr cryostats. Each wheel is divided into two segments in depth, for a total of four layers per end-cap. The wheels closest to the interaction point are built from 25 mm parallel copper plates, while those further away use 50 mm copper plates (for all wheels the first plate is half-thickness).

  The Forward Calorimeter (FCal) is integrated into the end-cap cryostats, as this provides clear benefits in terms of uniformity of the calorimetric coverage as well as reduced radiation background levels in the muon spectrometer. The FCal is approximately 10 interaction lengths deep, and consists of three modules in each end-cap: the first, made of copper, is optimised for electromagnetic measurements, while the other two, made of tungsten, measure predominantly the energy of hadronic interactions.

The pseudorapidity coverage and segmentation in depth of the calorimeters are summarised in Tab. 2.4 and Fig. 2.7 shows an overview of the calorimeter system.

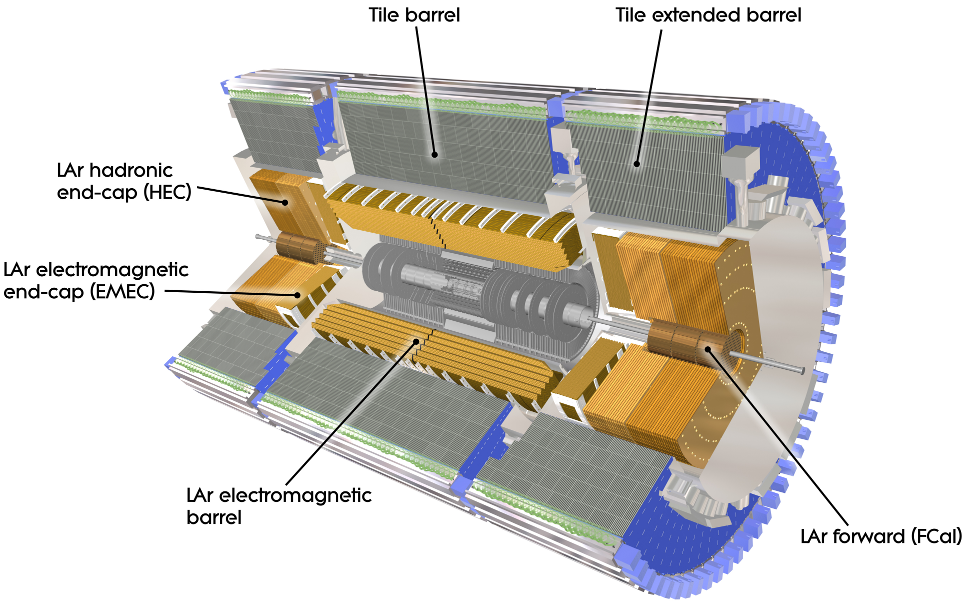

FIGURE 2.7: Cut-away view of the ATLAS calorimeter system [44].

2.2.3 Muon system

The conceptual layout of the muon spectrometer [48] is shown in Fig. 2.8. It is based on the magnetic deflection of muon tracks in the large superconducting air-core toroid magnets, instrumented with separate trigger and high-precision tracking chambers. Over the range $|\eta| < 1.4$, magnetic bending is provided by the large air core toroid. For $1.6 < |\eta| < 2.7$, muon tracks are bent by two smaller air core toroid end-cap magnets inserted into both ends of the barrel toroid. Over $1.4 < |\eta| < 1.6$, usually referred to as the transition region, magnetic deflection is provided by a combination of barrel and end-cap fields. This magnet configuration, in particular the air core toroids, provides a field which is mostly orthogonal to the muon trajectories, while minimising the degradation of resolution due to multiple scattering.
In the barrel region, tracks are measured in chambers arranged in three cylindrical layers around the beam axis; in the transition and end-cap regions, the chambers are installed

	barrel		end cap	
EMCal				
Number of layers and η coverage				
Presampler	1	$\lvert\eta\rvert < 1.52$	1	$1.5 < \lvert\eta\rvert < 1.8$
Calorimeter	3	$\lvert\eta\rvert < 1.35$	2	$1.375 < \lvert\eta\rvert < 1.5$
	2	$1.35 < \lvert\eta\rvert < 1.475$	2	$1.5 < \lvert\eta\rvert < 2.5$
			2	$2.5 < \lvert\eta\rvert < 3.2$
Number of readout channels (# Readout)				
Presampler	7808		1536 (both sides)	
Calorimeter	101760		62208 (both sides)	
LAr Hadronic end-cap				
η coverage			$1.5 < \lvert\eta\rvert < 3.2$	
Layers			4	
# Readout			5632 (both sides)	
LAr forward calorimeter				
η coverage			$3.1 < \lvert\eta\rvert < 4.9$	
Layers			3	
# Readout			3524 (both sides)	
Tile Calorimeter				
	barrel		Extended	
η coverage	$\lvert\eta\rvert < 1.0$		$0.8 < \lvert\eta\rvert < 1.7$	
Layers	3		3	
# Readout	5760		4092 (both sides)	

TABLE 2.4: Main parameters of the calorimeter system [32].

in planes perpendicular to the beam, also in three layers. Over most of the η-range, a precision measurement of the track coordinates in the principal bending direction of the magnetic field is provided by Monitored Drift Tubes (MDT) . At large pseudorapidities, Cathode Strip Chambers (CSCs, which are multi-wire proportional chambers [4, 49] with cathodes segmented into strips) with higher granularity are used in the innermost plane over $2 < |\eta| < 2.7$, to withstand the demanding rate and background conditions. The trigger system covers the pseudorapidity range $|\eta| < 2.4$. The trigger chambers for the muon spectrometer serve a threefold purpose: provide bunch-crossing identification, provide well-defined p_{T} thresholds, and measure the muon coordinate in the direction orthogonal to that determined by the precision-tracking chambers. Resistive Plate Chambers (RPC) [4, 50] are used in the barrel and Thin Gap Chambers (TGC) [51] in the end-cap regions.

The main parameters of the muon system are summarised in Tab. 2.5.

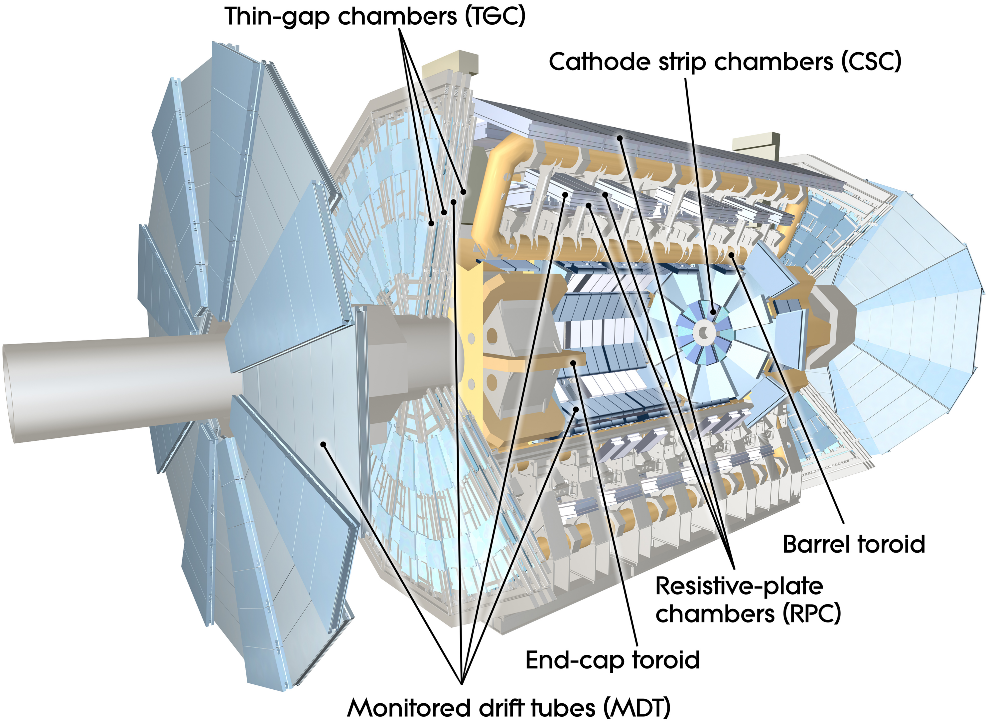

FIGURE 2.8: Cut-away view of the ATLAS muon system [44].

Monitored drift tubes	**MDT**
- Coverage	$\|\eta\| < 2.7$ (innermost layer: $\|\eta\| < 2.0$)
- Number of chambers	1088 (1150)
- Number of channels	339 000 (354 000)
- Function	Precision tracking
Cathode strip chambers	**CSC**
- Coverage	$2.0 < \|\eta\| < 2.7$
- Number of chambers	32
- Number of channels	31 000
- Function	Precision tracking
Resistive plate chambers	**RPC**
- Coverage	$\|\eta\| < 1.05$
- Number of chambers	544 (606)
- Number of channels	359 000 (373 000)
- Function	Triggering, second coordinate
Thin gap chambers	**TGC**
- Coverage	$1.05 < \|\eta\| < 2.7$ (2.4 for triggering)
- Number of chambers	3588
- Number of channels	318 000
- Function	Triggering, second coordinate

TABLE 2.5: Main parameters of the muon system [32].

2.2.4 Trigger system

The proton-proton interaction rate at the design luminosity of 10^{34} cm^{-2}s^{-1} is approximately 1 GHz, while the event data recording, based on technology and resource limitations, is limited to about 200 Hz. This requires an overall rejection factor of 5×10^6 against minimum-bias processes while maintaining maximum efficiency for the investigation of rare processes involving for instance the Higgs boson, as reported in Fig. 2.9.

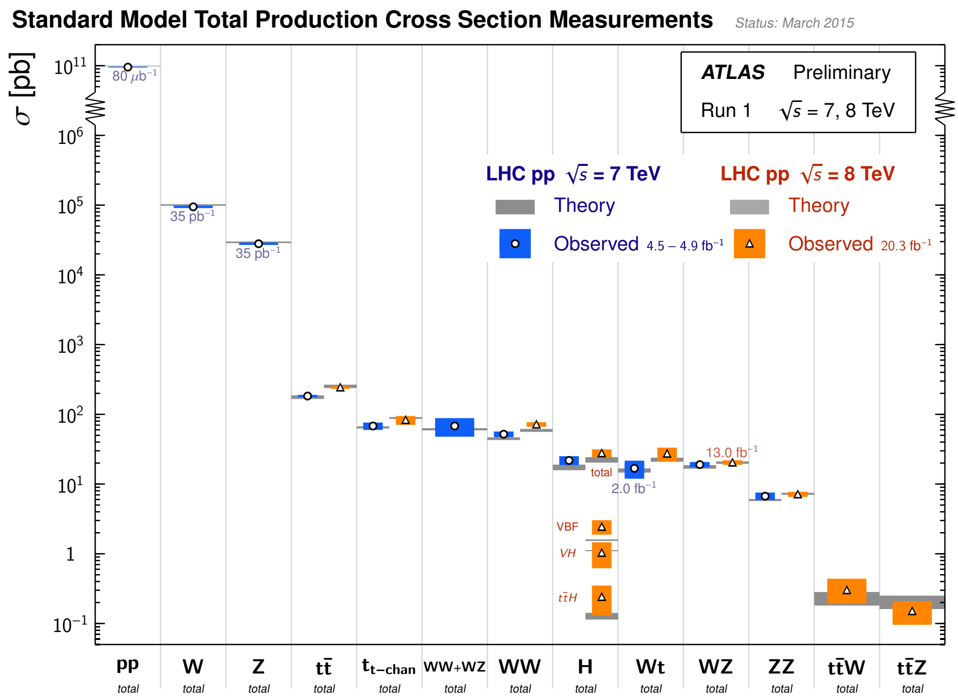

FIGURE 2.9: Summary of several Standard Model processes production cross section measurements, corrected for leptonic branching fractions, compared to the corresponding theoretical expectations. The luminosity used for each measurement is indicated close to the data point. Uncertainties on the theoretical predictions are quoted from the original ATLAS publications [52].

The Level-1 (L1) trigger system uses a subset of the total detector information to make a decision on whether or not to continue processing an event, reducing the data rate to approximately 75 kHz (limited by the bandwidth of the readout system, which is upgradeable to 100 kHz). The subsequent two levels, collectively known as the high-level trigger, are the Level-2 (L2) trigger and the event filter. They provide the reduction to a final data-taking rate of approximately 200 Hz.
The L1 trigger searches for high transverse-momentum muons, electrons, photons, jets, and $\tau-$leptons decaying to hadrons, as well as large missing momentum and total transverse momentum. Its selection is based on information from a subset of detectors. High

transverse-momentum muons are identified using trigger chambers in the barrel and end-cap regions of the spectrometer. Calorimeter selections are based on reduced-granularity information from all the calorimeters. Results from the L1 muon and calorimeter triggers are processed by the central trigger processor, which implements a trigger 'menu' made up of combinations of trigger selections. Pre-scaling of trigger menu items is also available, allowing optimal use of the bandwidth as luminosity and background conditions change. Events passing the L1 trigger selection are transferred to the next stages of the detector-specific electronics and subsequently to the data acquisition via point-to-point links. In each event, the L1 trigger also defines one or more Regions-of-Interest (RoI), i.e. the geographical coordinates in η and ϕ, of those regions within the detector where its selection process has identified interesting features. The RoI data include information on the type of feature identified and the criteria passed, e.g. a threshold. This information is subsequently used by the high-level trigger.

The L2 selection is seeded by the RoI information provided by the L1 trigger over a dedicated data path. L2 selections use, at full granularity and precision, all the available detector data within the RoI (approximately 2% of the total event data). The L2 menus are designed to reduce the trigger rate to approximately 3.5 kHz, with an event processing time of about 40 ms, averaged over all events.

The final stage of the event selection is carried out by the event filter. Its selections are implemented using offline analysis procedures within an average event processing time of the order of four seconds.

A schematic view of the ATLAS trigger system is shown in Fig. 2.10.

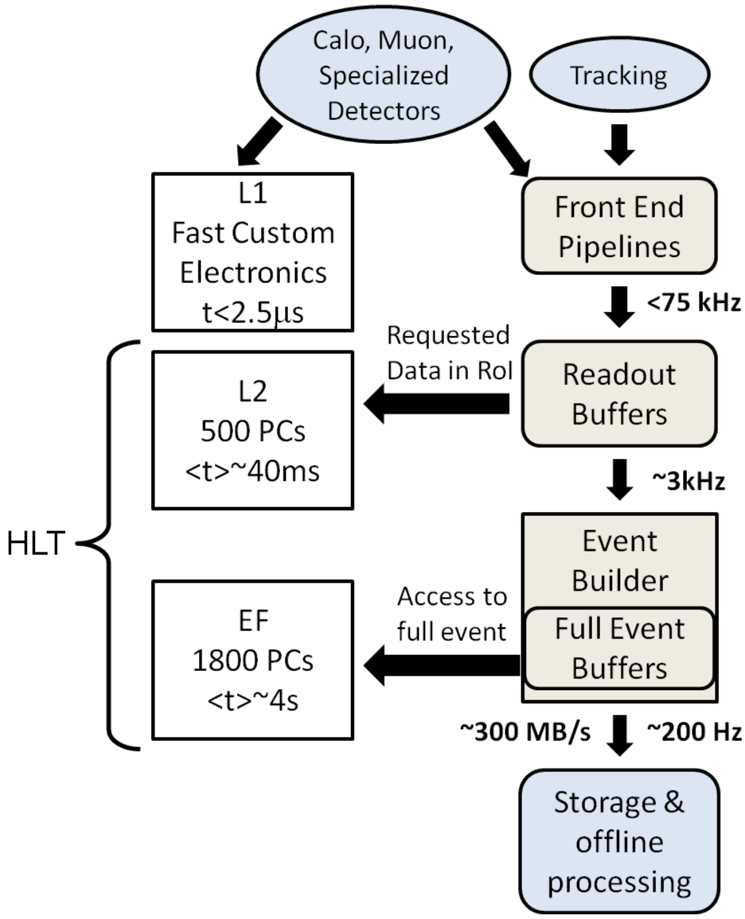

FIGURE 2.10: Schematic of the ATLAS trigger system [53].

Chapter 3

Physics objects used in the analysis

Each collision of protons leads to a large amount of particles. In order to obtain the most accurate reconstruction, the information from all the sub-detector is used: tracks from ID and MS, and clusters from the calorimeters.

An overview of the objects used in the analyses described in the next Chapters: track and vertices, electrons, muons, jets, MET.

3.1 Tracking and vertices

As reported in Ref. [43] several tools have been used in the track reconstruction. The most relevant ones are global-χ^2 and Kalman-filter techniques [54], dynamic noise adjustment [55], Gaussian-sum filters (GSF) [56] and deterministic annealing filters [57]. The reconstruction with the ID involves a pre-processing stage, a track-finding stage and post-processing stage.
The pre-processing stage transforms the raw data from the pixel and SCT detectors to clusters and then the clusters to space-points.
In the track-finding stage track seeds are constructed using space-points in the three pixel layers and the first SCT layer. These tracks are extended throughout the SCT to form track candidates. A fit to the track candidates permits to remove not compatible clusters associated to the track, further quality cuts allow to resolve ambiguities in the cluster-to-track association and to reject fake tracks. The surviving tracks are then extended to the TRT and refitted with the full information of all three detectors and "outliers" hits are removed as well. In order to improve the tracking efficiency for

secondary tracks from conversions or decays of long-lived particles, additional tracks are searched in the unused track segments in the TRT.
In the post-processing stage vertices are finded considering the tracks defined in the previous stages.

The primary vertex, by definition, is the one with the largest sum of asociated-track momenta ($\sum(p_{\mathrm{T}})^2$) and it has at least three tracks with $p_{\mathrm{T}} > 400$ MeV.

3.2 Leptons

Muons are reconstructed in the region $|\eta| < 2.5$ by combining tracks reconstructed in the MS and ID. This analysis uses muon candidates referred to as “Chain 1, CB muons” in Ref. [58].
Electrons are identified within the region $|\eta| < 2.47$, except in the transition region between barrel and end-cap calorimeters ($1.37 < |\eta| < 1.52$), through the association of an ID track to a calorimeter cluster whose shower profile is consistent with an electromagnetic shower [59]. Information from both the calorimetric and tracking system are used for the electron identification. A cut-based approach is adopted In the 7 TeV analysis while a likelihood-based selection is also exploited in the 8 TeV analysis as described in Ref. [60]. In all the analyses looser requirements are adopted for higher-p_{T} leptons than low-p_{T} ones to increase acceptance to signal with poor increase of background acceptance. Tab. 3.1 summarises the lepton identification selections adopted in the different event categories.

Category	p_{T} threshold	Electron identification
3ℓ	$p_{\mathrm{T}} > 15$ GeV	Loose LH ($p_{\mathrm{T}} > 20$ GeV) or Very Tight LH ($p_{\mathrm{T}} < 20$ GeV)
2ℓ	$p_{\mathrm{T}} > 22, 15$ GeV	Medium++ ($p_{\mathrm{T}} > 25$ GeV) or Very Tight LH ($p_{\mathrm{T}} < 25$ GeV)
4ℓ	$p_{\mathrm{T}} > 25, 20, 15, 15$ GeV	Loose LH (p_{T} >20 GeV) or Very Tight LH ($p_{\mathrm{T}} < 20$ GeV)

TABLE 3.1: Summary of lepton identification criteria in the different categories.

For the isolation requirement, both tracking and calorimeter information are used and p_{T}-dependent cuts are applied to the scalar sum of the transverse momenta of other tracks from the primary vertex within a cone around the track (PtCone), and to the scalar sum of the transverse energies measured in calorimeter cells within a cone (EtCone), excluding the energy associated to the particle itself. The electron calorimeter-based isolation algorithm uses topological clusters [60] while a cell-based isolation is used for muons in the calorimeter.
Tab. 3.2 and Tab. 3.3 summarise the lepton isolation criteria adopted in the different event categories.

Category	Cone Size	p_{T} range	Calorimetric isolation EtCone / p_{T}	Tracking isolation PtCone / p_{T}
3ℓ, 4ℓ	$\Delta R = 0.2$	> 20 GeV	< 0.10	< 0.04
		< 20 GeV	< 0.07	< 0.04

TABLE 3.2: Isolation criteria for the 8 TeV analysis adopted for the leptons in the 3ℓ and 4ℓ channels.

Category	Cone Size	E_{T} range	Calorimetric isolation EtCone / $E_{\mathrm{T}}(p_{\mathrm{T}})$	Tracking isolation PtCone / $E_{\mathrm{T}}(p_{\mathrm{T}})$
		> 25 GeV	< 0.28 (0.30)	< 0.10 (0.12)
2ℓ	$\Delta R = 0.3$	20-25 GeV	< 0.28 (0.18)	< 0.10 (0.12)
		< 20 GeV	< 0.24 (0.12)	< 0.08 (0.08)

TABLE 3.3: Isolation criteria for the 8 TeV analysis adopted for the electrons (muons) in the 2ℓ channels.

For all the analysed SRs the same optimised impact parameter cuts used in Ref. [61] are applied. The optimal cuts are found using the same procedure as for the isolation and the identification optimisations. The absolute value of $z_0 \times \sin\theta$ is required to be smaller than 0.4 mm for electrons and 1.0 mm for muons, where z_0 is the longitudinal impact parameter of the track evaluated with respect to the reconstructed primary vertex. The significance of the transverse impact parameter d_0, evaluated with respect to the reconstructed primary vertex, is required to be smaller than three.

3.3 Jets

Jets are reconstructed from three-dimensional topological clusters [62] over the region $|\eta| < 4.5$ using the anti-k_t algorithm [63] with radius parameter $R = 0.4$. Jets are required to have p_{T} larger than 25 GeV except for the forward region, $|\eta| > 2.4$, in which the threshold is raised to 30 GeV. The contamination of jets from pile-up is reduced requiring a Jet Vertex Fraction (JVF) larger than 0.5 (0.75) for the 8 (7) TeV data samples, for all jets with $p_{\mathrm{T}} < 50$ GeV and $|\eta| < 2.4$. The JVF is the ratio of the energy of the tracks associated (within $\Delta R < 0.4$) to the jet with respect to energy of tracks shared between the jet and the primary vertex.
Jets containing a b-hadron are tagged with the MV1 b-jet identification algorithm [64]. In Refs. [65, 66], for b-jets with $|\eta| < 2.5$ and $p_{\mathrm{T}} > 20$ (25) GeV in the 8 (7) TeV data analysis, an efficiency of 85% and a rejection of a factor of 10 against jets originating from light quarks or gluons is estimated using simulated $t\bar{t}$ events.

When a reconstructed lepton (jet) is close, i.e. $\Delta R < 0.1$ (0.35), to another reconstructed lepton, these are considered as generated by the same object. The following rules are used:

- electron-electron or muon-muon, the lepton with higher p_{T} is kept;
- electron-muon, electron is kept;
- electron-jet, electron is kept;
- muon-jet, muon is kept.

3.4 Missing transverse momentum

This study considers two definitions of missing transverse momentum (MET) [67, 68]. A calorimeter-based MET ($\mathbf{E}_{\mathrm{T}}^{\mathrm{miss}}$, whose magnitude is defined as $E_{\mathrm{T}}^{\mathrm{miss}}$) has a large rapidity coverage. The quantity $\mathbf{E}_{\mathrm{T}}^{\mathrm{miss}}$ is calculated as the negative vector sum of the momenta associated to energy deposits in the calorimeter, including contribution from neutral particles and deposits not associated to reconstructed objects ("soft term"). In the 8 TeV analysis, to suppress the pile-up effect, the ratio of the scalar p_{T} sum of all soft term tracks associated with the primary vertex to the scalar p_{T} sum of all soft term tracks from all vertices is employed. This ratio is used to scale all soft-event contributions to $E_{\mathrm{T}}^{\mathrm{miss}}$ [69].
A track-based MET ($\mathbf{p}_{\mathrm{T}}^{\mathrm{miss}}$, whose magnitude is defined as $p_{\mathrm{T}}^{\mathrm{miss}}$) is also used in order to reduce the effects of pile-up on the resolution of the calorimeter-based variant [70]. It is calculated as the vector sum of the transverse momenta of tracks with $p_{\mathrm{T}} > 500$ MeV that originate from the primary vertex. The neutral components of the jets are also included in this calculation replacing the momenta of jet-associated tracks with the energy measured in the calorimeter.

Chapter 4

The VH ($H\rightarrow WW^*$) analysis

A search for Higgs boson production in the VH mode ($H\rightarrow WW^*$) with the Run-1 ATLAS data is presented. Four analyses are considered.
The four-leptons analysis targets the ZH production mode with fully leptonic decay of the Z boson. The main backgrounds to this channel are non-resonant ZZ^* and ZWW^* production.
The three-leptons analysis targets the WH production with fully leptonic decay of the associate W. The most prominent background to this channel is $WZ/W\gamma^*$ production; followed by the non-resonant WWW^* production presenting the same final state as the signal.
The two-leptons Different-Flavour Opposite-Sign (DFOS) analysis is designed to select WH events in which the associated W decays to hadrons. After requiring two leptons of different flavour, the leading backgrounds for this channel are $t\bar{t}$ and Wt processes.
The two-leptons Same-Sign (SS) analysis is designed to select WH events in which one W from the Higgs boson decays hadronically. The main backgrounds in this channel are $WZ/W\gamma^*$, $W\gamma$ and W+jets production, WW, Z+jets and t-quark processes.

Although the three-leptons and two-leptons analyses are designed for the WH associated production, these analyses also have sensitivity to the ZH associated production. Therefore the ZH associated production is treated as signal in all the analyses, and a combined VH search result is obtained from these four analyses. The analyses presented herein were performed in a "blind" way: the algorithms and selection procedures were formally approved and fixed before the results from data in the Signal Region (SR) were examined. The 8 TeV analysis will be described as first. 3ℓ, 4ℓ and 2ℓ-DFOS analyses are also performed on the 7 TeV data sample. Each analysis has been optimised on the 8 TeV sample, which corresponds to a larger integrated luminosity and to more demanding experimental conditions, due to the higher level of pileup, and then applied with minor differences to the 7 TeV data sample as well, this second analysis, whose limited statistics does not allow a full illustration of the selection, will be described later in the Chapter.

The four analyses will be described in this Chapter, focusing on the three-leptons analysis I mainly contributed.

4.1 Physics processes

Higgs boson production in the WH and ZH associated modes, which will collectively be referred to as the VH associated production, provides important information on the Higgs boson couplings to gauge bosons. In particular, in the WH associated production mode with $H \to WW^*$ decay, the Higgs boson couples only to W bosons thus this process is sensitive exclusively to the Higgs to W boson coupling constant. The ZH associated production mode, with $H \to WW^*$ decay, contributes as well to the study of the Higgs couplings to gauge bosons. The Higgs boson decays to a W boson pair with rates compatible with the SM expectation [61]. In the SM, the cross section of the WH and ZH associated production, followed by $H \to WW^*$ decay, is predicted to be 0.151 pb^{-1} and 0.089 pb^{-1}, for $m_H = 125$ GeV [20].
Helicity conservation in the decay of the two W bosons from a scalar Higgs boson leads in general to a small opening angle between the leptons originating from the Higgs boson decay, while additional leptons from the decay of the recoiling boson tend to be at a large angle with respect to the other two. This allows to define a topology based naming scheme which applies to all the channels which is implemented in Fig. 4.1. In the following the pair of opposite sign leptons which are candidate to come from the $H \to WW^*$ decay chain, and appear to be either closer in angle to each other or present the smaller invariant mass, will be called ℓ_0 and ℓ_1. Lepton(s) from the decay of the associated boson are labelled ℓ_2 (ℓ_3).
From the four final states eight Signal Regions are defined through a further split of the categories described in Sec. 4.1.1, Sec. 4.1.2, Sec. 4.1.3 and Sec. 4.1.4 and applying the selections described in the Sec. 4.3. This further splitting permits the optimisation of dedicated selections for each sub-channel in which signal and backround contents are sensitively different as well the signal-to-backround ratio. As example, in the 3ℓ final state, in a SR with no Same Flavour Opposite Sign (SFOS) lepton pairs the main backround involves products of t-quarks decay while backrounds with Z bosons decay products are negligible. The main contribution of such background, on the other hand, is redirected to the complementary SR and it can be reduced using a Multivariate

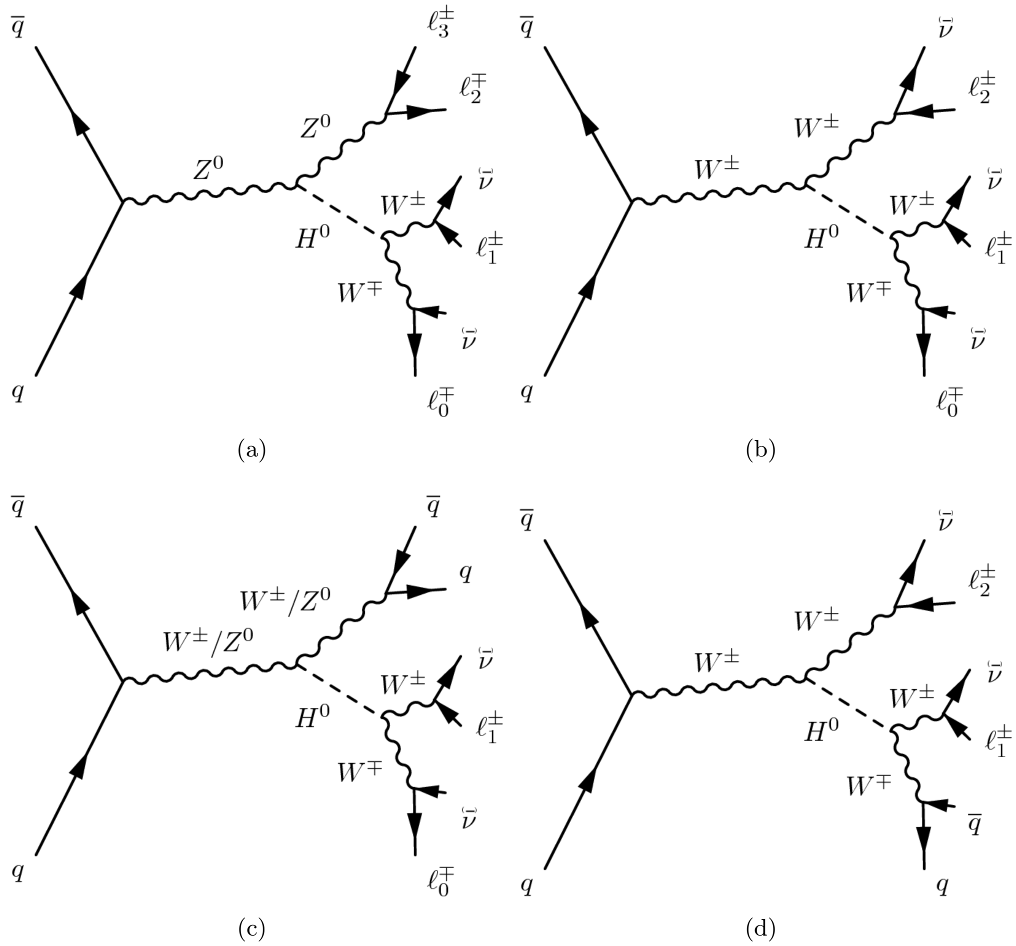

FIGURE 4.1: Tree-level Feynman diagrams of the $VH(H\to WW^*)$ topologies studied in this analysis: (a) 4ℓ channel, (b) 3ℓ channel, (c) 2ℓ-DFOS channel and (d) 2ℓ-SS channel. For charged lepton external lines, the directions of arrows refer to the superscripted sign. Relevant arrows are assigned to the associated neutrino external lines [71].

Analysis (MVA). A summary of the categories and the associated SRs is given in Tab. 4.1.

Channel	Category	Description
3ℓ	3SF	three SF leptons with two possible SFOS pairs (eee and $\mu\mu\mu$)
	1SFOS	three leptons with one SFOS pair ($ee\mu$ and $e\mu\mu$)
	0SFOS	three leptons with no SFOS pair
2ℓ-DFOS	DFOS	two DFOS leptons
2ℓ-SS	1jet	two SS leptons with one jet
	2jets	two SS leptons with two jets
4ℓ	1SFOS	four leptons with one SFOS pair
	2SFOS	four leptons with two SFOS pairs

Table 4.1: Event categories studied in this analysis.

4.1.1 $WH\to W(\ell\nu)WW^{(*)}\to \ell\nu\ell\nu\ell\nu$ phenomenology

The 3ℓ analysis is designed to search this process. The signature studied is three leptons with total charge ±1, eventually in presence of missing transverse momentum. It is common to a number of physics processes which represent the background to the WH signal. The main backgrounds with three real isolated leptons are due to the di-boson production of $WZ/W\gamma^*$, as well as the $ZZ^{(*)}$ production with an undetected lepton. Since the leptons are prompt ones and are isolated, these backgrounds cannot be reduced by the application of tight lepton identification criteria. However these backgrounds are characterised by the presence of at least one pair of Same Flavour Opposite Sign leptons. For this reason the analysis distinguishes between events with at least one pair of SFOS leptons and events without any such pair. The sample with a SFOS pair contains 3/4 of the signal, but suffers from the backgrounds listed above, while the sample without such pairs contains only 1/4 of the signal but is affected mainly by backgrounds that are reducible through lepton identification criteria. The selection criteria are optimised separately for these two samples. Three categories, listed in Tab. 4.1 as 3ℓ-3SF, 3ℓ-1SFOS and 3ℓ-0SFOS, are therefore defined in the 3ℓ channel.
At a significantly lower rate, but comparable to the signal, tri-boson production, in particular $WWW^{(*)}$, represents an irreducible background, while the associated production of $t\bar{t}$ pairs with vector bosons can be reduced through a t-quark veto based on the requirement of no jets identified as generated by a b-quark in the final state.
Final states with fewer than three prompt leptons and/or without real missing transverse momentum may contribute to the background due to instrumental effects. Fake leptons include both jets which have been misidentified as leptons and real non-isolated leptons from light flavour, beauty and charm decays. Background processes with two prompt leptons, such as WW, Z+jets, $t\bar{t}$ and Wt production, must be accompanied by a fake lepton to enter the selection. They can therefore be significantly reduced by isolation requirements on the three leptons. Final states with only one prompt lepton, such as W boson production or single top quarks produced through the s-channel or t-channel, would require two fake leptons and are strongly suppressed by isolation requirements.
The leptons in the event are classified by identifying ℓ_0 as the lepton with unique charge, ℓ_1 as the lepton closer in ΔR to ℓ_0, and ℓ_2 as the remaining one.

4.1.2 $WH\to W(jj)WW^{(*)}\to jj\ell\nu\ell\nu$ phenomenology

The 2ℓ-DFOS analysis is designed for this decay channel. The signature of this channel is the presence of two isolated charged leptons with overall null charge together with two jets from the hadronic decay of the associated W boson. The involved leptons are

labelled ℓ_0 and ℓ_1.
In the analysis only the final state which contains no SFOS lepton pairs is considered. This reduces the Z+jets and di-boson backgrounds that contain one or more Z bosons decaying to a pair of electrons or muons. In such no SFOS data sample, the main background contribution comes from the W+jets, $t\bar{t}$, WW and $Z \to \tau\tau$ productions. W+jets production is reduced significantly by requiring isolation on the two leptons but it still is a major background. To reduce the $t\bar{t}$ production a t-quark veto, which is based on the identification of no b-jets in the final state, is deployed. Rejecting events with lepton pairs with a large invariant mass reduces the $t\bar{t}$ production further as well as the WW production. Rejecting events with a large vectorial p_{T} sum of energetic objects reduces the W+jets and $t\bar{t}$ production by utilising the momentum imbalance of that processes. For the $Z \to \tau\tau$ a dedicated cut on the invariant mass reconstructed with collinear approximation [72] is applied. After all the selections, about a half of total background in the 2ℓ-DFOS comes from the $t\bar{t}$ production, and the remaining contribution is equally shared by W+jets, WW and $Z \to \tau\tau$ production processes.
In the analysis, $t\bar{t}$ and $Z \to \tau\tau$ contributions are normalised by using dedicated control samples, whereas the shape and normalisation of WW prediction is purely relying on Monte Carlo simulations. W+jets estimation is obtained by the data driven method used in Ref. [61].

4.1.3 $WH \to W(\ell\nu)WW^{(*)} \to \ell\nu\ell\nu jj$ phenomenology

The 2ℓ-SS analysis is designed for this decay channel. The signature of this channel is the presence of two isolated charged leptons with overall charge ± 2 together with one or two jets (2ℓ-SS-1jet and 2ℓ-SS2jets in Tab. 4.1 respectively) supposed to be associated with the hadronic decay of one of the two W bosons from the decay of the Higgs boson. The involved leptons are labelled ℓ_1 and ℓ_2, where ℓ_1 is the lepton assumed to come from the decay chain ofthe Higgs boson and is identified as the lepton that minimises the invariant mass with the decay products of the other W boson from the Higgs boson decay, i.e. which minimises $m_{\ell_1 jj}$ in events with two jets or $m_{\ell_1 j}$ when only one jet is present.
Most of the backgrounds in the 2ℓ-SS analysis are reducible. Processes involving fake leptons include the $W\gamma$ and W+jets productions. The W+jets and multi-jets background estimations are obtained by the data driven method used in Ref. [61]. The Z+jets and $t\bar{t}$ productions contribute when a lepton is reconstructed with the wrong charge (charge flip). However, these background processes can be almost entirely eliminated using a cut on missing transverse momentum and a t-quark veto respectively. W^+W^- production also contributes via a charge flip, but is more difficult to eliminate. $WZ/W\gamma^*$, $ZZ^{(*)}$,

and $t\bar{t}$ pair production with an associated vector boson contribute when a lepton is lost due to not passing the identification criteria, p_{T} acceptance, η acceptance, or isolation requirements. Irreducible processes include same sign WW production, $t\bar{t}$ production in association with a vector boson and Wt. The last two are greatly reduced by the use of a t-quark veto, however same sign WW production is difficult to reduce due to its final state sharing many similarities with the signal final state.

4.1.4 $ZH\to ZWW^{(*)}\to \ell\ell\ell\nu\ell\nu$ phenomenology

The 4ℓ analysis is designed for this decay channel. The signature is presence of four leptons with total charge zero, and missing transverse momentum carried away by the neutrinos. The tri-boson processes with the same final state are irreducible backgrounds. The $t\bar{t}Z$ process can also produce four leptons and missing transverse momentum but can be reduced by t-quark veto.
Processes containing fake leptons or fake missing transverse momentum can also contribute to the background. Di-boson production of $WZ/W\gamma^*$+jets with the presence of a fake lepton gives the same topology as the signal but can be reduced through lepton identification criteria. The $ZZ^{(*)} \to \ell\ell\ell\ell$ process with fake missing transverse momentum, from mis-measured jets and/or leptons or due to multiple pp interactions (pileup), can also contribute. The $ZZ^{(*)} \to \ell\ell\ell\ell$ background is characterised by the fact that, when the Z boson does not decay to τ-leptons, the final state consists of two pairs of SFOS leptons. Therefore the distinction based on the number of SFOS pairs is crucial in the ZH analysis, as the sample containing only one SFOS pair (4ℓ-1SFOS in Tab. 4.1) will suffer from a lower background contribution than the sample with two SFOS pairs (4ℓ-2SFOS).
The 2SFOS channel has some acceptance also for the $H \to ZZ^{(*)} \to \ell\ell\ell\ell$ process; to avoid overlaps with other searches [73, 74] this process is removed with a lower cut on the invariant mass of the four leptons.
The reconstruction of the $ZH\to ZWW^{(*)}\to \ell\ell\ell\nu\ell\nu$ decay proceeds through the identification of the two lepton candidates from the recoiling Z boson, hereafter called ℓ_2 and ℓ_3, followed by the identification of the lepton candidates from the Higgs boson decay chain, labelled ℓ_0 and ℓ_1.

4.2 Data and Monte Carlo samples

Focusing on the 8 TeV analysis, the data were selected using inclusive single lepton triggers and di-lepton triggers. The actual thresholds and isolation requirements on the leptons have been tightened with the increase of the instantaneous luminosity of LHC.

As a general rule the unprescaled single lepton triggers with the lowest threshold have been used for the purely leptonic channels (3ℓ and 4ℓ categories) while di-lepton triggers were added in the selections for the 2ℓ channels. Tab. 4.2 and Tab. 4.3 show the trigger selection for the 8 TeV run.

The two main single lepton triggers require the transverse momentum of the lepton with respect to the beam line, p_{T}, to exceed 24 GeV and that the lepton is isolated: the scalar sum of the p_{T} of charged particles within $\Delta R = 0.2$ of the lepton direction is required to be less than 0.10 and 0.12 times the lepton p_{T} for electrons and muons, respectively. Auxiliary triggers for high p_{T} ($p_{\mathrm{T}} > 60$ GeV for electrons, $p_{\mathrm{T}} > 35$ GeV for muons) single leptons without isolation requirement are also used to recover efficiency. The additional di-lepton triggers used for 2ℓ-DFOS and 2ℓ-SS channels select two electrons with $p_{\mathrm{T}} > 12$ GeV, two muons with $p_{\mathrm{T}} > 18$ GeV and $p_{\mathrm{T}} > 8$ GeV, or an electron with $p_{\mathrm{T}} > 12$ GeV and a muon with $p_{\mathrm{T}} > 8$ GeV. In the 2ℓ-DFOS and 2ℓ-SS analysis, W+jets and mulijets background are estimated by using a fake factor method in Ref. [61], and supporting triggers are used to measure the lepton fake probability in the method.

The trigger efficiencies, measured as a function of p_T, η and data-taking period using leptonic Z decays, are approximately 95% for electrons and 90% (70%) for muons in the endcap (barrel) with respect to the offline reconstructed leptons. Normalisation factors have been applied to Monte Carlo to correct the efficiency of each of the used triggers to data.

Optimal data-taking conditions for the detector system are required for an event to be accepted by the offline analysis. The data set used in the 8 TeV analysis corresponds to an integrated luminosity of 20.3 fb^{-1}.

electrons	EF_e24vhi_medium1 OR EF_e60_medium1
muons	EF_mu24i_tight OR EF_mu36_tight

TABLE 4.2: 8 TeV run – trigger selection for 3ℓ and 4ℓ cahnnels.

ee channel	EF_e24vhi_medium1 OR EF_e60_medium1 OR EF_2e12Tvh_loose1 OR EF_2e12Tvh_loose1_L2StarB
$\mu\mu$ channel	EF_mu24i_tight OR EF_mu36_tight OR EF_mu18_tight_mu8_EFFS
$e\mu$ & μe channels	EF_e24vhi_medium1 OR EF_e60_medium1 OR EF_mu24i_tight OR EF_mu36_tight OR EF_e12Tvh_medium1_mu8

TABLE 4.3: 8 TeV run – trigger selection for 2ℓ channels.

In modelling the data with Monte Carlo simulations the signal contribution is given by the associated production process. The gluon fusion production process, the vector boson fusion production process are also considered, and they are treated as backgrounds in the search for the VH process. Monte Carlo simulated signal events are generated using PYTHIA8 [75]. The signal cross sections are then normalised to Next-to-Next-to Leading Order (NNLO) calculations [20, 76, 77, 78, 79]. The Higgs boson decay branching ratios are calculated with HDECAY [80]. The Monte Carlo generators used to model signal and background processes are listed in Tab. 4.4 together with the assumed cross sections and normalisation up to NNLO and next-to-next-to-leading-logarithm (NNLL). The normalisation to the higher order is performed introducing a scale factors referred as k-factor. For the backgrounds for which a control region is built, the normalisation is then corrected using data. To model W production, ALPGEN [81] interfaced to PYTHIA6 is used, while it is interfaced to HERWIG [82] using the MLM matching scheme [83] to model the production of $Z/\gamma^{(*)}$ bosons in association with jets (Drell-Yan). In 3ℓ analysis, in order to have a better modelling of real photon radiation, the $Z\gamma$ production (with a real photon) is simulated with the SHERPA [84] generator. The duplicated phase space, involving Final-State-Radiation (FSR) of photons, is removed from ALPGEN with a dedicated filter. Electroweak Z/γ^* production with two jets is modelled with SHERPA. In 2ℓ and 4ℓ analyses the Z/γ^* production is treated as a part of $Z/\gamma^{(*)}$ process, which is modelled by ALPGEN+HERWIG.

Processes involving t-quarks are normalised to higher order available in Ref. [85]. The $t\bar{t}$ production is simulated with POWHEG [86] with PYTHIA6 for the parton shower and hadronisation. ACERMC [87], using PYTHIA6 for showering and hadronisation, is used for the generation of single t-quark quark production in the t-channel. For Wt and s-channel production POWHEG interfaced to PYTHIA6 is used while for Zt production MADGRAPH [88, 89] interfaced to PYTHIA6 is used. The $t\bar{t}W$ and $t\bar{t}Z$ backgrounds are generated with MADGRAPH interfaced to PYTHIA6.

POWHEG with PYTHIA6 with Perugia tune [90] is used for the generation of $WZ/W\gamma^*$ (with $m_{\gamma^*} > 7$ GeV) production and for WW production with the exception of the 2ℓ-DFOS channel, in which the latter is modelled with SHERPA. An additional contribution to the WW background from gluon-initiated diagrams is modelled using gg2WW [91] interfaced to HERWIG. WW+2jets and WZ+2jets processes are generated with SHERPA. $W\gamma$ production (with a real photon) is modelled with ALPGEN while SHERPA is employed for $WZ/W\gamma^*$ [92] (with $m_{\gamma^*} < 7$ GeV). The $ZZ^{(*)}$ final states, including the low mass Z^*/γ^* (an off-shell photon) contribution are modelled by two generators: POWHEG interfaced with PYTHIA8 for the invariant masses of the two SFOS lepton pairs larger than 4 GeV and SHERPA when one mass of the two SFOS lepton pairs is smaller than 4 GeV. The additional gluon-initiated diagrams are modelled using gg2ZZ [93] interfaced to HERWIG and JIMMY [94]. Electroweak $ZZ^{(*)}$ production with two jets is modelled with SHERPA. For the tri-boson production (VVV) simulation MADGRAPH [88, 89]

interfaced to Pythia is used. A k-factor of 1.5 is introduced to account for NLO cross section correction [95] to cross sections of the WWW^*, ZWW^* and ZZZ^* backgrounds. The CT10 parton distribution function (PDF) set [96] is used for the MC@NLO samples and the Powheg samples; CTEQ6L1 [97] is used for the Alpgen, MadGraph and Pythia samples, with the Alpgen $Z/\gamma^{(*)}$ sample reweighted to the MRSTMCal [98] PDF set as this better models the lepton kinematics [99]. Wherever parton showering is performed with Herwig, Jimmy [94] is used for the simulation of the underlying event. Acceptances and efficiencies are obtained for most processes from a full simulation [100] of the ATLAS detector using GEANT4 [101]. Given that the data reconstruction is affected by the detector response to pileup a realistic treatment of the pileup conditions is included in the simulation. In the 2012 data the average number of pileup is about 20 (Fig. 2.3).
All samples are processed using the full ATLAS detector simulation [100] based on Geant4 [101], except for WH, $WZ/W\gamma^*$ with $m_{\ell\ell} > 7$ GeV, $q\bar{q}/qg \to WW$, $WW\gamma^*$, $t\bar{t}$ and single top, which are instead simulated with Atlfast-II [102], a parameterisation of the response of the electromagnetic and hadronic calorimeters, and with Geant4 for other detector components. The events are reweighted to ensure that the distribution of pile-up observed in the data is correctly reproduced.

In the plots and tables in the analysis, similar processes are presented collectively as a single category. Tab. 4.5 shows the categorisation of the physics processes listed in Tab. 4.4 in each analysis. The names of the categories are used in plots and tables in the analysis. A set of plots and tables are reported from the publication in Ref. [71], where a simplified categorisation has been used: V, VV, VVV backgrounds following the number of involved vector bosons; t-quark processes; other Higgs involving ggF/VBF production.

4.3 Event selection

This Section describes the variables and the selections identified in each analysis for the optimal extraction of the signal from the background. The background expectations are taken from the simulation and are normalised when needed through the application of the normalisation factors discussed in Sec. 4.5.
The channels studied in this analysis have various common features.

- The presence in the final state of at least two high p_{T} leptons. The applied thresholds are listed in Tab. 3.1.

Process	Generator	$\sigma(\times\text{Br})$ [pb]	Cross-section normalisation
Higgs boson			
VH $(H \to WW^*)$	Pythia [75, 103] v8.165	0.24	NNLO QCD + NLO EW
VH $(H \to \tau\tau)$	Pythia v8.165	0.07	NNLO QCD + NLO EW
$gg \to H$ $(H \to WW^*)$	Powheg-Box [104, 105, 106, 107] v1.0 (r1655)+ Pythia v8.165	4.1	NNLO+NNLL QCD + NLO EW
VBF $(H \to WW^*)$	Powheg-Box [108] v1.0 (r1655)+ Pythia v8.165	0.34	NNLO QCD + NLO EW
$t\bar{t}$H $(H \to WW^*)$	Pythia v8.165	0.028	NLO
Single boson			
$Z/\gamma^*(\to \ell\ell)$+jets ($m_{\ell\ell} > 10$ GeV)	Alpgen [81] v2.14 + Herwig [82] v6.52	16540	NNLO
HF $Z/\gamma^*(\to \ell\ell)$+jets ($m_{\ell\ell} > 30$ GeV)	Alpgen v2.14 + Herwig v6.52	126	NNLO
VBF $Z/\gamma^*(\to \ell\ell)$ ($m_{\ell\ell} > 7$ GeV)	Sherpa [84] v1.4.1	5.3	LO
Top-quark			
$t\bar{t}$	Powheg-Box[109] v1.0 (r2129)+Pythia v6.428	250	NNLO+NNLL
	MC@NLO [105] v4.03		
$t\bar{t}W/Z$	MadGraph [89] v5.1.5.2	0.35	LO
tqb	AcerMC [87] v3.8 +Pythia v6.428	88	NNLL
tb, tW	Powheg-Box [110, 111] v1.0 (r2092)+ Pythia v6.428	28	NNLL
tZ	MadGraph v5.1.5.2 v6.428	0.035	LO
Dibosons			
$WZ/W\gamma^*(\to \ell\ell\ell\nu)(m_{\ell\ell} > 7$ GeV)	Powheg-Box[112] v1.0 (r1508)+Pythia v8.165	12.7	NLO
$WZ/W\gamma^*(\to \ell\ell\ell\nu)$(min. $m_{\ell\ell} < 7$ GeV)	Sherpa v1.4.1	12.2	NLO
other WZ	Powheg-Box[112] v1.0 (r1508) + Pythia v8.165	21.2	NLO
$q\bar{q}/qg \to Z^{(*)}Z^{(*)}(\to \ell\ell\ell\ell, \ell\ell\nu\nu)$ ($m_{\ell\ell} > 4$ GeV)	Powheg-Box[112] v1.0 (r1556) +Pythia v8.165	1.24	NLO
$q\bar{q}/qg \to Z^{(*)}Z^{(*)}(\to \ell\ell\ell\ell, \ell\ell\nu\nu)$ (min. $m_{\ell\ell} < 4$ GeV)	Sherpa v1.4.1	7.3	NLO
other $q\bar{q}/qg \to ZZ$	Powheg-Box[112] v1.0 (r1556) + Pythia v8.165	6.9	NLO
$gg \to Z^{(*)}Z^{(*)}$	gg2ZZ [93] v3.1.2 + Herwig v6.52 (8 TeV only)	0.59	LO
$q\bar{q}/qg \to WW$	Powheg-Box[112] v1.0 (r1556) + Pythia v6.428	545	NLO
	Sherpa v1.4.1 (for 2ℓ-DFOS 8 TeV only)	54	NLO
$gg \to WW$	gg2WW [91] v3.1.2 + Herwig v6.52	1.9	LO
VBS WZ, $ZZ(\to \ell\ell\ell\ell, \ell\ell\nu\nu)$ ($m_{\ell\ell} > 7$ GeV), WW	Sherpa v1.4.1	1.2	LO
$W\gamma$ ($p_{\mathrm{T}}^{\gamma} > 8$ GeV)	Alpgen v2.14 +Herwig v6.52	1140	NLO
$Z\gamma$ ($p_{\mathrm{T}}^{\gamma} > 8$ GeV)	Sherpa v1.4.3	960	NLO
Tribosons			
$WWW^*, ZWW^*, ZZZ^*, WW\gamma^*$	MadGraph v5.1.3.33	0.44	NLO

Table 4.4: MC generators used to model the signal and background processes. The Higgs boson samples are normalised using the production cross section and the decay branching fraction computed for $m_H = 125$ GeV. The values reported for the VH $(H \to WW^*)$ process include the NNLO contribution from the $gg \to ZH$ $(H \to WW^*)$ process. The corresponding cross section times branching fraction of the $H \to WW^*$ decay, $\sigma \times \text{Br}$, are shown for the Higgs production processes, while for background processes the production cross section, including the effect of the leptonic branching fraction, and the $m_{\ell\ell}$ and p_T^{γ} cuts, as specified in the "Process" column, is presented. 'HF' refers to heavy-flavour jet production, and 'VBS' refers to vector boson scattering. When a lower cut on $m_{\ell\ell}$ is specified, it is applied to all SFOS lepton pairs, while when an upper cut is indicated it is applied to the SFOS pair of lowest mass in the event. For the Sherpa1.1 $Z^{(*)}Z^{(*)}$ sample a lower cut of 4 GeV is applied, in addition, to the SFOS lepton pair of higher mass. Cross sections are computed to different levels of accuracy (LO, NLO, NNLO or next-to-next-to-leading-logarithm, NNLL), as specified by the last column [71]

<table>
<tr><th>Process</th><th>3ℓ cat.</th><th>2ℓ-DFOS cat.</th><th>2ℓ-SS cat.</th><th>4ℓ cat.</th></tr>
<tr><td>WH/ZH</td><td>VH</td><td>VH</td><td>VH</td><td>VH</td></tr>
<tr><td>ggF</td><td>ggF</td><td>ggF</td><td>ggF</td><td>ggF</td></tr>
<tr><td>VBF</td><td>VBF</td><td>VBF</td><td>VBF</td><td>—</td></tr>
<tr><td>$t\bar{t}$H</td><td>$t\bar{t}$H</td><td>—</td><td>—</td><td>—</td></tr>
<tr><td>inclusive W</td><td rowspan="2">—</td><td rowspan="2">W+jets</td><td rowspan="2">W+jets</td><td rowspan="2">—</td></tr>
<tr><td>inclusive W+HF</td></tr>
<tr><td>inclusive Z/γ^* high mass</td><td rowspan="4">$Z/\gamma*$</td><td rowspan="4">$Z/\gamma*$</td><td rowspan="4">$Z/\gamma*$</td><td rowspan="4">$Z/\gamma*$</td></tr>
<tr><td>inclusive Z/γ^* low mass</td></tr>
<tr><td>inclusive Z/γ^*+HF</td></tr>
<tr><td>$Z/\gamma^* + 2$ jets (EWcoupling)</td></tr>
<tr><td>inclusive $Z\gamma$</td><td>$Z\gamma$</td><td colspan="3">This process is treated as a part of $Z/\gamma*$</td></tr>
<tr><td>$t\bar{t}$</td><td rowspan="6">t-quark</td><td rowspan="6">t-quark</td><td rowspan="6">t-quark</td><td rowspan="5">—</td></tr>
<tr><td>tqb</td></tr>
<tr><td>tb</td></tr>
<tr><td>tW</td></tr>
<tr><td>tZ</td></tr>
<tr><td>$t\bar{t}W/Z$</td><td>$t\bar{t}V$</td></tr>
<tr><td>$q\bar{q}/g \to WW$</td><td rowspan="3">WW</td><td rowspan="3">WW</td><td rowspan="3">WW</td><td rowspan="3">—</td></tr>
<tr><td>$gg \to WW$</td></tr>
<tr><td>$WW + 2$ jets (6EWcoupling)</td></tr>
<tr><td>$WZ/W\gamma^*(m_{(Z/\gamma^*)} > 7)$ GeV</td><td rowspan="3">$WZ/W\gamma^*$</td><td rowspan="4">$WZ/W\gamma^*$</td><td rowspan="3">$WZ/W\gamma^*$</td><td rowspan="4">$WZ/W\gamma^*$</td></tr>
<tr><td>$WZ/W\gamma^*(m_{(Z/\gamma^*)} < 7)$ GeV</td></tr>
<tr><td>$WZ + 2$ jets (6EWcoupling)</td></tr>
<tr><td>$W\gamma$</td><td>$W\gamma$</td><td>$W\gamma$</td></tr>
<tr><td>$q\bar{q}/g \to Z^{(*)}Z^{(*)} \to 4l$</td><td rowspan="4">$ZZ^*$</td><td rowspan="4">$ZZ^*$</td><td rowspan="4">$ZZ^*$</td><td rowspan="4">$ZZ^*$</td></tr>
<tr><td>$q\bar{q}/g \to Z^{(*)}Z^{(*)} \to 4l$ low mass</td></tr>
<tr><td>$gg \to Z^{(*)}Z^{(*)} \to 4l$</td></tr>
<tr><td>$ZZ + 2$ jets (6EWcoupling)</td></tr>
<tr><td>$WWW^*, ZWW^*, ZZZ^*, WWg^*$</td><td>$VVV$</td><td>$VVV$</td><td>$VVV$</td><td>$VVV$</td></tr>
<tr><td>QCD</td><td>—</td><td>QCD</td><td>QCD</td><td>—</td></tr>
</table>

TABLE 4.5: Process categorisation in each analysis.'—' represents a null contribution.

- The low multiplicity of jets in the final state but for the ones from the decay of one of the vector bosons in the 2ℓ-SS and 2ℓ-DFOS channels. In the following only events with at most one jet will be considered for the 3ℓ and 4ℓ channels, with one or two jets for the 2ℓ-SS channel, and with two jets for the 2ℓ-DFOS channel.

- The absence of jets from the hadronisation of b-quarks. This is an important feature which allows to to contrast the background induced by events containing the t-quark(s) .

- Whenever a SFOS lepton pair is present, besides the $\ell_2\ell_3$ pair in the 4ℓ channel, a selection on its invariant mass is applied rejecting events in the low mass region and in the mass window around the Z boson pole to reduce the background from inclusive γ^* and Z production respectively.

Category	Pre-selection
3ℓ 3ℓ pre-selection	three isolated leptons with $p_{\mathrm{T}} > 15$ GeV trigger match, total charge $\pm$ 1
2ℓ-DFOS DFOS pre-selection	two isolated leptons with different flavour and $p_{\mathrm{T}} > 22, 15$ GeV trigger match, total charge zero
2ℓ-SS SS pre-selection	two isolated leptons with $p_{\mathrm{T}} > 10$ GeV trigger match, total charge $\pm$ 2
4ℓ 4ℓ pre-selection	four isolated leptons with $p_{\mathrm{T}} > 15$ GeV containing at least one SFOS pair trigger match, total charge zero

TABLE 4.6: Summary of pre-selection cuts in the different categories.

- All the channels under study have at least two neutrinos in the final state, however their transverse momenta can partly balance each other, therefore the requirement of a minimum $E_{\mathrm{T}}^{\mathrm{miss}}$ in the event is applied only for the channels in which a further reduction of the background from Z+jets production is needed.
- The decay products of the Higgs boson decay tend to be close to each other and separate from the associate vector boson decay ones. The angular separation or the invariant mass between the candidate decay products are the preferred discriminating variables.

In the following, the selections on the number of isolated leptons with the identification criteria described in Sec. 3.2, and the requirements on the total charge of the leptonic system, are called pre-selections and are summarised in Tab. 4.6.
In all the analyses at least one lepton in an event is required to match one of the triggers in Tab. 4.2 and Tab. 4.3. In the matching, leptons are required to have a p_{T} higher enough to be in the plateau of the trigger efficiency. The trigger scale factors have been applied on each lepton in MC taking the correlation between single and di-lepton triggers into account, and regardless of the result of the trigger matching. In the application of the scale factor the trigger efficiency is assumed to be zero below a certain threshold to avoid the difficulty of the turn-on modelling.

Hereafter, the MC distributions are scaled with the NFs reported in Tab. 5.1, evaluated according to the statistical treatment described in Sec. 5.1; the error band in plots includes statistical uncertainty on the event yield, experimental systematic uncertainties, theoretical systematic uncertainties and the statistical component of fitting uncertainties on the background NFs; the last bin of the plots contains the overflow event. The result of the Kolmogor-Smirnov (KS) test [113] is reported on the left top of plots as a measure of the agreement between data and MC distributions.

The 3ℓ analysis is further described in Sec. 4.4, details of the $2\ell/4\ell$ analyses can be found in Ref. [71].

4.4 3ℓ analysis

The 3ℓ pre-selection requires exactly three isolated leptons with $p_{\mathrm{T}} > 15$ GeV of total charge ±1, one of which should be matched to the trigger. The pre-selection suppresses completely some background sources which will not be discussed further in the following. These are inclusive W boson production and production of $b\bar{b}$ pairs. A contribution from single top production, despite the reduction due to the isolation requirements, is present at all the stages of the event selection and is treated in plots and tables together with the $t\bar{t}$ one.
For the event selection, events are divided into 3SF+1SFOS and 0SFOS samples, the former has at least one SFOS lepton pair and the latter has not. In order to reduce the $t\bar{t}$ background, events are then required to contain at most one jet of transverse momentum above 25 GeV (Fig. 4.2). The background from t-quark production is further suppressed by vetoing the presence on any b-tagged jet with p_{T} above 20 GeV (Fig. 4.2 (c) and (d)). This requirement will be referred to as "t-quark veto" in the following. In order to select final states with neutrinos escaping detection, $E_{\mathrm{T}}^{\mathrm{miss}}$ is required to be above 30 GeV and $p_{\mathrm{T}}^{\mathrm{miss}}$ above 20 GeV in 3SF+1SFOS (Fig. 4.3). Due to the lower backgrounds in the 0SFOS category, $E_{\mathrm{T}}^{\mathrm{miss}}$ selections are not required. Masses of all SFOS pairs are required to be at least 25 GeV away from the Z boson mass, which is only applicable to the 3SF+1SFOS sample. This requirement suppresses the $WZ/W\gamma^*$ and ZZ^* irreducible backgrounds and further reduces the Drell-Yan backgrounds (Fig. 4.4). A lower threshold is set on the smallest invariant mass of opposite sign leptons at 12 GeV and 6 GeV in the 3SF+1SFOS and 0SFOS samples respectively. In addition, an upper threshold is set on the largest invariant mass of opposite sign leptons at 200 GeV in both cases. These selections reject events from a region which could be populated by heavy flavour backgrounds and reduce the $WZ/W\gamma^*$ background. The latter can present large mass values since, in addition to the s-channel that is present also in WH production, it can proceed through the t- and u-channels (Fig. 4.5).
The angular separation between ℓ_0 and ℓ_1, $\Delta R_{\ell_0,\ell_1}$, is required to be smaller than two in 3SF+1SFOS. This cut favours the Higgs boson decay topology with respect to that of $WZ/W\gamma^*$ events (Fig. 4.6). The above selections result from an optimisation which minimises the expected limit for a Higgs boson of mass 125 GeV produced in the WH associated production mode.
The lepton identification and isolation criteria are different with respect to what have been adopted in the $H\to WW^*$ ggF, VBF [61] and in 2ℓ-SS analysis, thus some small overlap between the selected events may occur and has to be removed. These selections are labelled as "SS-leptons OR" and "$\ell\nu\ell\nu$ OR" in the cutflow tables.
Tab. 4.8 and Tab. 4.9 summarise the effect of the different cuts on Monte Carlo samples. It is possible to observe the different signal over VV ratio between 3SF and 1SFOS,

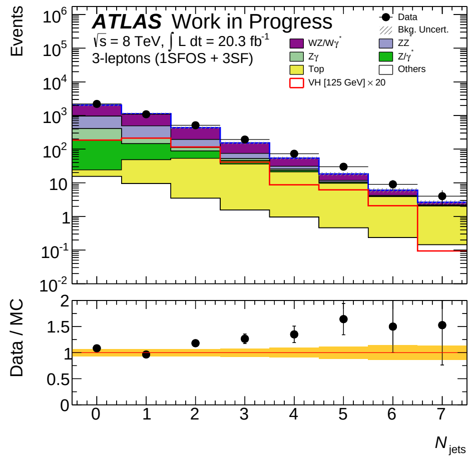

(a)

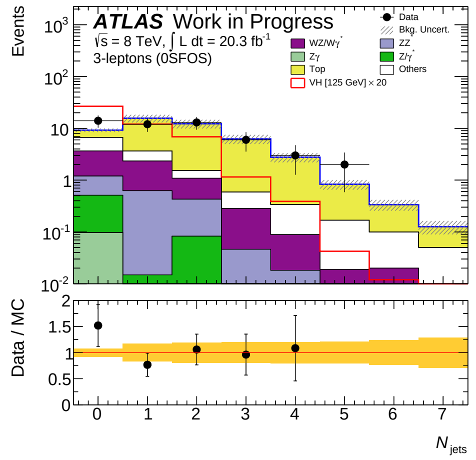

(b)

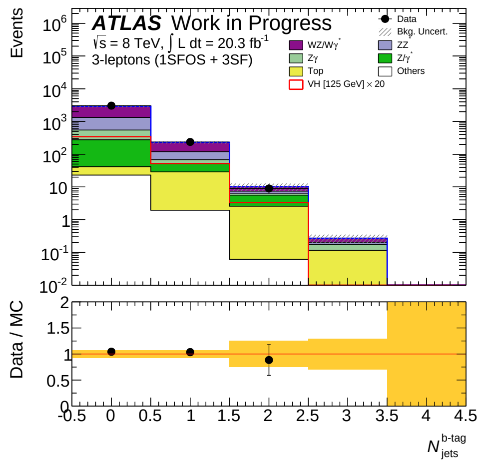

(c)

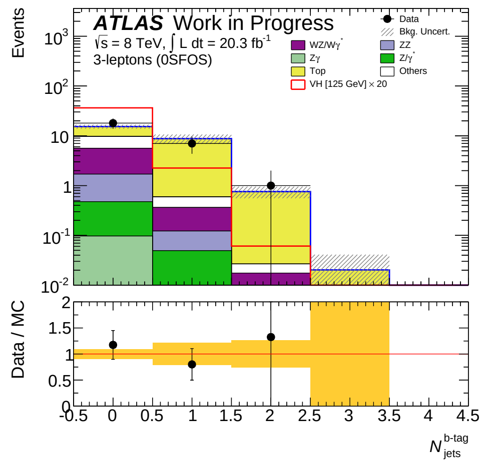

(d)

FIGURE 4.2: MC distributions after pre-selection: (a) number of jets with p_{T} above 25 GeV in 3SF+1SFOS, (b) number of jets with p_{T} above 25 GeV in the 0SFOS sample, (c) number of b-tagged jets in the 3SF+1SFOS sample, and (d) number of b-tagged jets in the 0SFOS sample. The background expectation from the simulation of the background components is shown as a stacked filled histograms. Expectations for SM Higgs boson associated production with $m_H = 125$ GeV are multiplied by a factor 20 and presented as a non-stacked unfilled histogram.

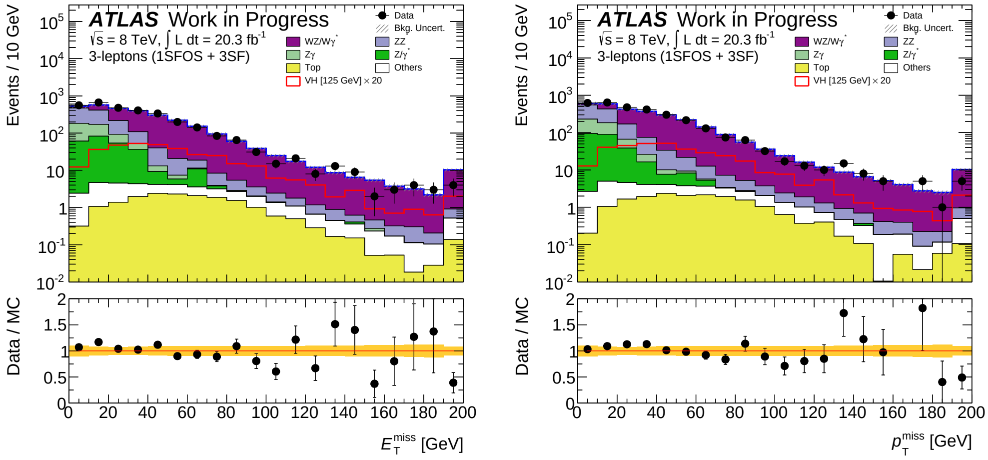

(a) (b)

FIGURE 4.3: MC distributions after the t-quark veto in the 3SF+1SFOS sample: (a) $E_{\mathrm{T}}^{\mathrm{miss}}$, (b) $p_{\mathrm{T}}^{\mathrm{miss}}$. The background expectation from the simulation of the background components is shown as a stacked filled histograms. Expectations for SM Higgs boson associated production with $m_H = 125$ GeV are multiplied by a factor 20 and presented as a non-stacked unfilled histogram.

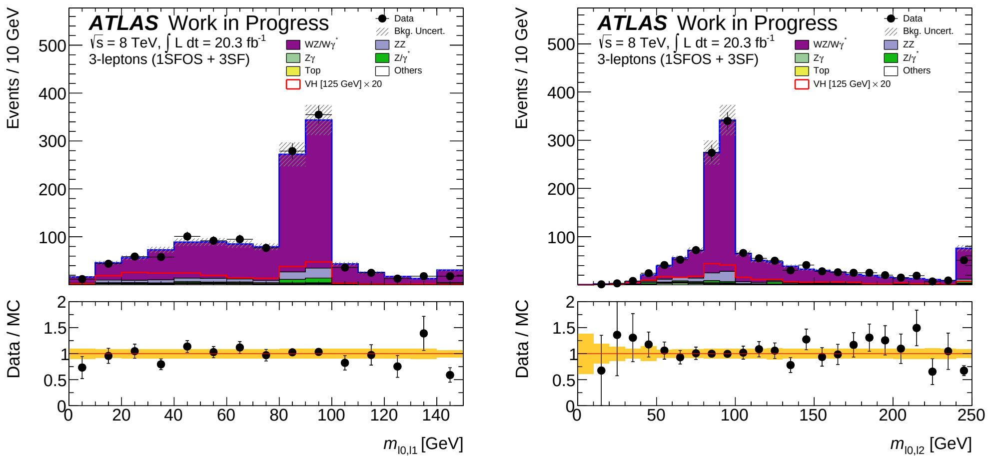

(a) (b)

FIGURE 4.4: MC distributions after $E_{\mathrm{T}}^{\mathrm{miss}}$ selections in the 3SF+1SFOS sample: (a) the invariant mass of the opposite sign lepton-pair with smaller ΔR, (b) the invariant mass of the opposite sign lepton-pair with larger ΔR. The background expectation from the simulation of the background components is shown as a stacked filled histograms. Expectations for SM Higgs boson associated production with $m_H = 125$ GeV are multiplied by a factor 20 and presented as a non-stacked unfilled histogram.

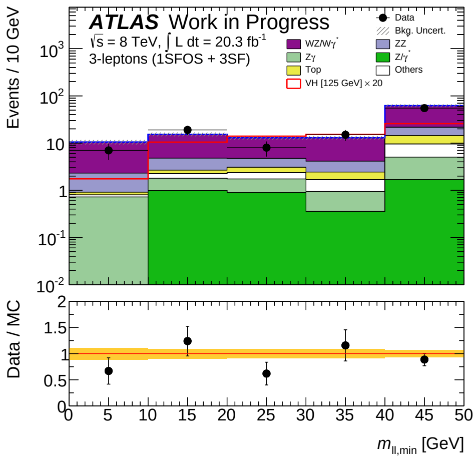

(a)

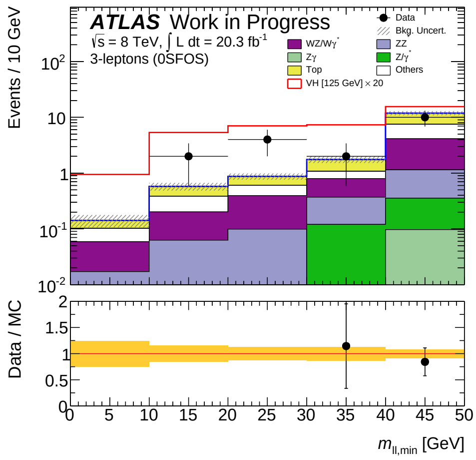

(b)

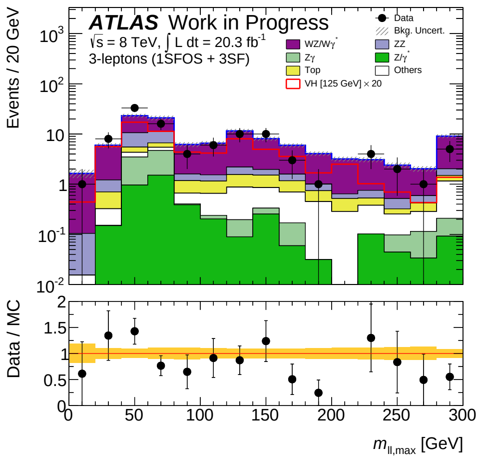

(c)

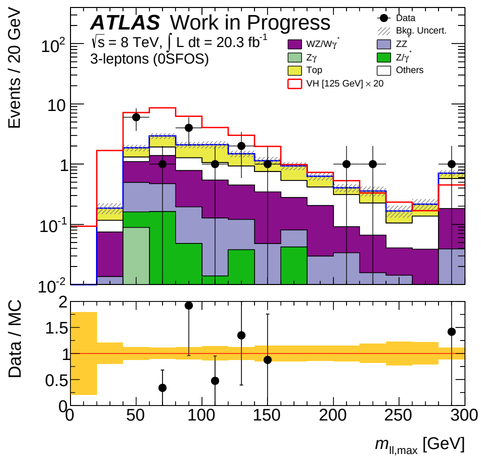

(d)

FIGURE 4.5: MC distributions after the Z-mass veto in the 3SF+1SFOS sample and after the t-quark veto in the 0SFOS: (a) smallest invariant mass of opposite sign leptons in the 3SF+1SFOS sample, (b) smallest invariant mass of opposite sign leptons in the 0SFOS sample, (c) largest invariant mass of opposite sign leptons in the 3SF+1SFOS sample, and (d) largest invariant mass of opposite sign leptons in the 0SFOS sample. The background expectation from the simulation of the background components is shown as a stacked filled histograms. Expectations for SM Higgs boson associated production with $m_H = 125$ GeV are multiplied by a factor 20 and presented as a non-stacked unfilled histogram.

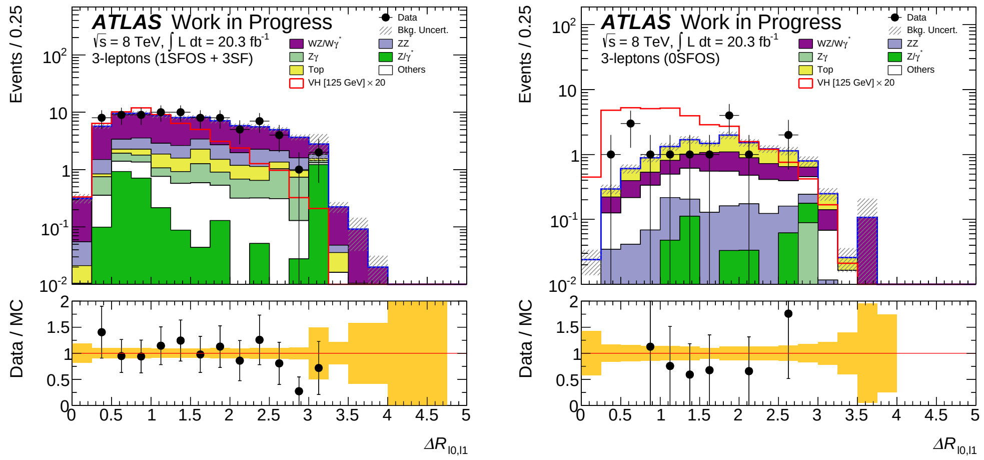

(a)

(b)

FIGURE 4.6: MC distributions after $m_{\ell\ell}^{min}$ and $m_{\ell\ell}^{max}$ selections: (a) $\Delta R_{\ell_0,\ell_1}$ in the 3SF+1SFOS sample, (b) $\Delta R_{\ell_0,\ell_1}$ in the 0SFOS sample. The background expectation from the simulation of the background components is shown as a stacked filled histograms. Expectations for SM Higgs boson associated production with $m_H = 125$ GeV are multiplied by a factor 20 and presented as a non-stacked unfilled histogram.

which is the reason why the two categories are considered separately, although the selections are the same.

The above selection is complemented by the discrimination between signal and background based on the shape of the $\Delta R_{\ell_0,\ell_1}$ variable in the 0SFOS and of a multivariate classifier in 3SF and 1SFOS, as discussed in Sec. 4.4.1 and Sec. 5.2.

Signal Selections		
Cut	3SF+1SFOS	0SFOS
Pre-selection	3 isolated leptons (p_{T}>15 GeV), trigger, total charge ± 1	
Jet multiplicity	$N_{\mathrm{jet}} \leq 1$	
t-quark veto	$N_{b-\mathrm{tag}} = 0$	
$E_{\mathrm{T}}^{\mathrm{miss}}$ cut	$E_{\mathrm{T}}^{\mathrm{miss}}$> 30 GeV, $p_{\mathrm{T}}^{\mathrm{miss}}$> 20 GeV	
Di-lepton mass cuts	$\lvert m_{\ell\ell} - m_Z \rvert > 25$ GeV, $m_{\ell\ell}^{min} > 12$ GeV, $m_{\ell\ell}^{max} < 200$ GeV	$m_{\ell\ell}^{min} > 6$ GeV, $m_{\ell\ell}^{max} < 200$ GeV
Angular cut	$\Delta R_{\ell_0 \ell_1} < 2.0$	
SS-lepton overlap removal	remove overlap with SS-lepton analysis (SS-leptons OR)	
ggF/VBF Overlap removal	remove overlap with ggF/VBF $H \to WW$ analysis ($\ell\nu\ell\nu$ OR)	

TABLE 4.7: Summary of the selection criteria defining the 3ℓ signal regions.

	$W(H \to WW)$	$Z(H \to WW)$	$W(H \to \tau\tau)$	$Z(H \to \tau\tau)$	VH (125 GeV)	Total Bkg.	sign.	Obs.	Data/MC	Data/(MC+Sig)
Pre-selection ($\ell\ell\ell$)	6.78 ± 0.76	20.4 ± 2.9	1.21 ± 0.15	2.61 ± 0.30	31.0 ± 4.0	3879 ± 513	0.497 ± 0.086	4166	1.07 ± 0.12	1.07 ± 0.12
3SF + 1SFOS ($\ell\ell\ell$)	5.12 ± 0.60	20.0 ± 2.9	0.92 ± 0.12	2.57 ± 0.30	28.6 ± 3.9	3832 ± 509	0.462 ± 0.088	4116	1.07 ± 0.14	1.07 ± 0.14
num. jets < 2 ($\ell\ell\ell$)	4.59 ± 0.54	12.5 ± 1.9	0.81 ± 0.11	1.96 ± 0.24	19.9 ± 2.8	3165 ± 423	0.353 ± 0.069	3295	1.04 ± 0.14	1.03 ± 0.14
top-veto ($\ell\ell\ell$)	4.33 ± 0.52	10.4 ± 1.7	0.76 ± 0.10	1.55 ± 0.21	17.1 ± 2.5	2911 ± 389	0.316 ± 0.062	3049	1.05 ± 0.14	1.04 ± 0.14
$E_{T,STVF}^{miss}$ and $E_{T,TrackHWW}^{miss}$ cuts ($\ell\ell\ell$)	3.49 ± 0.42	6.9 ± 1.1	0.521 ± 0.073	1.03 ± 0.14	11.9 ± 1.7	1280 ± 143	0.333 ± 0.061	1282	1.00 ± 0.12	0.99 ± 0.11
Z mass veto ($\ell\ell\ell$)	2.51 ± 0.30	0.52 ± 0.13	0.271 ± 0.041	0.069 ± 0.014	3.37 ± 0.45	113 ± 17	0.314 ± 0.064	104	0.92 ± 0.17	0.89 ± 0.16
$m_{ll,min}$ and $m_{ll,max}$ cuts ($\ell\ell\ell$)	2.18 ± 0.26	0.395 ± 0.097	0.250 ± 0.038	0.055 ± 0.011	2.88 ± 0.37	80 ± 13	0.319 ± 0.067	81	1.01 ± 0.20	0.97 ± 0.19
$\Delta R_{ll} < 2.0$ ($\ell\ell\ell$)	2.06 ± 0.25	0.351 ± 0.091	0.173 ± 0.027	-	2.62 ± 0.34	57.1 ± 8.5	0.344 ± 0.068	62	1.08 ± 0.21	1.04 ± 0.20
SS-leptons OR ($\ell\ell\ell$)	2.05 ± 0.23	0.351 ± 0.090	0.173 ± 0.027	-	2.62 ± 0.32	57.0 ± 6.7	0.344 ± 0.059	62	1.09 ± 0.19	1.04 ± 0.18
$\ell\nu\ell\nu$ OR ($\ell\ell\ell$)	2.00 ± 0.24	0.347 ± 0.090	0.170 ± 0.027	-	2.56 ± 0.33	55.3 ± 8.2	0.341 ± 0.067	60	1.09 ± 0.21	1.04 ± 0.20
3SF ($eee + \mu\mu\mu$)	1.75 ± 0.21	9.9 ± 1.5	0.336 ± 0.049	1.22 ± 0.15	13.2 ± 1.9	1844 ± 268	0.308 ± 0.063	1982	1.07 ± 0.16	1.07 ± 0.16
num. jets < 2 ($eee + \mu\mu\mu$)	1.56 ± 0.19	6.5 ± 1.1	0.277 ± 0.041	0.94 ± 0.12	9.3 ± 1.4	1530 ± 223	0.238 ± 0.050	1602	1.05 ± 0.16	1.04 ± 0.15
top-veto ($eee + \mu\mu\mu$)	1.48 ± 0.18	5.37 ± 0.93	0.261 ± 0.039	0.74 ± 0.10	7.8 ± 1.2	1412 ± 206	0.209 ± 0.045	1475	1.04 ± 0.16	1.04 ± 0.15
$E_{T,STVF}^{miss}$ and $E_{T,TrackHWW}^{miss}$ cuts ($eee + \mu\mu\mu$)	1.18 ± 0.15	3.42 ± 0.64	0.177 ± 0.028	0.494 ± 0.071	5.28 ± 0.87	640 ± 85	0.208 ± 0.044	635	0.99 ± 0.14	0.98 ± 0.14
Z mass veto ($eee + \mu\mu\mu$)	0.703 ± 0.088	0.29 ± 0.11	0.058 ± 0.013	-	1.08 ± 0.19	43.5 ± 8.6	0.163 ± 0.043	32	0.74 ± 0.19	0.72 ± 0.19
$m_{ll,min}$ and $m_{ll,max}$ cuts ($eee + \mu\mu\mu$)	0.598 ± 0.074	0.194 ± 0.075	0.053 ± 0.013	-	0.87 ± 0.14	29.3 ± 6.3	0.159 ± 0.043	25	0.85 ± 0.25	0.83 ± 0.24
$\Delta R_{ll} < 2.0$ ($eee + \mu\mu\mu$)	0.570 ± 0.071	0.172 ± 0.072	-	-	0.80 ± 0.13	21.6 ± 3.7	0.171 ± 0.040	22	1.02 ± 0.28	0.98 ± 0.27
SS-leptons OR ($eee + \mu\mu\mu$)	0.569 ± 0.065	0.172 ± 0.072	-	-	0.80 ± 0.12	21.5 ± 2.7	0.171 ± 0.034	22	1.02 ± 0.25	0.99 ± 0.24
$\ell\nu\ell\nu$ OR ($eee + \mu\mu\mu$)	0.563 ± 0.060	0.168 ± 0.072	-	-	0.79 ± 0.12	21.2 ± 2.6	0.170 ± 0.030	22	1.04 ± 0.24	1.00 ± 0.23
1SFOS ($ee\mu + \mu\mu e$)	3.37 ± 0.41	10.1 ± 1.6	0.588 ± 0.082	1.36 ± 0.17	15.4 ± 2.2	1987 ± 293	0.344 ± 0.070	2134	1.07 ± 0.16	1.07 ± 0.16
num. jets < 2 ($ee\mu + \mu\mu e$)	3.03 ± 0.37	6.0 ± 1.0	0.533 ± 0.076	1.02 ± 0.13	10.6 ± 1.5	1634 ± 243	0.262 ± 0.055	1693	1.04 ± 0.16	1.03 ± 0.15
top-veto ($ee\mu + \mu\mu e$)	2.85 ± 0.35	5.07 ± 0.86	0.494 ± 0.071	0.82 ± 0.11	9.2 ± 1.4	1498 ± 222	0.238 ± 0.050	1574	1.05 ± 0.16	1.04 ± 0.16
$E_{T,STVF}^{miss}$ and $E_{T,TrackHWW}^{miss}$ cuts ($ee\mu + \mu\mu e$)	2.30 ± 0.28	3.48 ± 0.61	0.344 ± 0.052	0.540 ± 0.075	6.7 ± 1.0	639 ± 86	0.263 ± 0.053	647	1.01 ± 0.14	1.00 ± 0.14
Z mass veto ($ee\mu + \mu\mu e$)	1.80 ± 0.22	0.232 ± 0.053	0.213 ± 0.034	-	2.29 ± 0.30	70 ± 11	0.272 ± 0.058	72	1.03 ± 0.21	0.99 ± 0.20
$m_{ll,min}$ and $m_{ll,max}$ cuts ($ee\mu + \mu\mu e$)	1.58 ± 0.19	0.201 ± 0.045	0.197 ± 0.032	-	2.01 ± 0.26	50.9 ± 8.9	0.280 ± 0.061	56	1.10 ± 0.24	1.06 ± 0.23
$\Delta R_{ll} < 2.0$ ($ee\mu + \mu\mu e$)	1.49 ± 0.18	0.179 ± 0.042	0.133 ± 0.023	-	1.82 ± 0.24	35.6 ± 6.2	0.303 ± 0.066	40	1.12 ± 0.27	1.07 ± 0.25
SS-leptons OR ($ee\mu + \mu\mu e$)	1.48 ± 0.17	0.179 ± 0.041	0.133 ± 0.022	-	1.82 ± 0.22	35.5 ± 4.5	0.303 ± 0.053	40	1.13 ± 0.23	1.07 ± 0.22
$\ell\nu\ell\nu$ OR ($ee\mu + \mu\mu e$)	1.44 ± 0.17	0.179 ± 0.042	0.130 ± 0.021	-	1.77 ± 0.21	34.0 ± 4.3	0.301 ± 0.046	38	1.12 ± 0.22	1.06 ± 0.20
0SFOS ($\ell\ell\ell$)	1.66 ± 0.20	0.37 ± 0.12	0.283 ± 0.040	-	2.36 ± 0.32	47.4 ± 8.8	0.340 ± 0.078	50	1.06 ± 0.25	1.01 ± 0.23
num. jets < 2 ($\ell\ell\ell$)	1.49 ± 0.18	0.166 ± 0.042	0.254 ± 0.039	-	1.94 ± 0.25	24.8 ± 4.4	0.384 ± 0.084	26	1.05 ± 0.28	0.97 ± 0.25
top-veto ($\ell\ell\ell$)	1.40 ± 0.17	0.145 ± 0.040	0.240 ± 0.037	-	1.81 ± 0.24	15.2 ± 2.4	0.456 ± 0.093	18	1.18 ± 0.33	1.06 ± 0.30
$m_{ll,min}$ and $m_{ll,max}$ cuts ($\ell\ell\ell$)	1.32 ± 0.16	0.145 ± 0.040	0.230 ± 0.035	-	1.72 ± 0.23	13.3 ± 2.1	0.462 ± 0.096	15	1.12 ± 0.34	1.00 ± 0.30
SS-leptons OR ($\ell\ell\ell$)	1.32 ± 0.15	0.145 ± 0.039	0.230 ± 0.034	-	1.72 ± 0.21	13.1 ± 1.9	0.466 ± 0.089	15	1.15 ± 0.34	1.01 ± 0.30
$\ell\nu\ell\nu$ OR ($\ell\ell\ell$)	1.28 ± 0.15	0.145 ± 0.030	0.225 ± 0.033	-	1.68 ± 0.21	11.7 ± 1.8	0.478 ± 0.087	14	1.19 ± 0.33	1.04 ± 0.22

TABLE 4.8: 8 TeV 3ℓ analysis: number of expected events for the signal and total MC at each step of the event selection described in Tab. 4.7. The "sign." in the last column stands for significance, which is defined through the formula $\sqrt{2((s+b)\ln(1+\frac{s}{b})-s)}$, where s represents the number of signal events and b the background ones. The breakdown of background sources in presented in Tab. 4.9.

	VH (125 GeV)	$WZ/W\gamma^*$	$W\gamma$	ZZ^*	WW	VVV	Z/γ^*	$Z\gamma$	top	$ggF/VBF/ttH$	Total Bkg.
Pre-selection ($\ell\ell\ell$)	31.0 ± 4.0	2071 ± 134	0.038 ± 0.069	941 ± 147	1.03 ± 0.17	21.85 ± 0.93	308 ± 65	319 ± 57	201 ± 43	14.70 ± 0.62	3879 ± 513
3SF + 1SFOS ($\ell\ell\ell$)	28.6 ± 3.9	2066 ± 199	0.038 ± 0.069	939 ± 148	0.80 ± 0.16	17.3 ± 4.3	307 ± 65	319 ± 57	166 ± 35	13.8 ± 1.2	3832 ± 509
num. jets < 2 ($\ell\ell\ell$)	19.9 ± 2.8	1717 ± 169	0.010 ± 0.026	828 ± 131	0.68 ± 0.16	15.4 ± 3.8	260 ± 58	287 ± 51	47 ± 10	9.01 ± 0.82	3165 ± 423
top-veto ($\ell\ell\ell$)	17.1 ± 2.5	1595 ± 160	0.010 ± 0.025	771 ± 123	0.63 ± 0.15	14.2 ± 3.6	232 ± 51	270 ± 48	17.9 ± 4.3	8.10 ± 0.76	2911 ± 389
$E_{T,STVF}^{miss}$ and $E_{T,TrackHWW}^{miss}$ cuts ($\ell\ell\ell$)	11.9 ± 1.7	1124 ± 112	0.010 ± 0.025	88 ± 14	0.51 ± 0.15	12.0 ± 3.0	26.2 ± 8.4	13.4 ± 3.0	14.8 ± 3.5	1.08 ± 0.13	1280 ± 143
Z mass veto ($\ell\ell\ell$)	3.37 ± 0.45	76.1 ± 7.9	0.010 ± 0.025	14.1 ± 3.0	0.317 ± 0.080	5.9 ± 1.6	3.9 ± 2.2	6.3 ± 1.7	6.8 ± 1.7	0.241 ± 0.033	113 ± 17
$m_{ll,min}$ and $m_{ll,max}$ cuts ($\ell\ell\ell$)	2.88 ± 0.37	50.3 ± 5.2	-	11.1 ± 2.4	0.235 ± 0.072	4.0 ± 1.1	3.5 ± 2.2	5.2 ± 1.4	5.7 ± 1.4	0.222 ± 0.032	80 ± 13
$\Delta R_{ll} < 2.0$ ($\ell\ell\ell$)	2.62 ± 0.34	37.1 ± 3.8	-	7.5 ± 1.5	0.175 ± 0.061	3.02 ± 0.81	2.21 ± 0.69	3.04 ± 0.95	4.0 ± 1.0	0.177 ± 0.028	57.1 ± 8.5
SS-leptons OR ($\ell\ell\ell$)	2.62 ± 0.32	37.0 ± 2.7	-	7.5 ± 1.5	0.175 ± 0.061	3.01 ± 0.19	2.21 ± 0.69	3.04 ± 0.95	3.89 ± 0.98	0.177 ± 0.024	57.0 ± 6.7
$\ell\nu\ell\nu$ OR ($\ell\ell\ell$)	2.56 ± 0.32	36.1 ± 2.6	-	7.4 ± 1.5	0.171 ± 0.064	2.954 ± 0.092	2.08 ± 0.66	3.04 ± 0.95	3.34 ± 0.85	0.173 ± 0.018	55.3 ± 6.2
3SF ($eee + \mu\mu\mu$)	13.2 ± 1.9	1038 ± 124	0.038 ± 0.069	469 ± 74	0.28 ± 0.12	6.5 ± 2.2	135 ± 32	120 ± 22	67 ± 14	6.53 ± 0.76	1844 ± 268
num. jets < 2 ($eee + \mu\mu\mu$)	9.3 ± 1.4	863 ± 105	0.010 ± 0.026	415 ± 66	0.25 ± 0.12	5.7 ± 1.9	115 ± 28	108 ± 19	17.3 ± 3.9	4.58 ± 0.54	1530 ± 223
top-veto ($eee + \mu\mu\mu$)	7.8 ± 1.2	801 ± 99	0.010 ± 0.025	388 ± 62	0.23 ± 0.12	5.3 ± 1.8	105 ± 25	101 ± 18	6.3 ± 1.5	4.15 ± 0.50	1412 ± 206
$E_{T,STVF}^{miss}$ and $E_{T,TrackHWW}^{miss}$ cuts ($eee + \mu\mu\mu$)	5.28 ± 0.87	566 ± 70	0.010 ± 0.025	45.5 ± 7.4	0.21 ± 0.12	4.5 ± 1.5	12.6 ± 5.3	5.1 ± 1.5	5.3 ± 1.3	0.540 ± 0.077	640 ± 85
Z mass veto ($eee + \mu\mu\mu$)	1.08 ± 0.19	30.1 ± 3.9	0.010 ± 0.025	6.1 ± 1.4	0.092 ± 0.044	1.57 ± 0.54	1.5 ± 2.0	2.29 ± 0.81	1.70 ± 0.44	0.098 ± 0.017	43.5 ± 8.6
$m_{ll,min}$ and $m_{ll,max}$ cuts ($eee + \mu\mu\mu$)	0.87 ± 0.14	18.9 ± 2.4	-	4.7 ± 1.1	0.070 ± 0.042	0.97 ± 0.34	1.4 ± 2.0	1.80 ± 0.67	1.33 ± 0.36	0.091 ± 0.016	29.3 ± 6.3
$\Delta R_{ll} < 2.0$ ($eee + \mu\mu\mu$)	0.80 ± 0.13	14.7 ± 1.9	-	3.32 ± 0.78	0.070 ± 0.042	0.82 ± 0.29	0.22 ± 0.16	1.32 ± 0.53	1.02 ± 0.30	0.079 ± 0.015	21.6 ± 3.7
SS-leptons OR ($eee + \mu\mu\mu$)	0.80 ± 0.12	14.7 ± 1.1	-	3.32 ± 0.77	0.070 ± 0.042	0.811 ± 0.075	0.22 ± 0.16	1.32 ± 0.53	0.99 ± 0.30	0.079 ± 0.013	21.5 ± 2.7
$\ell\nu\ell\nu$ OR ($eee + \mu\mu\mu$)	0.79 ± 0.12	14.5 ± 1.1	-	3.32 ± 0.76	0.070 ± 0.042	0.804 ± 0.028	0.22 ± 0.16	1.32 ± 0.53	0.91 ± 0.26	0.079 ± 0.013	21.2 ± 1.6
1SFOS ($ee\mu + \mu\mu e$)	15.4 ± 2.2	1028 ± 123	-	470 ± 74	0.53 ± 0.10	10.8 ± 3.7	172 ± 37	198 ± 35	99 ± 21	7.25 ± 0.81	1987 ± 293
num. jets < 2 ($ee\mu + \mu\mu e$)	10.6 ± 1.5	853 ± 104	-	412 ± 65	0.434 ± 0.095	9.7 ± 3.3	145 ± 33	179 ± 32	30.2 ± 6.8	4.43 ± 0.52	1634 ± 243
top-veto ($ee\mu + \mu\mu e$)	9.2 ± 1.4	793 ± 97	-	383 ± 61	0.403 ± 0.093	8.9 ± 3.0	127 ± 29	168 ± 30	11.6 ± 2.8	3.95 ± 0.47	1498 ± 222
$E_{T,STVF}^{miss}$ and $E_{T,TrackHWW}^{miss}$ cuts ($ee\mu + \mu\mu e$)	6.7 ± 1.0	557 ± 68	-	42.5 ± 7.2	0.304 ± 0.077	7.6 ± 2.6	13.6 ± 5.3	8.4 ± 1.8	9.6 ± 2.3	0.543 ± 0.081	639 ± 86
Z mass veto ($ee\mu + \mu\mu e$)	2.29 ± 0.30	45.9 ± 5.7	-	8.1 ± 1.8	0.225 ± 0.066	4.3 ± 1.5	2.41 ± 0.71	4.0 ± 1.1	5.1 ± 1.3	0.143 ± 0.024	70 ± 11
$m_{ll,min}$ and $m_{ll,max}$ cuts ($ee\mu + \mu\mu e$)	2.01 ± 0.26	31.5 ± 4.0	-	6.4 ± 1.5	0.165 ± 0.057	3.0 ± 1.0	2.07 ± 0.68	3.37 ± 0.93	4.3 ± 1.1	0.131 ± 0.023	50.9 ± 8.9
$\Delta R_{ll} < 2.0$ ($ee\mu + \mu\mu e$)	1.82 ± 0.24	22.3 ± 2.8	-	4.16 ± 0.91	0.105 ± 0.045	2.20 ± 0.75	2.00 ± 0.67	1.72 ± 0.60	2.96 ± 0.74	0.098 ± 0.020	35.6 ± 6.2
SS-leptons OR ($ee\mu + \mu\mu e$)	1.82 ± 0.22	22.3 ± 1.7	-	4.16 ± 0.91	0.105 ± 0.045	2.20 ± 0.14	2.00 ± 0.67	1.72 ± 0.60	2.89 ± 0.73	0.097 ± 0.017	35.5 ± 4.5
$\ell\nu\ell\nu$ OR ($ee\mu + \mu\mu e$)	1.77 ± 0.21	21.6 ± 2.7	-	4.04 ± 0.89	0.101 ± 0.045	2.15 ± 0.14	1.87 ± 0.62	1.72 ± 0.60	2.43 ± 0.63	0.094 ± 0.016	34.0 ± 4.0
0SFOS ($\ell\ell\ell$)	2.36 ± 0.32	5.17 ± 0.47	-	1.71 ± 0.30	0.225 ± 0.071	4.51 ± 0.42	0.51 ± 0.20	0.097 ± 0.093	34.2 ± 7.4	0.921 ± 0.096	47.4 ± 8.8
num. jets < 2 ($\ell\ell\ell$)	1.94 ± 0.25	4.17 ± 0.41	-	1.30 ± 0.23	0.195 ± 0.068	4.13 ± 0.39	0.43 ± 0.17	0.097 ± 0.093	14.5 ± 3.3	0.054 ± 0.018	24.8 ± 4.4
top-veto ($\ell\ell\ell$)	1.81 ± 0.24	3.89 ± 0.40	-	1.22 ± 0.22	0.187 ± 0.074	3.90 ± 0.38	0.38 ± 0.16	0.097 ± 0.093	5.5 ± 1.3	0.034 ± 0.016	15.2 ± 2.4
$m_{ll,min}$ and $m_{ll,max}$ cuts ($\ell\ell\ell$)	1.72 ± 0.23	3.58 ± 0.37	-	1.11 ± 0.20	0.147 ± 0.062	3.00 ± 0.29	0.37 ± 0.15	0.097 ± 0.093	5.0 ± 1.2	0.032 ± 0.016	13.3 ± 2.1
SS-leptons OR ($\ell\ell\ell$)	1.72 ± 0.21	3.56 ± 0.32	-	1.11 ± 0.20	0.147 ± 0.062	3.00 ± 0.18	0.37 ± 0.15	0.097 ± 0.093	4.8 ± 1.2	0.032 ± 0.016	13.1 ± 1.9
$\ell\nu\ell\nu$ OR ($\ell\ell\ell$)	1.68 ± 0.21	3.42 ± 0.31	-	1.07 ± 0.19	0.116 ± 0.049	2.93 ± 0.18	0.37 ± 0.15	0.097 ± 0.093	3.72 ± 0.91	-	11.7 ± 1.8

TABLE 4.9: 8 TeV 3ℓ analysis: number of expected events for the different background processes at each step of the event selection described in Tab. 4.7.

4.4.1 3ℓ Multivariate analysis

A Multivariate Analysis (MVA) based on Boosted Decision Trees (BDT) [114] has been used to enhance the sensitivity in 3ℓ-3SF and 3ℓ-1SFOS SRs. The main purpose of this MVA analysis is to reject the dominant $WZ/W\gamma^*$ and ZZ^* background, but it has a considerable rejection power also for the other background sources.
A decision tree is a collection of cuts used to classify events as signal or background (Appendix A). The input events are successively split using a set of discriminant variables. At each split, the variable which gives the best separation between signal and background is found, as well as the optimal value of the cut on this variable. The tree is complete after a given number of splits. At this point the tree contains *leaves*, with each leaf having predominantly signal or background events: a given event is classified as signal or background depending on the majority classification of the training events that end up in the same final leaf node. At this point, a second tree is grown to correctly identify the signal or background events that were misidentified by the first tree. Such events are given an increased weight or *boost*, relative to correctly identified events. Then a third tree is grown and so on until there is a *forest* of $O(1000)$ trees. A weighted average is taken from all trees to form a discriminant, or *BDT Score*. The *boosting* stabilises the response of the decision trees with respect to fluctuations in the training samples and is able to considerably enhance the performance with respect to a single tree. The performance of the boosted decision trees depends on the type of boosting used. In this analysis a gradient boosted decision trees (Appendix A) has been adopted. The default values of most BDT parameters, as suggested in Ref. [114], are kept, except of the ones listed below, which have been modified to optimise the performance:

- the number of trees in the forest (NTrees = 1000);
- the minimum number of events requested in a leaf (nEventsMin = 1430);
- the use of only a random sub-sample of all events for growing the trees in each iteration (UseBaggedGrad);
- the fraction of events to be used at each iteration (GradBaggingFraction = 0.5);
- the learning rate of the BDT (Shrinkage = 0.1);
- the maximum number of layers in one tree (MaxDepth = 3).

The main changes with respect to the default values concern the BDT parameters which depend on the number of input variables and on the number of events used in the training, these BDT parameters have been tuned in order to ensure that there is no overtraining, i.e. that the BDT is robust against statistical fluctuations in the training samples. The values used for the modified BDT parameters are very similar to the ones used in Ref. [115].

4.4.1.1 Training of the Boosted Decision Trees

The MC samples used in this analysis are the ones already described in Sec. 4.2. The training of the BDT has been performed using the WH signal and the $WZ/W\gamma^*$ and ZZ^* as background. All the other background samples are used in the final classification. Following the recommendations in the *Toolkit for Multivariate Data Analysis* (TMVA) [114], the training samples are divided into even and odd samples. The training is then performed separately for even and odd events and two sets of weight files are produced. Each training consists of WH 45000 signal events and 180000 background events ($WZ/W\gamma^*$ plus ZZ^*). The weight file produced when training with even events is used to classify odd events and vice-versa. The KS test [113] in Fig. 4.11 is used to check that the BDT method is not affected by statistical fluctuations in the training samples: the results from the training and test samples are compared and the KS probability is evaluated. The high values of the KS test probability (0.74 for signal, 0.89 for background) are an indication of the robustness of the BDT training.
The input events, on which the training is performed, are the ones selected by the preselection cuts defined for the 3ℓ channel described in Sec. 4.3. They contain exactly three isolated leptons with $p_{\mathrm{T}} > 15$ GeV of total charge $\pm$ 1, one of which should be matched to the trigger. Before performing the training procedure, the following cuts are also applied to the input events:

Cut 1: Selection of 3SF and 1SFOS SRs;

Cut 2: "jet-veto", at most one jet with $p_{\mathrm{T}} > 25$ GeV;

Cut 3: "top-veto", no b-tagged jets with $p_{\mathrm{T}} > 20$ GeV;

Cut 4: $E_{\mathrm{T}}^{\mathrm{miss}} > 15$ GeV.

An optimisation study has been done in order to identify the input discriminating variables, used in the training, that give the best separation between signal and background, the following ones have been used:

- $p_{\mathrm{T}}^{\ell_0}$, $p_{\mathrm{T}}^{\ell_1}$, $p_{\mathrm{T}}^{\ell_2}$, $|\Sigma \mathbf{p}_{\mathrm{T}}{}^{\mathrm{lep}}|$,
- $m_{\ell_0\ell_1}$, $m_{\ell_0\ell_2}$, $\Delta R_{\ell_0\ell_1}$,

- $E_{\mathrm{T}}^{\mathrm{miss}}$, $p_{\mathrm{T}}^{\mathrm{miss}}$.

Fig. 4.7, Fig. 4.8 and Fig. 4.9 show the shapes of the input variables for signal and background after the training cuts. Fig. 4.10 shows the linear correlation among the input variables for both signal and background. Non-negligibe linear correlation is present among training variables, anyway the optimisation has guaranteed that alternative trainings even with less variables have worse performances.

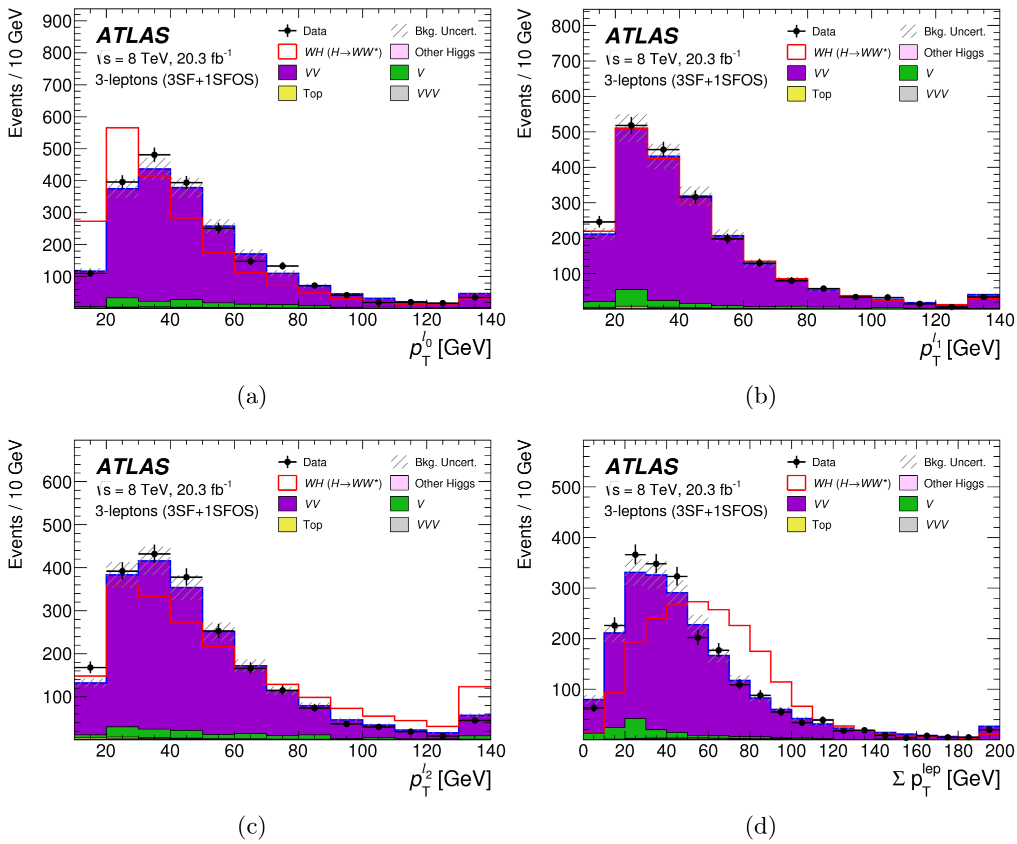

FIGURE 4.7: Shapes of the input training variables for background (stacked filled histograms) and WH signal (non-stacked unfilled histogram multiplied by a factor 500) after the training cuts 1, 2 and 3: (a) $p_{\mathrm{T}}^{\ell_0}$, (b) $p_{\mathrm{T}}^{\ell_1}$, (c) $p_{\mathrm{T}}^{\ell_2}$, (d) $|\Sigma \mathbf{p_T}^{\mathrm{lep}}|$ [71].

Tab. 4.10 shows the separation and importance for the training variable. The separation $< S^2 >$ of a variable y is defined by the integral:

$$< S^2 >= \frac{1}{2}\int \frac{(\hat{y}_S(y) - \hat{y}_B(y))^2}{(\hat{y}_S(y) + \hat{y}_B(y))} dy,$$

where $\hat{y}_S$ and $\hat{y}_B$ are the signal and background PDFs of y, respectively [114]. The importance of a variable is derived by counting how often the variable is used to split decision tree nodes, weighting each split occurrence by the separation gain-squared it has achieved and by the number of events in the node. In MVA analyses the ranking based

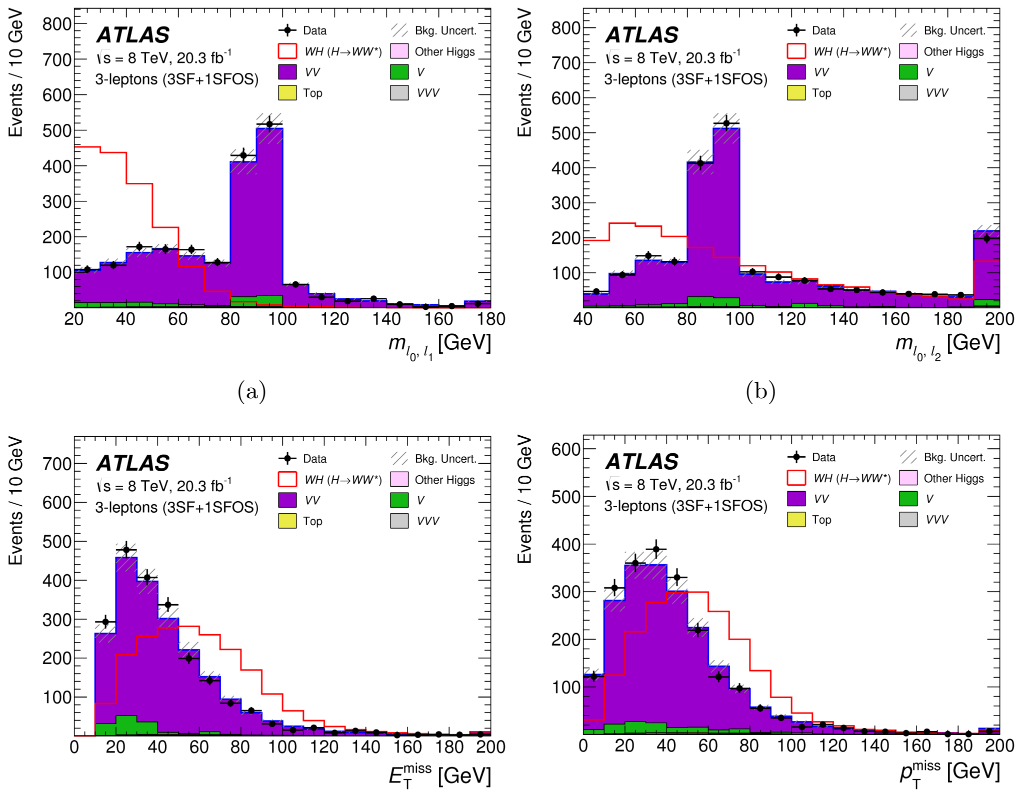

(a) (b)

(c) (d)

FIGURE 4.8: Shapes of the input training variables for background (stacked filled histograms) and WH signal (non-stacked unfilled histogram multiplied by a factor 500) after the training cuts 1, 2 and 3: (a) $m_{\ell_0\ell_1}$, (b) $m_{\ell_0\ell_2}$, (c) $E_{\mathrm{T}}^{\mathrm{miss}}$, (d) $p_{\mathrm{T}}^{\mathrm{miss}}$ [71].

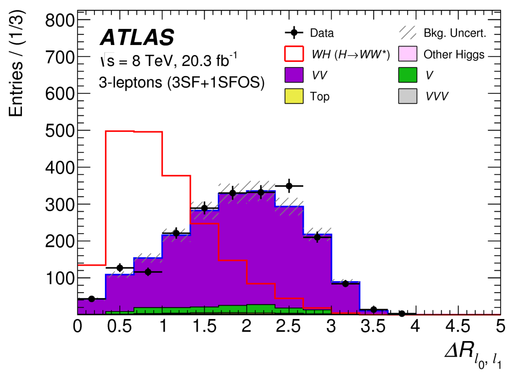

(a)

FIGURE 4.9: Shapes of the input training variables for background (stacked filled histograms) and WH signal (non-stacked unfilled histogram multiplied by a factor 500) after the training cuts 1, 2 and 3: $\Delta R_{\ell_0\ell_1}$ [71].

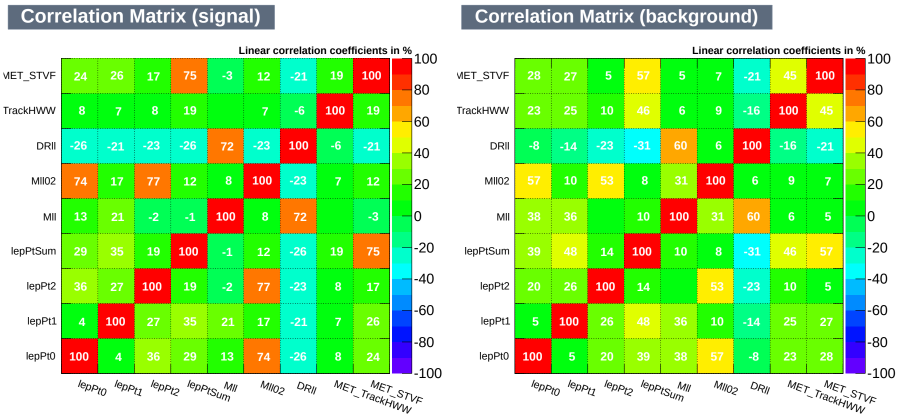

(a) (b)

FIGURE 4.10: Linear correlation among the input variables for (a) the signal and (b) the $WZ/W\gamma^*$ plus ZZ^* background. In this table $p_{\mathrm{T}}^{\mathrm{miss}}$ and $E_{\mathrm{T}}^{\mathrm{miss}}$ are referred with MET_TrackHWW and MET_STVF respectively.

on the importance can be slightly different by the ranking based on the separation, what matters is that on average the variables with the higher importance have also higher separation and this is what is happening in our case, as shown in Tab. 4.10.

Variable	Separation (%)	Importance (%)
$m_{\ell_0\ell_1}$	42.9	19.1
$\Delta R_{\ell_0\ell_1}$	29.9	14.1
$m_{\ell_0\ell_2}$	16.4	17.5
$E_{\mathrm{T}}^{\mathrm{miss}}$	6.81	9.3
$p_{\mathrm{T}}^{\ell_0}$	4.7	7.6
$p_{\mathrm{T}}^{\mathrm{miss}}$	4.3	6.0
$\lvert\Sigma \mathbf{p}_{\mathrm{T}}{}^{\mathrm{lep}}\rvert$	3.5	10.0
$p_{\mathrm{T}}^{\ell_2}$	1.9	8.1
$p_{\mathrm{T}}^{\ell_1}$	0.4	8.4

TABLE 4.10: Separation and importance for 3ℓ MVA training variables.

4.4.1.2 Classification of data and MC samples

The training produces two sets of weight files which are used, in the final classification, to assign a BDT Score to data and MC events: the weight file produced when training with even events is used to classify odd events and vice-versa. The best sensitivity is obtained performing a fit to the shape of the BDT Score distribution for 3SF+1SFOS as described in Sec. 5.2 instead of adopting a simple cut.

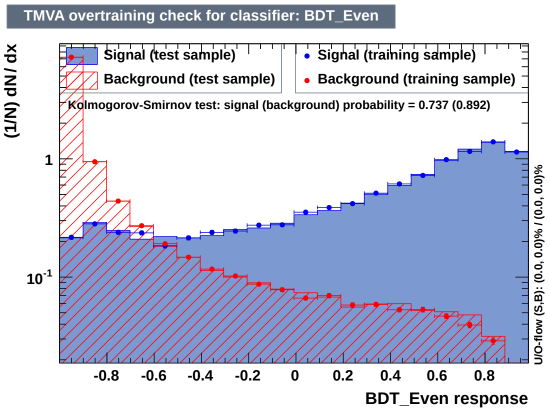

FIGURE 4.11: Result of the Kolmogorov-Smirnov test to check the compatibility of the training and testing samples for the signal and the background.

Fig. 4.12 shows the BDT Score distribution for the signal and for all the backgrounds, after the selection performed by the seven cuts listed above.

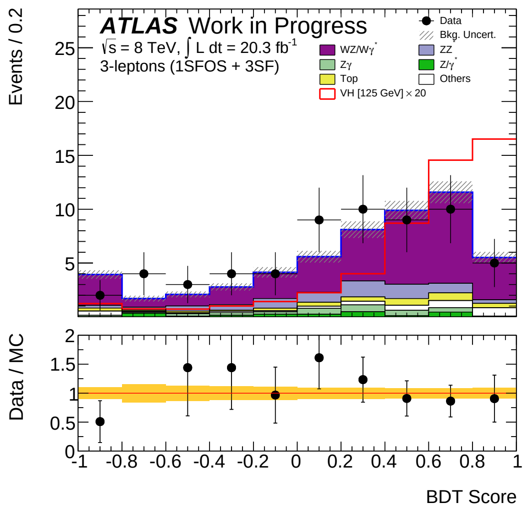

FIGURE 4.12: Distribution of BDT Score for background (stacked filled histograms) and VH signal (non-stacked unfilled histogram multiplied by a factor 20).

4.5 Control samples

Control Regions, defined in a phase space disjoint but close to the signal phase space, are used to normalise the prediction of some of the backgrounds to the yield estimated using data. Given the requirement of selecting a phase space close to the SRs, different CRs can be defined for the same background to normalise the predictions for different SRs. Selections are defined granting the orthogonality between the CRs used for the background normalisation in a given analysis. The normalisation of the backgrounds in the SRs are extracted from the final fit, described in Sec. 5.2, where both SRs and CRs are used taking into account properly all the correlations. A simultaneous likelihood fit to the relevant SRs and CRs is performed; the inputs to the fit are the numbers of observed events in the SRs and CRs and the expected contributions of each process contributing to the CRs. The free parameters in the fit are the NFs of the most relevant backgrounds as well as the signal strength. The other free parameters are the systematic uncertainties on the expected background yield that are included as nuisance parameters with gaussian constraint in the fit. The correlations between different regions are taken into account with common nuisance parameters in the fitting procedure. The list of backgrounds normalised in such a way depends on the SRs and is described in the following Sections.

The 3ℓ analysis is further described in Sec. 4.5.1, details of the $2\ell/4\ell$ analyses can be found in Ref. [71].

4.5.1 3ℓ analysis

In the 3ℓ analysis normalisation factors are defined for each of the following backgrounds:

- $WZ/W\gamma^*$, the dominant background in 3SF+1SFOS;
- ZZ^*, the second background in 3SF+1SFOS;
- t-quark processes;
- Z+jets (e-fake, μ-fake);
- $Z\gamma$.

It is not always possible to define selections providing pure CRs for the above listed backgrounds, for instance the Z+jets component cannot be easily disentangled from $WZ/W\gamma^*$, ZZ^* and $Z\gamma$. Tab. 4.11 lists for all the CRs defined for the 3ℓ analysis the differences in selections with respect to the SR, the target background(s) and the

SR to which the NFs, extracted from the final fit to CRs and SRs, are applied. The CRs are defined within 3SF and 1SFOS topologies, and the normalisation factors are applied also to 0SFOS. This choice is dictated by the larger number of events available in 3SF and 1SFOS. Tab. 5.1 shows the normalisation factors extracted from the final fit to CRs and SRs analysis while Tab. 4.12 shows the background composition in the defined CRs after applying the NFs. 3ℓ-WZ-CR and 3ℓ-ZZ-CR have the highest purity for $WZ/W\gamma^*$ and ZZ^* respectively. Since the features of the Z+jets background are expected to be different when the additional fake lepton is an electron or a muon, two distinct CRs and normalisation factors have been introduced for 3ℓ-Zjets-CR. They apply separately to events with the flavour combinations $\mu\mu e + eee$ (3ℓ-Zjets-CR-e-fake) and $\mu\mu\mu + ee\mu$ (3ℓ-Zjets-CR-μ-fake). 3ℓ-Top-CR is designed for t-quark processes but presents a non-negligible contribution of other backgrounds with jets. 3ℓ-$Z\gamma$-CR is designed for processes with a on-shell Z boson and a photon, in approximately half of the CR an off-shell Z boson is present instead of the photon anyway $Z\gamma$ and ZZ^* are treated as separate processes, i.e. a NF for the former and another one for the latter, no constraints are assumed on their relation in the fit procedure. As explained in Sec. 5.2, a simultaneous fit is performed to both CRs and SRs, it takes into account all the contributions included the small signal “contamination” in the CRs.

Data and MC distributions are presented from Fig. 4.13 to Fig. 4.17. Fig. 4.18 shows in each CR the distribution of the BDT Score defined in Sec. 4.4.1.

Name	Main background	Reference SR	Changes w.r.t. SR	to be applied to SR
3ℓ-WZ-CR	$WZ/W\gamma^*$	3SF, 1SFOS	≥ 1 SFOS pair with $\lvert m_{\ell\ell} - m_Z \rvert < 25$ GeV	3SF, 1SFOS, 0SFOS
3ℓ-ZZ-CR	ZZ^*	3SF, 1SFOS only $\mu\mu\mu, ee\mu$	no Z-mass veto $\lvert m_{\ell\ell\ell} - m_Z \rvert < 15$ GeV ($E_{\mathrm{T}}^{\mathrm{miss}} < 30$ GeVor $p_{\mathrm{T}}^{\mathrm{miss}} < 20$ GeV) veto eee and $\mu\mu e$ channels	3SF, 1SFOS, 0SFOS
3ℓ-Zjets-CR (μ/e)-fake	Z+jets $WZ/W\gamma^*$, ZZ^*, $Z\gamma$	3SF, 1SFOS	≥ 1 SFOS pair with $\lvert m_{\ell\ell} - m_Z \rvert < 25$ GeV ($E_{\mathrm{T}}^{\mathrm{miss}} < 30$ GeVand $p_{\mathrm{T}}^{\mathrm{miss}} < 20$ GeV) $\lvert m_{\ell\ell\ell} - m_Z \rvert > 15$ GeV	3SF, 1SFOS, 0SFOS
3ℓ-Top-CR	Top	3SF, 1SFOS	no $m_{\ell\ell}^{max}$ and $\Delta R_{\ell_0\ell_1}$ cuts at least 1 jet, at least 1 b-tagged jet	3SF, 1SFOS, 0SFOS
3ℓ-$Z\gamma$-CR	$Z\gamma$, ZZ^*	3SF, 1SFOS only $eee, \mu\mu e$	no Z-mass veto $\lvert m_{\ell\ell\ell} - m_Z \rvert < 15$ GeV ($E_{\mathrm{T}}^{\mathrm{miss}} < 30$ GeVor $p_{\mathrm{T}}^{\mathrm{miss}} < 20$ GeV) veto $\mu\mu\mu$ and $ee\mu$ channels	3SF, 1SFOS, 0SFOS

TABLE 4.11: 3ℓ analysis: summary of the control regions.

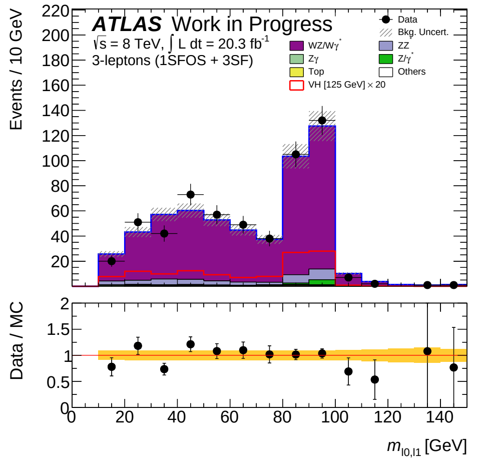

(a)

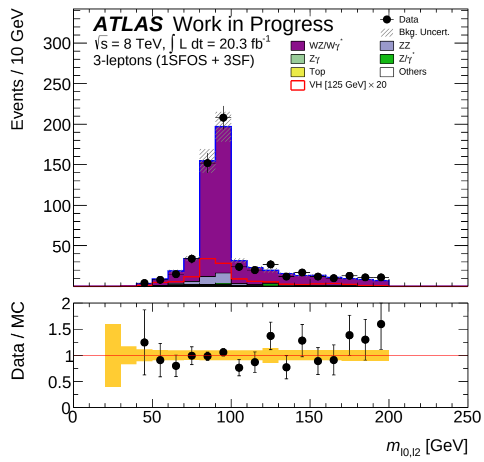

(b)

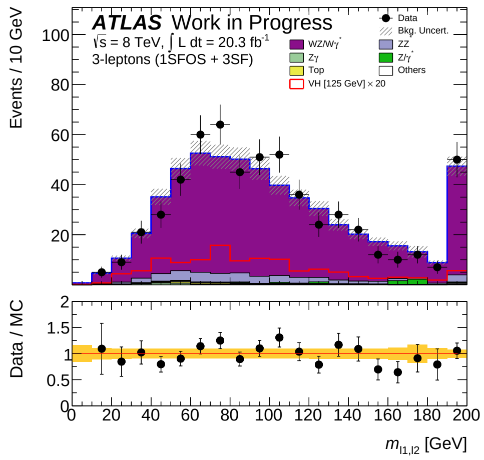

(c)

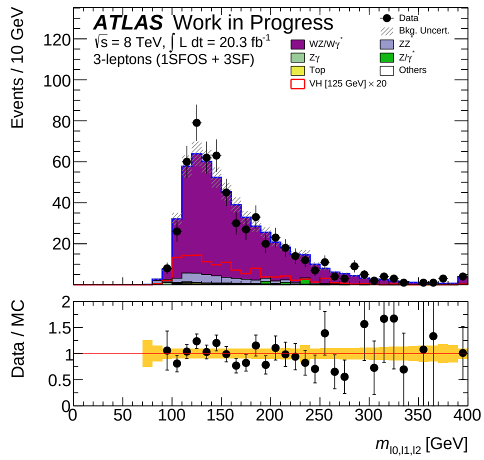

(d)

FIGURE 4.13: Distributions of different invariant mass combinations in the 3ℓ control region 3ℓ-WZ-CR: (a) invariant mass of opposite-sign lepton pair with smaller ΔR, (b) invariant mass of opposite-sign lepton pair with larger ΔR, (c) invariant mass of same-sign lepton pair, and (d) tri-lepton invariant mass. Data (dots) are compared to background expectation from the simulation of the background components, normalised using the NFs from the final fit (stacked filled histograms). Expectations for SM Higgs boson associated production with $m_H = 125$ GeV are multiplied by a factor 20 and presented as a non-stacked unfilled histogram.

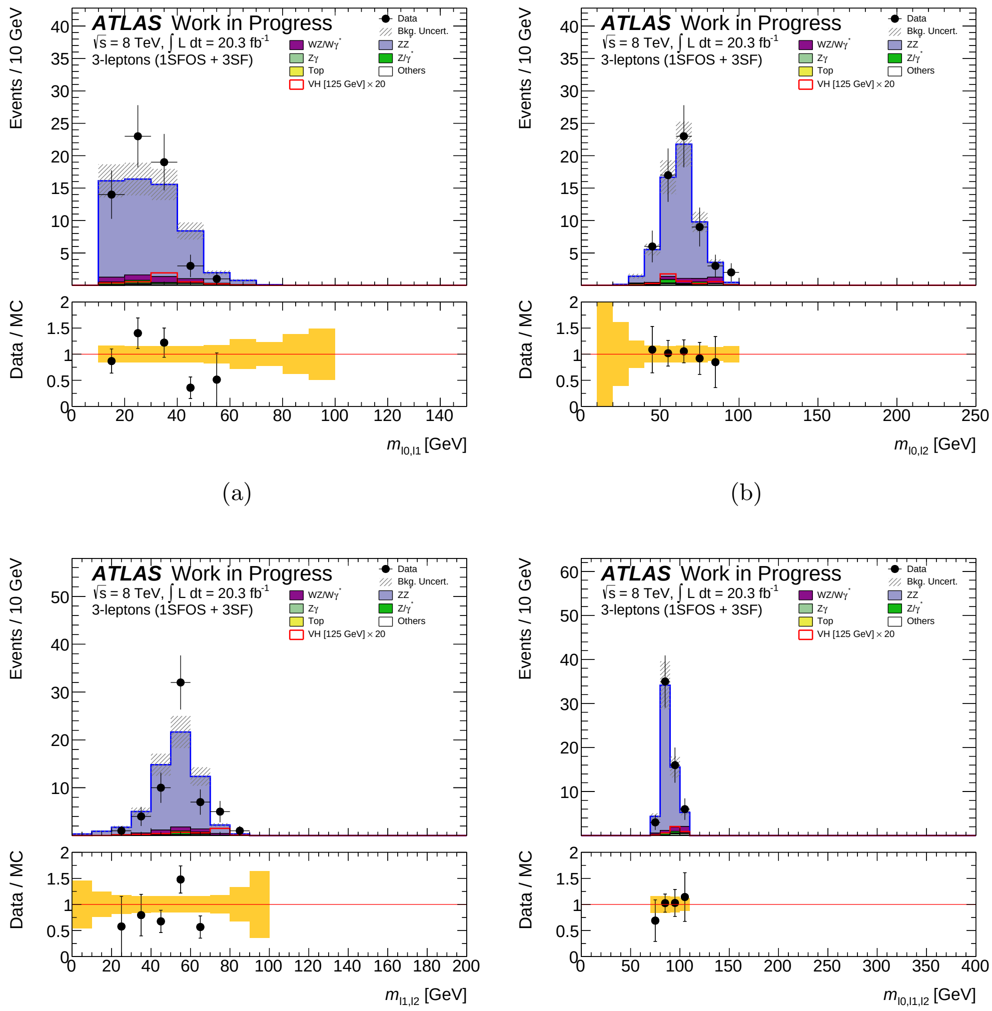

(a) (b)

(c) (d)

FIGURE 4.14: Distributions of different invariant mass combinations in the 3ℓ control region 3ℓ-ZZ-CR: (a) invariant mass of opposite-sign lepton pair with smaller ΔR, (b) invariant mass of opposite-sign lepton pair with larger ΔR (c) invariant mass of same-sign lepton pair, and (d) tri-lepton invariant mass. Data (dots) are compared to background expectation from the simulation of the background components, normalised using the NFs from the final fit (stacked filled histograms). Expectations for SM Higgs boson associated production with $m_H = 125$ GeV are multiplied by a factor 20 and presented as a non-stacked unfilled histogram.

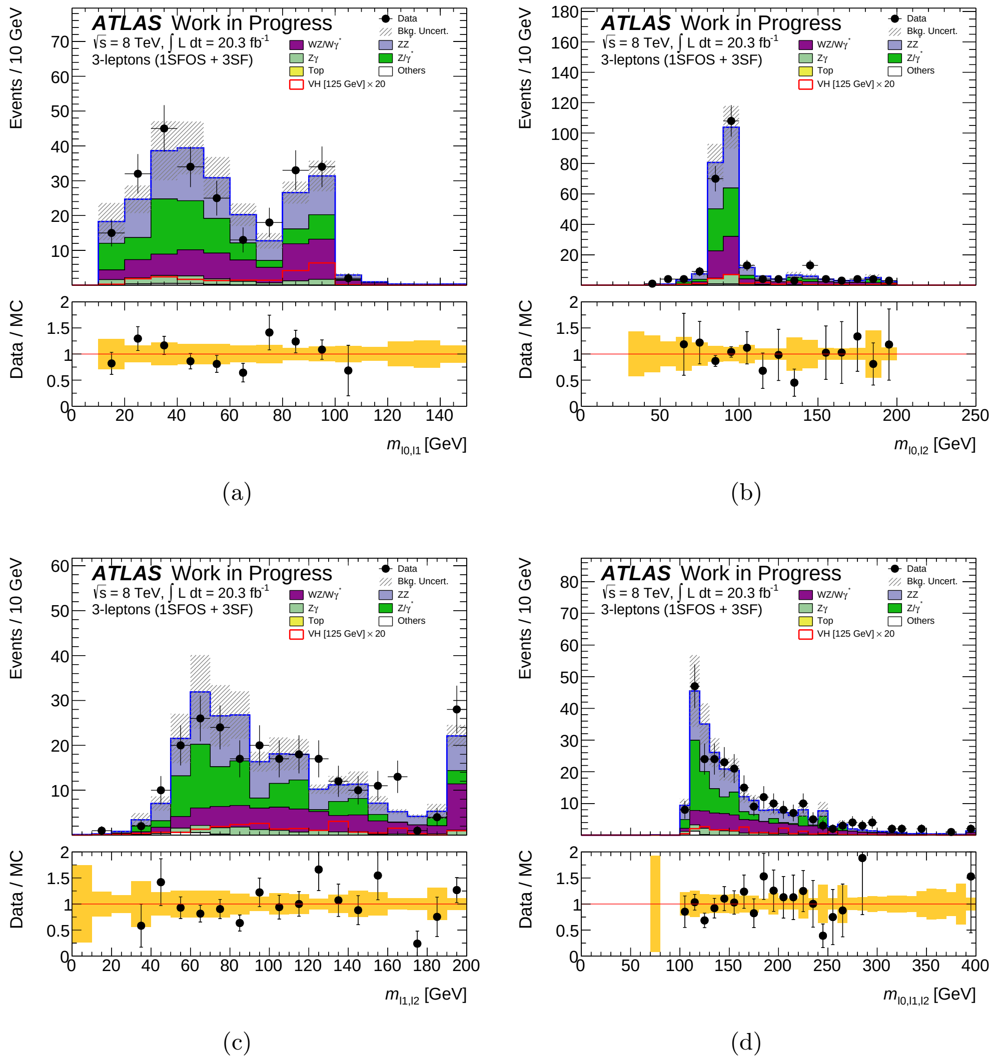

FIGURE 4.15: Distributions of different invariant mass combinations in the 3ℓ control region 3ℓ-Zjets-CR: (a) invariant mass of opposite-sign lepton pair with smaller ΔR, (b) invariant mass of opposite-sign lepton pair with larger ΔR, (c) invariant mass of same-sign lepton pair, and (d) tri-lepton invariant mass. Data (dots) are compared to background expectation from the simulation of the background components, normalised using the NFs from the final fit (stacked filled histograms). Expectations for SM Higgs boson associated production with $m_H = 125$ GeV are multiplied by a factor 20 and presented as a non-stacked unfilled histogram.

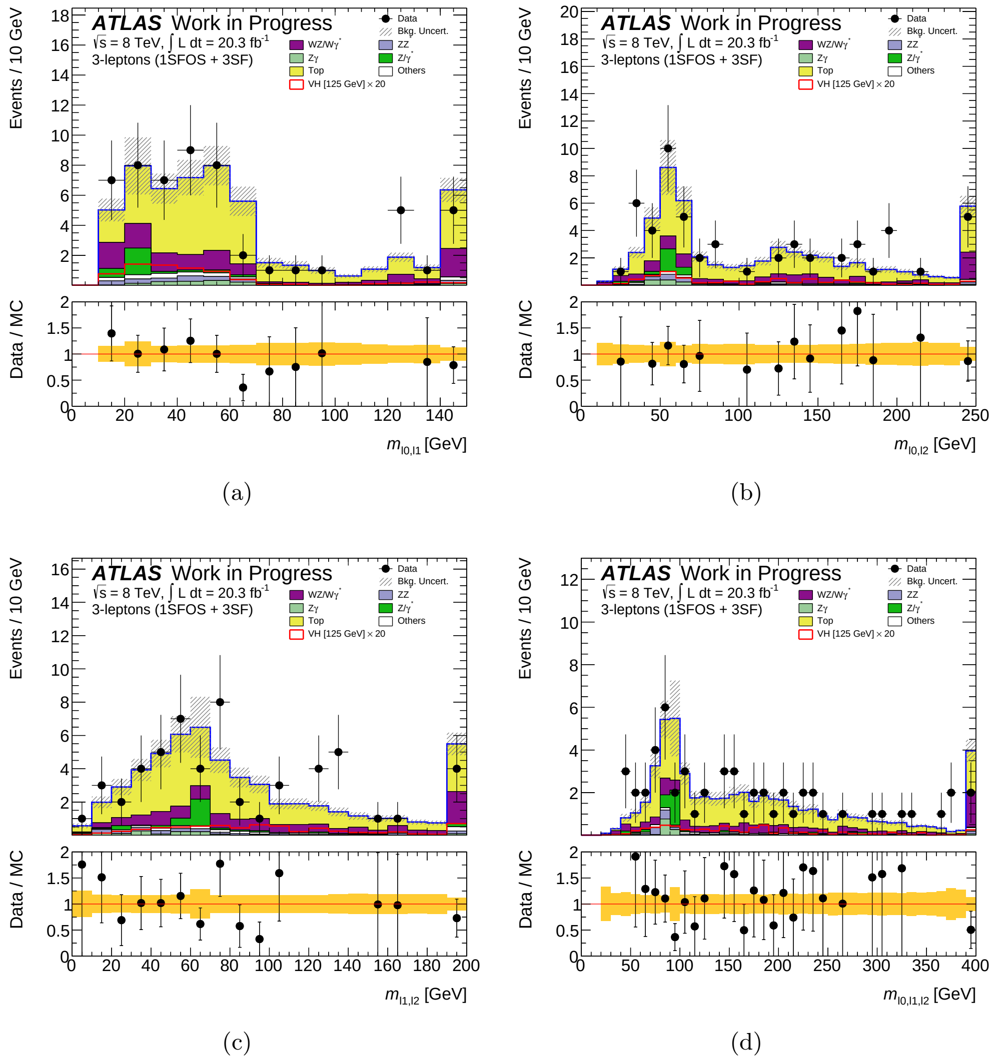

FIGURE 4.16: Distributions of different invariant mass combinations in the 3ℓ control region 3ℓ-Top-CR: (a) invariant mass of opposite-sign lepton pair with smaller ΔR, (b) invariant mass of opposite-sign lepton pair with larger ΔR, (c) invariant mass of same-sign lepton pair, and (d) tri-lepton invariant mass. Data (dots) are compared to background expectation from the simulation of the background components, normalised using the NFs from the final fit (stacked filled histograms). Expectations for SM Higgs boson associated production with $m_H = 125$ GeV are multiplied by a factor 20 and presented as a non-stacked unfilled histogram.

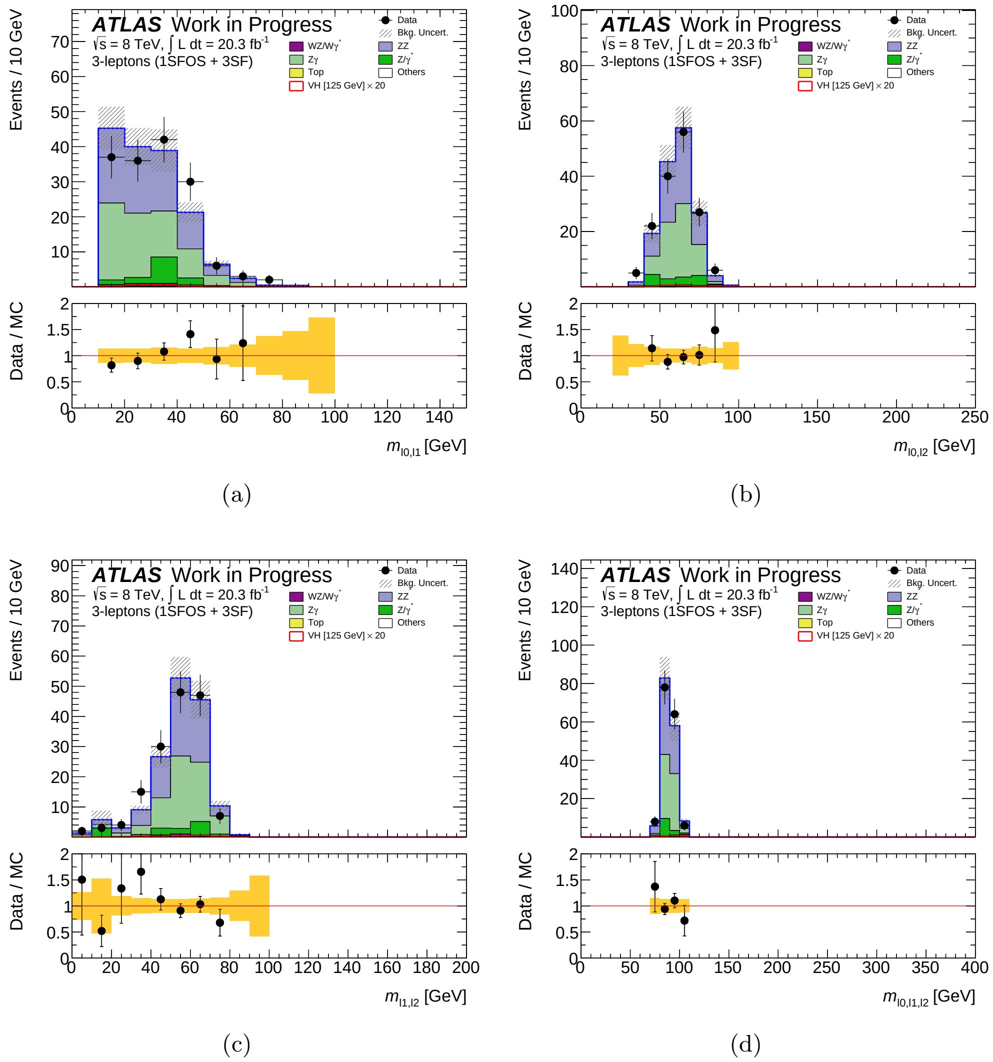

FIGURE 4.17: Distributions of different invariant mass combinations in the 3ℓ control region 3ℓ-$Z\gamma$-CR: (a) invariant mass of opposite-sign lepton pair with smaller ΔR, (b) invariant mass of opposite-sign lepton pair with larger ΔR, (c) invariant mass of same-sign lepton pair, and (d) tri-lepton invariant mass. Data (dots) are compared to background expectation from the simulation of the background components, normalised using the NFs from the final fit (stacked filled histograms). Expectations for SM Higgs boson associated production with $m_H = 125$ GeV are multiplied by a factor 20 and presented as a non-stacked unfilled histogram.

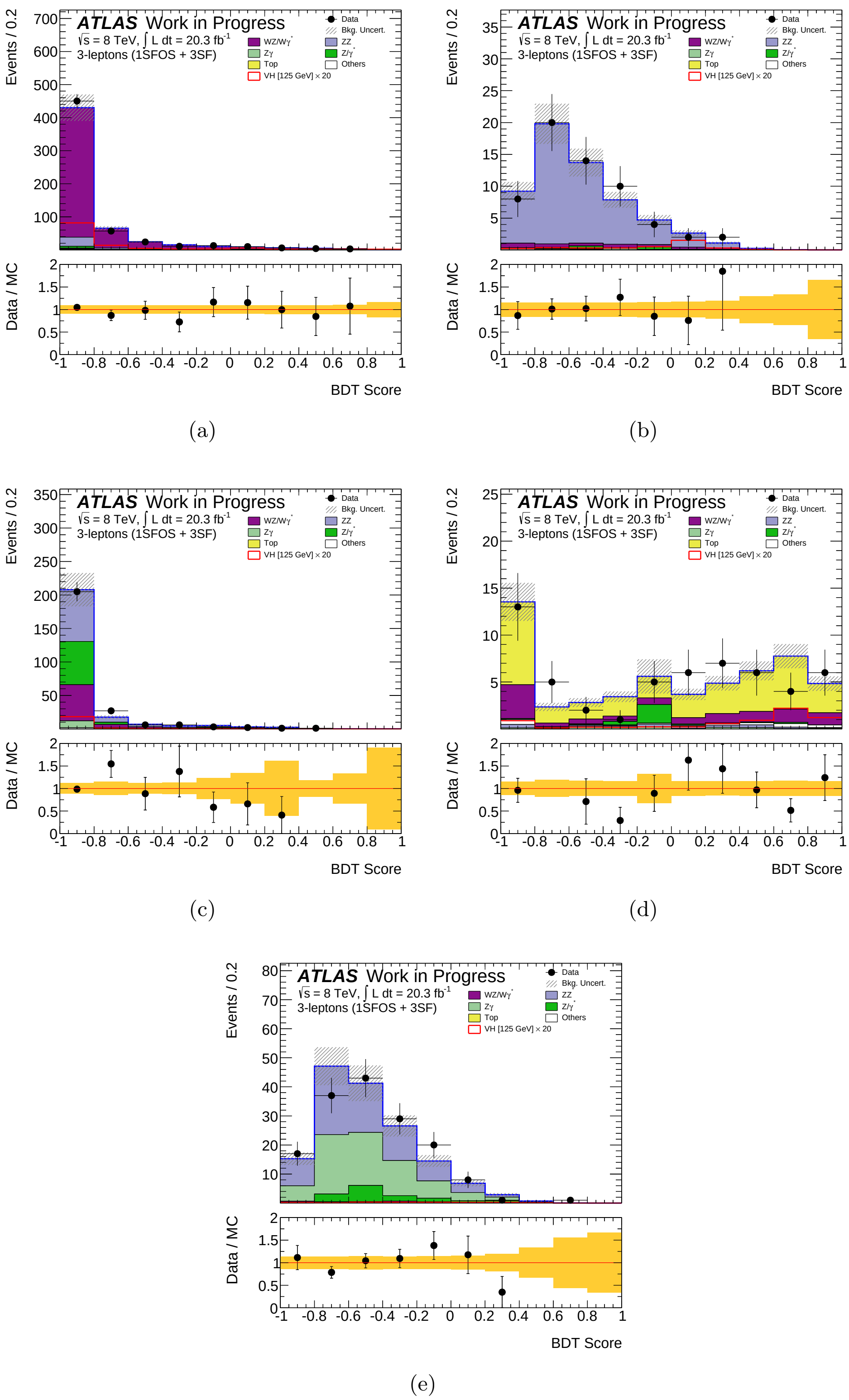

FIGURE 4.18: Distributions of BDT Score in the 3ℓ control regions: (a) 3ℓ-WZ-CR, (b) 3ℓ-ZZ-CR, (c) 3ℓ-Zjets-CR, (d) 3ℓ-Top-CR, (e) 3ℓ-$Z\gamma$-CR. Data (dots) are compared to background expectation from the simulation of the background components, normalised using the NFs from the final fit (stacked filled histograms). Expectations for SM Higgs boson associated production with $m_H = 125$ GeV are multiplied by a factor 20 and presented as a non-stacked unfilled histogram.

	Obs.	Total Bkg.	Data/MC	VH (125 GeV)	Total Bkg. + Sig	Data/(MC+Sig)	$WZ/W\gamma^*$	$W\gamma$	ZZ^*	WW	VVV	Z/γ^*	$Z\gamma$	top	$ggF/VBF/ttH$
WZ CR ($\ell\ell\ell$)	578	569 ± 62	1.02 ± 0.12	6.12 ± 0.63	575 ± 63	1.00 ± 0.12	513 ± 51	-	38.7 ± 6.3	0.052 ± 0.041	3.33 ± 0.82	6.2 ± 3.0	3.12 ± 0.95	3.77 ± 0.96	0.500 ± 0.078
ZZ CR ($\ell\ell\ell$)	60	59 ± 10	1.01 ± 0.22	0.180 ± 0.061	59 ± 10	1.01 ± 0.22	3.28 ± 0.41	-	53.6 ± 8.8	-	0.044 ± 0.023	1.26 ± 0.86	0.35 ± 0.31	0.160 ± 0.087	0.620 ± 0.061
$Z\gamma$ CR ($\ell\ell\ell$)	156	155 ± 31	1.01 ± 0.22	0.100 ± 0.011	155 ± 31	1.01 ± 0.22	2.60 ± 0.37	-	72 ± 12	-	0.054 ± 0.021	12.8 ± 5.5	66 ± 14	0.21 ± 0.10	0.450 ± 0.064
Z+jets CR ($\ell\ell\ell$)	251	247 ± 45	1.01 ± 0.20	1.06 ± 0.18	248 ± 45	1.01 ± 0.20	64.4 ± 6.7	-	94 ± 15	0.021 ± 0.032	0.170 ± 0.054	72 ± 22	13.6 ± 3.5	0.200 ± 0.088	1.83 ± 0.20
Z+jets CR (μ-fake)	103	101 ± 24	1.02 ± 0.27	0.69 ± 0.15	102 ± 24	1.01 ± 0.27	35.0 ± 3.7	-	39.3 ± 6.4	-	0.091 ± 0.032	25 ± 16	-	0.110 ± 0.054	1.07 ± 0.12
Z+jets CR (e-fake)	148	146 ± 29	1.01 ± 0.22	0.370 ± 0.082	146 ± 29	1.01 ± 0.22	29.4 ± 3.1	-	55.7 ± 9.4	0.021 ± 0.034	0.081 ± 0.032	46 ± 14	13.6 ± 3.5	0.100 ± 0.057	0.770 ± 0.097
Top CR ($\ell\ell\ell$)	55	55 ± 11	1.00 ± 0.25	0.340 ± 0.062	55 ± 11	0.99 ± 0.25	11.2 ± 1.7	-	2.01 ± 0.61	0.051 ± 0.031	0.47 ± 0.14	3.0 ± 1.9	1.30 ± 0.45	35.4 ± 7.7	1.50 ± 0.14

TABLE 4.12: 8 TeV 3ℓ analysis: number of expected and observed events in the control regions defined in Tab. 4.11. The expectations are normalised using the NFs from the final fit.

4.6 Analysis of the 7 TeV data sample

4ℓ, 3ℓ and 2ℓ-DFOS analyses have been performed on the 7 TeV data sample as well. In this Section the differences between the 8 TeV and 7 TeV analyses are highlighted and the results of the latter are presented.

4.6.1 Data and Monte Carlo samples

The data used for this analysis were collected in 2011 and amount to 4.5 fb^{-1}. The data were collected using inclusive single muon and single electron triggers with different thresholds with respect to 8 TeV data analyses. The two main triggers require the transverse momentum of the lepton with respect to the beam line, p_{T}, to exceed 18 GeV in case of the muon and between 20 and 22 GeV for the electron. An auxiliary trigger for high p_{T} muons (p_{T} >40 GeV) using only muon spectrometer reconstruction is also used to recover efficiency. The processes considered as part of the signal or of the backgrounds are listed in Tab. 4.13 together with the generator adopted to model them and the cross-section assumed in the default normalisation.

Process	Generator	Cross section ($\sqrt{s}=7$ TeV [pb])	Notes
WH/ZH	Pythia v6.425	0.20 (m_H=125 GeV)	$H \to WW^*$
ggF	Powheg-Box v1.0 + Pythia v6.425	0.34 (m_H=125 GeV)	$H \to WW^* \to \ell\nu\ell\nu$
VBF	Powheg-Box v1.0 + Pythia v6.425	0.027 (m_H=125 GeV)	$H \to WW^* \to \ell\nu\ell\nu$
inclusive W	Alpgen v2.14 + Herwig v6.520	26000 × ($k=1.20$)	$W \to \ell\nu$
inclusive W+HF	Alpgen v2.14 + Herwig v6.520	1300 × ($k=1.20$)	Wc, Wcc, Wbb
inclusive Z/γ^* high mass	Alpgen v2.14 + Herwig v6.520	2600 × ($k=1.25$)	$Z \to \ell\ell$
inclusive Z/γ^* low mass	Alpgen v2.14 + Herwig v6.520	9600 × ($k=1.22$)	$Z \to \ell\ell$
inclusive Z/γ^*+bb	Alpgen v2.14 + Herwig v6.520	30 × ($k=1.25$)	with $Z \to \ell\ell$
inclusive Z/γ^*+cc	Alpgen v2.14 + Herwig v6.520	20	with $Z \to ee, \mu\mu$
inclusive $Z\gamma$	Sherpa v1.4.3	82	$Z \to \ell\ell$
Z/γ^*+2 jets (EWcoupling)	Sherpa v1.3.1	2.8	$Z \to \ell\ell$
$t\bar{t}$	MC@NLO v4.0.1 + Herwig v6.520	177.3	
tqb	AcerMC v3.8+Pythia v6.425	20.9	$W \to \ell\nu$
tb	Powheg-Box v1.0 + Pythia v6.425	1.5	$W \to \ell\nu$
tW	Powheg-Box v1.0 + Pythia v6.425	1.65	both $W \to \ell\nu$
tZ	MadGraph5 v1.3.27 +Pythia v6.425	0.24	
$t\bar{t}W/Z$	MadGraph5 v1.3.27 +Pythia v6.425	0.25	0 and 1 jet
$q\bar{q}/g \to WW$	Powheg-Box v1.0 + Pythia v6.425	4.68	both $W \to \ell\nu$
$gg \to WW$	gg2WW v2.4.0 + Herwig v6.520	0.12	both $W \to \ell\nu$
$WW+2$ jets (6EWcoupling)	Sherpa v1.4.0	0.027	both $W \to \ell\nu$
$WW+2$ jets (6EWcoupling, like-sign)	Sherpa v1.4.0	0.023	
WW (4EWcoupling, like-sign)	Sherpa v1.4.0	0.016	
$WZ/W\gamma^*(m_{(Z/\gamma^*)}>7)$ GeV	Powheg-Box v1.0+Pythia v6.425	10.7	$\ell\nu(\ell\ell)$
$WZ/W\gamma^*(m_{(Z/\gamma^*)}<7)$ GeV	MadGraph v1.3.27 + Pythia v6.425	6.3 × ($k=2.01$)	$\ell\nu(\ell\ell)$
$WZ+2$ jets (6EWcoupling)	Sherpa v1.4.0	0.0085	$\ell\ell\ell\nu$ final states
$W\gamma$	Alpgen v2.14+Herwig v6.520	272 × ($k=1.15$)	
$q\bar{q}/g \to Z^{(*)}Z^{(*)} \to 4l$	Powheg-Box v1.0+Pythia v6.425	0.79	$\ell\ell\ell\ell$ and $\ell\ell\nu\nu$
$q\bar{q}/g \to Z^{(*)}Z^{(*)} \to 4l$ low mass	Sherpa v1.4.3	6.7 × ($k=0.88$)	both $Z \to \ell\ell$
$ZZ+2$ jets (6EWcoupling)	Sherpa v1.4.0	0.0014	$\ell\ell\ell\ell$ and $\ell\ell\nu\nu$
WWW^*, ZWW^*, ZZZ^*	MadGraph5 v1.5.12 + Pythia v6.427	0.0045 × ($k=1.5$)	to $3/4\ell$ final states

Table 4.13: MC generators used to model the signal and background processes. The generator used for the simulation of each process and the one for the parton showering of the events are reported, the nominal cross section used as reference and the noted regarding additional filters.

4.6.2 Object identification and event selection

The differences of the 7 TeV with respect to 8 TeV selection are:

- The electron isolation is based on the energy associated to calorimeter cells instead of topological clusters;
- the p_{T} threshold in track isolation calculation is 900 MeV instead of 400 MeV;
- the GSF algorithm is not used in electron trackings;
- the electron p_{T} cuts and identification have been re-optimised as summarised in Tab. 4.14;
- the lepton isolation criteria in 2ℓ-DFOS analysis have been re-optimised as reported in Ref. [71];
- the electron impact parameter ($z_0 \times \sin\theta$) is required to be less than 1.0 mm and d_0/σ_d is required to be smaller than 10;
- the JVF cut for jets $p_{\mathrm{T}} < 50$ GeV is 75% instead of 50%;

Category	p_{T} threshold	electron ID
3ℓ	p_{T}>15 GeV(with trigger match)	Medium++
2ℓ-DFOS	p_{T}>22, 15 GeV	Tight++
4ℓ	p_{T}>25, 20, 15, 10 GeV	Medium++

TABLE 4.14: Summary of the additional lepton identification criteria in the different categories.

The 3ℓ analysis is further described in Sec. 4.6.3, details of the $2\ell/4\ell$ analyses can be found in Ref. [71].

4.6.3 3ℓ analysis

Tab. 4.15 and Tab. 4.16 summarise the effect of the different cuts on Monte Carlo samples.

	$W(H\to WW)$	$Z(H\to WW)$	$W(H\to\tau\tau)$	$Z(H\to\tau\tau)$	VH (125 GeV)	Total Bkg.	sign.	Obs.	Data/MC	Data/(MC+Sig)
Pre-selection ($\ell\ell\ell$)	1.30 ± 0.14	1.39 ± 0.17	0.279 ± 0.033	0.558 ± 0.062	3.52 ± 0.40	1183 ± 215	0.102 ± 0.021	1159	0.98 ± 0.17	0.98 ± 0.17
3SF + 1SFOS ($\ell\ell\ell$)	0.98 ± 0.11	1.35 ± 0.18	0.209 ± 0.027	0.547 ± 0.067	3.08 ± 0.38	1175 ± 212	0.090 ± 0.020	1152	0.98 ± 0.18	0.98 ± 0.18
num. jets < 2 ($\ell\ell\ell$)	0.91 ± 0.11	1.01 ± 0.14	0.193 ± 0.025	0.439 ± 0.055	2.56 ± 0.32	1055 ± 186	0.079 ± 0.017	1011	0.96 ± 0.17	0.96 ± 0.17
top-veto ($\ell\ell\ell$)	0.88 ± 0.10	0.92 ± 0.13	0.190 ± 0.025	0.371 ± 0.047	2.37 ± 0.30	1011 ± 178	0.074 ± 0.016	973	0.96 ± 0.17	0.96 ± 0.17
E_T^{miss} and $E_{T,TrackHWW}^{miss}$ cuts ($\ell\ell\ell$)	0.702 ± 0.082	0.627 ± 0.086	0.129 ± 0.018	0.242 ± 0.031	1.70 ± 0.21	235 ± 37	0.111 ± 0.023	247	1.05 ± 0.18	1.04 ± 0.18
Z mass veto ($\ell\ell\ell$)	0.509 ± 0.060	-	0.071 ± 0.011	-	0.661 ± 0.080	24.9 ± 5.4	0.132 ± 0.033	28	1.12 ± 0.32	1.10 ± 0.31
$m_{ll,min}$ and $m_{ll,max}$ cuts ($\ell\ell\ell$)	0.441 ± 0.052	-	0.063 ± 0.010	-	0.575 ± 0.070	18.1 ± 4.2	0.134 ± 0.035	22	1.22 ± 0.39	1.18 ± 0.37
$\Delta R_{ll} < 2.0$ ($\ell\ell\ell$)	0.416 ± 0.049	-	-	-	0.521 ± 0.063	12.1 ± 2.7	0.149 ± 0.038	12	1.00 ± 0.36	0.95 ± 0.34
SS-leptons OR ($\ell\ell\ell$)	0.415 ± 0.044	-	-	-	0.519 ± 0.057	12.0 ± 2.4	0.149 ± 0.034	12	1.00 ± 0.35	0.96 ± 0.34
$\ell\nu\ell\nu$ OR ($\ell\ell\ell$)	0.408 ± 0.048	-	-	-	0.511 ± 0.062	11.6 ± 2.6	0.149 ± 0.037	11	0.94 ± 0.35	0.90 ± 0.34
3SF ($eee+\mu\mu\mu$)	0.332 ± 0.038	0.660 ± 0.089	0.064 ± 0.010	0.270 ± 0.035	1.33 ± 0.17	509 ± 97	0.059 ± 0.013	510	1.00 ± 0.20	1.00 ± 0.20
num. jets < 2 ($eee+\mu\mu\mu$)	0.311 ± 0.036	0.493 ± 0.068	-	0.211 ± 0.028	1.07 ± 0.14	455 ± 85	0.050 ± 0.011	442	0.97 ± 0.19	0.97 ± 0.19
top-veto ($eee+\mu\mu\mu$)	0.301 ± 0.035	0.449 ± 0.063	-	0.171 ± 0.023	0.98 ± 0.12	436 ± 81	0.047 ± 0.011	426	0.98 ± 0.19	0.97 ± 0.19
E_T^{miss} and $E_{T,TrackHWW}^{miss}$ cuts ($eee+\mu\mu\mu$)	0.239 ± 0.028	0.307 ± 0.043	-	0.107 ± 0.016	0.694 ± 0.089	117 ± 20	0.064 ± 0.014	115	0.98 ± 0.19	0.97 ± 0.19
Z mass veto ($eee+\mu\mu\mu$)	0.144 ± 0.017	-	-	-	0.182 ± 0.022	9.5 ± 2.0	0.059 ± 0.015	8	0.84 ± 0.35	0.83 ± 0.34
$m_{ll,min}$ and $m_{ll,max}$ cuts ($eee+\mu\mu\mu$)	0.122 ± 0.014	-	-	-	0.156 ± 0.019	6.7 ± 1.5	0.060 ± 0.016	5	0.75 ± 0.38	0.73 ± 0.37
$\Delta R_{ll} < 2.0$ ($eee+\mu\mu\mu$)	0.117 ± 0.014	-	-	-	0.146 ± 0.018	4.7 ± 1.1	0.067 ± 0.017	5	1.06 ± 0.53	1.03 ± 0.51
SS-leptons OR ($eee+\mu\mu\mu$)	0.116 ± 0.012	-	-	-	0.146 ± 0.016	4.70 ± 0.92	0.067 ± 0.015	5	1.06 ± 0.52	1.03 ± 0.50
$\ell\nu\ell\nu$ OR ($eee+\mu\mu\mu$)	0.116 ± 0.012	-	-	-	0.145 ± 0.016	4.65 ± 0.90	0.067 ± 0.015	5	1.06 ± 0.52	1.03 ± 0.50
1SFOS ($ee\mu+\mu\mu e$)	0.646 ± 0.075	0.687 ± 0.093	0.145 ± 0.019	0.277 ± 0.035	1.75 ± 0.22	666 ± 122	0.068 ± 0.015	642	0.96 ± 0.18	0.96 ± 0.18
num. jets < 2 ($ee\mu+\mu\mu e$)	0.603 ± 0.070	0.517 ± 0.071	0.134 ± 0.018	0.228 ± 0.030	1.48 ± 0.18	599 ± 107	0.061 ± 0.013	569	0.95 ± 0.18	0.95 ± 0.17
top-veto ($ee\mu+\mu\mu e$)	0.584 ± 0.068	0.474 ± 0.066	0.133 ± 0.018	0.200 ± 0.027	1.39 ± 0.17	575 ± 102	0.058 ± 0.013	547	0.95 ± 0.17	0.95 ± 0.17
E_T^{miss} and $E_{T,TrackHWW}^{miss}$ cuts ($ee\mu+\mu\mu e$)	0.463 ± 0.054	0.320 ± 0.044	0.088 ± 0.013	0.135 ± 0.019	1.01 ± 0.12	117 ± 21	0.093 ± 0.021	132	1.12 ± 0.23	1.11 ± 0.23
Z mass veto ($ee\mu+\mu\mu e$)	0.365 ± 0.043	-	-	-	0.479 ± 0.057	15.4 ± 4.0	0.121 ± 0.035	20	1.30 ± 0.44	1.26 ± 0.43
$m_{ll,min}$ and $m_{ll,max}$ cuts ($ee\mu+\mu\mu e$)	0.319 ± 0.037	-	-	-	0.419 ± 0.050	11.4 ± 3.3	0.123 ± 0.038	17	1.49 ± 0.56	1.44 ± 0.53
$\Delta R_{ll} < 2.0$ ($ee\mu+\mu\mu e$)	0.299 ± 0.035	-	-	-	0.374 ± 0.045	7.4 ± 2.1	0.137 ± 0.042	7	0.95 ± 0.45	0.91 ± 0.42
SS-leptons OR ($ee\mu+\mu\mu e$)	0.298 ± 0.032	-	-	-	0.373 ± 0.041	7.3 ± 1.8	0.137 ± 0.037	7	0.96 ± 0.43	0.91 ± 0.41
$\ell\nu\ell\nu$ OR ($ee\mu+\mu\mu e$)	0.292 ± 0.031	-	-	-	0.366 ± 0.041	7.0 ± 1.8	0.137 ± 0.032	6	0.86 ± 0.42	0.82 ± 0.40
0SFOS ($\ell\ell\ell$)	0.319 ± 0.037	-	0.070 ± 0.011	-	0.441 ± 0.052	8.3 ± 2.9	0.152 ± 0.057	7	0.84 ± 0.44	0.80 ± 0.41
num. jets < 2 ($\ell\ell\ell$)	0.299 ± 0.035	-	0.066 ± 0.010	-	0.408 ± 0.049	4.9 ± 1.6	0.181 ± 0.061	2	0.41 ± 0.31	0.37 ± 0.29
top-veto ($\ell\ell\ell$)	0.289 ± 0.034	-	0.064 ± 0.010	-	0.393 ± 0.047	3.39 ± 0.89	0.209 ± 0.060	2	0.59 ± 0.44	0.53 ± 0.40
$m_{ll,min}$ and $m_{ll,max}$ cuts ($\ell\ell\ell$)	0.271 ± 0.031	-	-	-	0.370 ± 0.044	2.86 ± 0.75	0.214 ± 0.062	2	0.70 ± 0.53	0.62 ± 0.46
$\Delta R_{ll} < 2.0$ ($\ell\ell\ell$)	0.271 ± 0.031	-	-	-	0.370 ± 0.044	2.86 ± 0.75	0.214 ± 0.062	2	0.70 ± 0.53	0.62 ± 0.46
SS-leptons OR ($\ell\ell\ell$)	0.270 ± 0.029	-	-	-	0.368 ± 0.041	2.85 ± 0.73	0.213 ± 0.060	2	0.70 ± 0.53	0.62 ± 0.46
$\ell\nu\ell\nu$ OR ($\ell\ell\ell$)	0.263 ± 0.021	-	-	-	0.358 ± 0.040	2.47 ± 0.66	0.222 ± 0.055	2	0.81 ± 0.51	0.71 ± 0.43

TABLE 4.15: 7 TeV 3ℓ analysis: number of expected events for the signal and total MC at each step of the event selection described in Tab. 4.7. The "sign." in the last column stands for significance, which is defined through the formula $\sqrt{2((s+b)\ln(1+\frac{s}{b})-s)}$, where s represents the number of signal events and b the background ones. The breakdown of background sources in presented in Tab. 4.16.

	VH (125 GeV)	$WZ/W\gamma^*$	ZZ^*	WW	VVV	Z/γ^*	$Z\gamma$	top	$ggF/VBF/ttH$	Total Bkg.
Pre-selection ($\ell\ell\ell$)	3.52 ± 0.40	347 ± 40	321 ± 83	0.544 ± 0.079	2.516 ± 0.076	123 ± 19	353 ± 50	32 ± 14	1.788 ± 0.065	1183 ± 215
3SF + 1SFOS ($\ell\ell\ell$)	3.08 ± 0.38	346 ± 47	320 ± 83	0.474 ± 0.073	1.99 ± 0.49	123 ± 19	352 ± 50	27 ± 12	1.54 ± 0.14	1175 ± 212
num. jets < 2 ($\ell\ell\ell$)	2.56 ± 0.32	305 ± 42	295 ± 76	0.393 ± 0.067	1.80 ± 0.44	106 ± 16	336 ± 48	8.2 ± 3.8	0.788 ± 0.073	1055 ± 186
top-veto ($\ell\ell\ell$)	2.37 ± 0.30	291 ± 40	284 ± 73	0.348 ± 0.062	1.71 ± 0.42	101 ± 15	327 ± 46	3.4 ± 1.7	0.723 ± 0.066	1011 ± 178
E_T^{miss} and $E_{T,TrackHWW}^{miss}$ cuts ($\ell\ell\ell$)	1.70 ± 0.21	199 ± 27	18.2 ± 5.0	0.211 ± 0.055	1.40 ± 0.35	5.5 ± 2.0	7.6 ± 2.1	2.8 ± 1.4	0.061 ± 0.012	235 ± 37
Z mass veto ($\ell\ell\ell$)	0.661 ± 0.080	15.2 ± 2.2	3.1 ± 1.0	0.117 ± 0.045	0.69 ± 0.19	1.59 ± 0.82	2.69 ± 0.72	1.54 ± 0.81	-	24.9 ± 5.4
$m_{ll,min}$ and $m_{ll,max}$ cuts ($\ell\ell\ell$)	0.575 ± 0.070	10.2 ± 1.5	2.37 ± 0.84	0.078 ± 0.040	0.45 ± 0.12	1.37 ± 0.78	2.29 ± 0.64	1.28 ± 0.70	-	18.1 ± 4.2
$\Delta R_{ll} < 2.0$ ($\ell\ell\ell$)	0.521 ± 0.063	7.4 ± 1.1	1.40 ± 0.49	0.055 ± 0.036	0.293 ± 0.077	0.95 ± 0.46	1.17 ± 0.42	0.77 ± 0.42	-	12.1 ± 2.7
SS-leptons OR ($\ell\ell\ell$)	0.519 ± 0.057	7.35 ± 0.93	1.40 ± 0.48	0.055 ± 0.036	0.292 ± 0.015	0.95 ± 0.46	1.17 ± 0.42	0.76 ± 0.42	-	12.0 ± 2.4
$\ell\nu\ell\nu$ OR ($\ell\ell\ell$)	0.511 ± 0.052	7.22 ± 0.91	1.38 ± 0.48	0.055 ± 0.036	-	0.95 ± 0.46	1.17 ± 0.42	0.56 ± 0.34	-	11.6 ± 2.4
3SF ($eee + \mu\mu\mu$)	1.33 ± 0.17	174 ± 27	151 ± 39	0.104 ± 0.033	0.74 ± 0.25	48.0 ± 8.0	123 ± 18	11.0 ± 5.0	0.683 ± 0.082	509 ± 97
num. jets < 2 ($eee + \mu\mu\mu$)	1.07 ± 0.14	154 ± 24	139 ± 36	0.103 ± 0.033	0.67 ± 0.23	40.5 ± 6.9	117 ± 17	3.1 ± 1.5	0.393 ± 0.048	455 ± 85
top-veto ($eee + \mu\mu\mu$)	0.98 ± 0.12	147 ± 23	134 ± 34	0.093 ± 0.032	0.64 ± 0.21	38.5 ± 6.6	114 ± 17	1.25 ± 0.65	0.363 ± 0.044	436 ± 81
E_T^{miss} and $E_{T,TrackHWW}^{miss}$ cuts ($eee + \mu\mu\mu$)	0.694 ± 0.089	102 ± 16	9.4 ± 2.5	0.055 ± 0.024	0.51 ± 0.17	1.93 ± 0.63	2.22 ± 0.84	1.06 ± 0.58	-	117 ± 20
Z mass veto ($eee + \mu\mu\mu$)	0.182 ± 0.022	6.3 ± 1.1	1.39 ± 0.47	0.044 ± 0.022	0.181 ± 0.062	0.50 ± 0.33	0.68 ± 0.27	0.34 ± 0.23	-	9.5 ± 2.0
$m_{ll,min}$ and $m_{ll,max}$ cuts ($eee + \mu\mu\mu$)	0.156 ± 0.019	4.27 ± 0.72	1.08 ± 0.41	0.032 ± 0.018	0.118 ± 0.041	0.36 ± 0.30	0.61 ± 0.24	0.20 ± 0.18	-	6.7 ± 1.5
$\Delta R_{ll} < 2.0$ ($eee + \mu\mu\mu$)	0.146 ± 0.018	3.21 ± 0.56	0.59 ± 0.20	0.021 ± 0.014	0.083 ± 0.029	0.36 ± 0.30	0.31 ± 0.14	0.12 ± 0.14	-	4.7 ± 1.1
SS-leptons OR ($eee + \mu\mu\mu$)	0.146 ± 0.016	3.21 ± 0.44	0.59 ± 0.20	0.021 ± 0.014	-	0.36 ± 0.30	0.31 ± 0.14	0.12 ± 0.14	-	4.70 ± 0.92
$\ell\nu\ell\nu$ OR ($eee + \mu\mu\mu$)	0.145 ± 0.016	3.16 ± 0.44	0.59 ± 0.20	0.021 ± 0.014	-	0.36 ± 0.30	0.31 ± 0.14	0.12 ± 0.14	-	4.65 ± 0.91
1SFOS ($ee\mu + \mu\mu e$)	1.75 ± 0.22	172 ± 27	169 ± 44	0.370 ± 0.064	1.24 ± 0.42	75 ± 11	229 ± 32	16.4 ± 7.5	0.86 ± 0.10	666 ± 122
num. jets < 2 ($ee\mu + \mu\mu e$)	1.48 ± 0.18	151 ± 23	156 ± 40	0.289 ± 0.058	1.13 ± 0.38	66 ± 10	218 ± 30	5.1 ± 2.4	0.395 ± 0.049	599 ± 107
top-veto ($ee\mu + \mu\mu e$)	1.39 ± 0.17	144 ± 22	150 ± 39	0.254 ± 0.053	1.08 ± 0.36	62 ± 10	213 ± 30	2.2 ± 1.1	0.360 ± 0.044	575 ± 102
E_T^{miss} and $E_{T,TrackHWW}^{miss}$ cuts ($ee\mu + \mu\mu e$)	1.01 ± 0.12	96 ± 15	8.9 ± 2.5	0.156 ± 0.049	0.89 ± 0.30	3.5 ± 1.7	5.4 ± 1.4	1.79 ± 0.89	-	117 ± 21
Z mass veto ($ee\mu + \mu\mu e$)	0.479 ± 0.057	8.9 ± 1.5	1.66 ± 0.68	0.073 ± 0.039	0.51 ± 0.17	1.09 ± 0.73	2.01 ± 0.59	1.20 ± 0.64	-	15.4 ± 4.0
$m_{ll,min}$ and $m_{ll,max}$ cuts ($ee\mu + \mu\mu e$)	0.419 ± 0.050	6.0 ± 1.0	1.29 ± 0.61	0.046 ± 0.035	0.33 ± 0.11	1.01 ± 0.71	1.68 ± 0.53	1.07 ± 0.58	-	11.4 ± 3.3
$\Delta R_{ll} < 2.0$ ($ee\mu + \mu\mu e$)	0.374 ± 0.045	4.18 ± 0.71	0.81 ± 0.38	0.034 ± 0.033	0.210 ± 0.072	0.59 ± 0.34	0.87 ± 0.38	0.65 ± 0.36	-	7.4 ± 2.1
SS-leptons OR ($ee\mu + \mu\mu e$)	0.373 ± 0.041	4.14 ± 0.55	0.81 ± 0.38	0.034 ± 0.033	0.210 ± 0.013	0.59 ± 0.34	0.87 ± 0.38	0.64 ± 0.35	-	7.3 ± 1.8
$\ell\nu\ell\nu$ OR ($ee\mu + \mu\mu e$)	0.366 ± 0.040	4.06 ± 0.50	0.79 ± 0.38	0.034 ± 0.033	-	0.59 ± 0.34	0.87 ± 0.38	0.44 ± 0.27	-	7.0 ± 1.7
0SFOS ($\ell\ell\ell$)	0.441 ± 0.052	1.18 ± 0.19	0.53 ± 0.15	0.070 ± 0.028	0.527 ± 0.046	0.36 ± 0.22	0.030 ± 0.031	5.4 ± 2.5	0.250 ± 0.035	8.3 ± 2.9
num. jets < 2 ($\ell\ell\ell$)	0.408 ± 0.049	1.05 ± 0.17	0.48 ± 0.14	0.070 ± 0.028	0.484 ± 0.042	0.36 ± 0.22	0.030 ± 0.031	2.4 ± 1.2	-	4.9 ± 1.6
top-veto ($\ell\ell\ell$)	0.393 ± 0.047	1.01 ± 0.17	0.46 ± 0.14	0.058 ± 0.025	0.470 ± 0.041	0.36 ± 0.22	0.030 ± 0.031	1.00 ± 0.51	-	3.39 ± 0.89
$m_{ll,min}$ and $m_{ll,max}$ cuts ($\ell\ell\ell$)	0.370 ± 0.044	0.88 ± 0.15	0.43 ± 0.13	0.046 ± 0.023	0.346 ± 0.031	0.36 ± 0.22	0.030 ± 0.031	0.75 ± 0.40	-	2.86 ± 0.75
$\Delta R_{ll} < 2.0$ ($\ell\ell\ell$)	0.370 ± 0.044	0.88 ± 0.15	0.43 ± 0.13	0.046 ± 0.023	0.346 ± 0.031	0.36 ± 0.22	0.030 ± 0.031	0.75 ± 0.40	-	2.86 ± 0.75
SS-leptons OR ($\ell\ell\ell$)	0.368 ± 0.041	0.88 ± 0.14	0.43 ± 0.13	0.046 ± 0.025	0.345 ± 0.017	0.36 ± 0.22	0.030 ± 0.031	0.75 ± 0.40	-	2.85 ± 0.73
$\ell\nu\ell\nu$ OR ($\ell\ell\ell$)	0.358 ± 0.040	0.85 ± 0.13	0.42 ± 0.13	0.023 ± 0.020	0.338 ± 0.013	0.36 ± 0.22	0.030 ± 0.031	0.44 ± 0.29	-	2.47 ± 0.66

TABLE 4.16: 7 TeV 3ℓ analysis: number of expected events for the different background processes at each step of the event selection described in Tab. 4.7.

The basic features of the 3ℓ Multivariate Analysis for the 7 TeV data are identical to the ones already described for the 8 TeV data analysis, namely the same set of input variables and of training events. For this reason the same values of the optimised BDT parameters used for 8 TeV data analysis have been used also for the 7 TeV data analysis. With these parameters the training with 7 TeV MC samples has been done.
Fig. 5.3 shows the BDT Score distribution for the signal and for all the backgrounds, after the event selection.
The only difference in the 7 TeV CRs with respect to 8 TeV selection is that the following: the Z+jets μ-fake CR has been dropped in the 3ℓ analysis due to the very limited statistics Also for the 7 TeV analysis, in order to achieve the best sensitivity, a fit to the shape of the BDT Score distribution for 3SF+1SFOS has been performed as well as a fit to the shape of $\Delta R_{\ell_0,\ell_1}$ distribution in 0SFOS reported in Fig. 5.3. To acknowledge the low statistics of 7 TeV analysis an example BDT Score distribution in CRs is reported in Fig. 4.19. The fit is performed in the limit setting procedure as explained in Sec. 5.2.

Tab. 4.17 summarises the expected composition of the background events and the number of observed events in the control regions. Tab. 5.1 shows the normalisation factors extracted from the final fit.

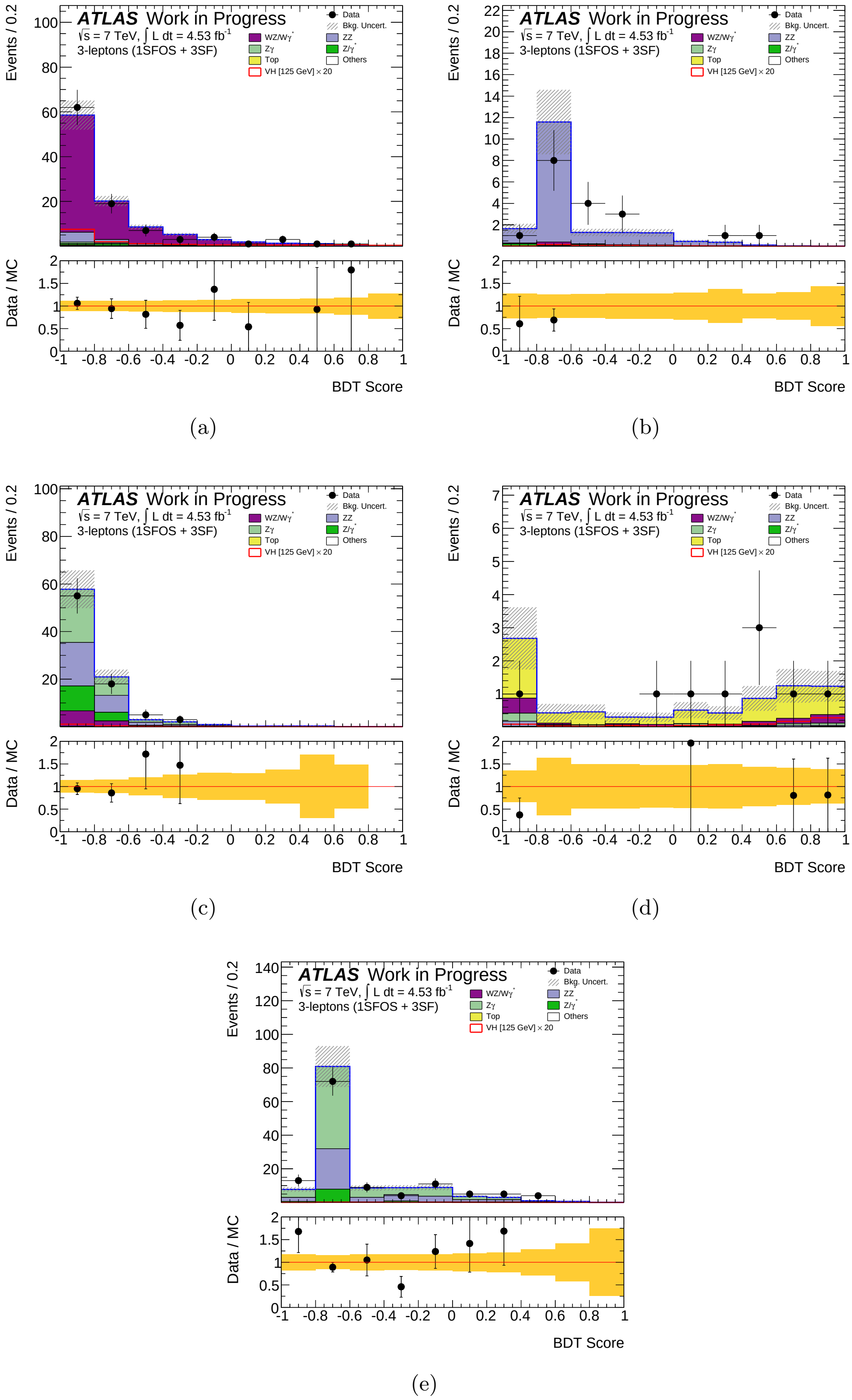

FIGURE 4.19: Distributions of BDT Score in the 3ℓ control regions: (a) 3ℓ-WZ-CR, (b) 3ℓ-ZZ-CR, (c) 3ℓ-Zjets-CR, (d) 3ℓ-Top-CR, (e) 3ℓ-$Z\gamma$-CR. Data (dots) are compared to background expectation from the simulation of the background components, normalised using the NFs from the final fit (stacked filled histograms). Expectations for SM Higgs boson associated production with m_H = 125 GeV are multiplied by a factor 20 and presented as a non-stacked unfilled histogram.

	Obs.	Total Bkg.	Data/MC	VH (125 GeV)	Total Bkg. + Sig	Data/(MC+Sig)	$WZ/W\gamma^*$	$W\gamma$	ZZ^*	WW	VVV	Z/γ^*	$Z\gamma$	top	$ggF/VBF/ttH$
WZ CR ($\ell\ell\ell$)	101	100 ± 15	1.00 ± 0.19	0.730 ± 0.041	101 ± 16	1.00 ± 0.19	88 ± 12	-	7.5 ± 2.0	0.032 ± 0.024	0.360 ± 0.091	1.48 ± 0.75	1.85 ± 0.76	0.71 ± 0.37	-
ZZ CR ($\ell\ell\ell$)	18	18.1 ± 4.6	1.00 ± 0.35	-	18.1 ± 4.6	1.00 ± 0.34	0.56 ± 0.14	-	16.8 ± 4.4	0.011 ± 0.037	-	0.55 ± 0.23	0.100 ± 0.073	0.000 ± 0.042	0.065 ± 0.013
$Z\gamma$ CR ($\ell\ell\ell$)	123	122 ± 26	1.00 ± 0.23	-	122 ± 26	1.00 ± 0.23	0.75 ± 0.15	-	39 ± 10	-	-	10.1 ± 2.3	72 ± 13	0.047 ± 0.045	0.051 ± 0.012
Z+jets CR (e-fake)	68	67 ± 15	1.01 ± 0.26	0.042 ± 0.015	67 ± 15	1.01 ± 0.26	4.64 ± 0.75	-	17.3 ± 4.7	-	-	12.8 ± 3.3	32.7 ± 7.2	0.054 ± 0.092	0.064 ± 0.015
Top CR ($\ell\ell\ell$)	9	8.8 ± 3.8	1.02 ± 0.55	0.043 ± 0.011	8.8 ± 3.8	1.02 ± 0.55	1.21 ± 0.26	-	0.37 ± 0.19	0.012 ± 0.022	0.045 ± 0.014	0.03 ± 0.19	0.57 ± 0.30	6.2 ± 2.9	0.320 ± 0.041

TABLE 4.17: 7 TeV 3ℓ analysis: number of expected and observed events in the control regions defined in Tab. 4.11.

4.7 Systematic uncertainties

Theoretical and experimental uncertainties are evaluated on the background and signal events yield both in the CRs and in the SRs. Contributions from minor backgrounds that do not have any visible effect on the final result are neglected. In applying the systematic uncertainties in the final statistical fit, the signal and background processes are categorised in one of the following three types depending on how they are estimated:

- Purely MC predicted processes;
- Background processes normalised from CRs;
- Fully data-driven estimated background processes.

For MC predicted processes the various sources of common and specific systematic uncertainties described in the following sub-sections are applied to evaluate the effects on the theoretical expected yield. For background processes normalised with data the effects of the systematic uncertainties in the CRs (that, in general, are different from the effects in the SR) are taken into account in the fitting procedure. The experimental systematic variations are applied to both SRs and CRs and the effects are correlated in the fit. The theory systematic uncertainties are assigned to the extrapolation factor α defined in the following

$$\begin{aligned} N_{bkg}^{SR,\ est} &= \frac{N_{MC,\ bkg}^{SR}}{N_{MC,\ bkg}^{CR}} \times (N_{data}^{CR} - N_{MC,\ other\ bkg}^{CR}), \\ &= \alpha \times (N_{data}^{CR} - N_{MC,\ other\ bkg}^{CR}), \end{aligned} \tag{4.1}$$

where $N_{bkg}^{SR,\ est}$ is estimated number of the events from a background source in the SR, $N_{MC,\ bkg}^{SR}$ and $N_{MC,\ bkg}^{CR}$ are the number of MC events from that source in the SR and CR, respectively. N_{data}^{CR} is the number of observed events in the CR, and $N_{MC,\ other\ bkg}^{CR}$ is the number of expected MC events from the other background processes in the CR. The only fully data-driven estimated background is the W+jet and QCD contribution in the 2ℓ-SS and 2ℓ-DFOS analyses. The systematic uncertainties on this estimation are summarised in Ref. [61].

In the following sub-section the different sources of systematic uncertainties, both of theoretical and experimental origin, are explained in more detail for the 8 TeV analysis. Sec. 4.7.5 details the uncertainties in the 7 TeV one.

4.7.1 Theoretical systematics

The common theoretical uncertainties on the Higgs boson production cross section and branching ratio are summarised in Tab. 4.18 which also includes the naming convention for the associated nuisance parameters adopted in the statistical calculation. The main uncertainty on the VH ($H \to WW^*$) signal, shown in the 'VH Acceptance' row of Tab. 4.18, accounts for the variations in the acceptance of the signal processes. It is dominated by the missing higher order QCD contributions in the $qq \to VH$ PYTHIA8 simulation, evaluated comparing with POWHEG-BOX+PYTHIA8 MC, followed by the parton shower uncertainty evaluated comparing the predictions of POWHEG-BOX+PYTHIA8 with POWHEG-BOX+HERWIG. The uncertainty on the $gg \to ZH$ acceptance has been estimated to be 5% in the 4ℓ categories, in which the process is the most relevant. A conservative estimate of 100% is assigned in the other categories.

Theoretical uncertainties on the Higgs boson production cross sections and branching ratios are evaluated following the recommendation of the LHC Higgs cross section working group [20, 76, 77]. These uncertainties are used commonly to the four analyses. The uncertainty on the the $H \to WW^*$ branching ratio arises from two main sources, missing high-order corrections (theoretical uncertainties) and experimental errors on the SM input parameters, such as quark masses or α_s (parametric uncertainties). Higher order correction can also affect the p_{T} distribution of the radiating gauge boson produced in association with the Higgs boson. The main theoretical systematics are summarised in Tab. 4.18.

Source of Uncertainty	Name in statistical calculation	Affected Sample
QCD scales	QCDscale_Higgs_VH	WH,ZH
	QCDscale_Higgs_ggZH	ZH
	QCDscale_Higgs_ggH	ggF
	QCDscale_Higgs_qqH	VBF
	QCDscale_Higgs_ttH	ttH
PDF and α_{S}	pdf_Higgs_qqH	WH,ZH,VBF
	pdf_Higgs_ggH	ggF
Higgs VV branching ratio	ATLAS_BR_VV	WH,ZH
Higgs $\tau\tau$ branching ratio	ATLAS_BR_tautau	WH,ZH
VH p_{T} reweighting	ATLAS_VHPT_Reweight	WH,ZH
VH Acceptance	VH_xxx_ggZH_ACCEPT	ZH
	VH_xxx_LO2NLO	WH

TABLE 4.18: The common Higgs-related theoretical sources of systematic uncertainties and the samples to which they are applied.

Other theoretical uncertainties on the non Higgs processes are assessed in each analysis as described in Sec. 4.7.4 for the 3ℓ analysis and in Ref. [71] for the $2\ell/4\ell$ analyses.

4.7.2 Experimental systematics

The impact of the experimental uncertainties has been evaluated in a variety of aspects. These sources include the physics objects reconstruction and identification efficiency, the energy resolution, and the energy scales.

The uncertainty of the Jet Energy Scale (JES) is evaluated using a combination of in-situ techniques exploiting the transverse momentum balance between a jet and a reference object as in Ref. [116]. For central jets with $20 \leq p_{\mathrm{T}}^{\mathrm{jet}} \leq 800$ GeV, photons or Z bosons are used as reference objects. A system of low-p_{T} jets is used to extend the JES variation up to the TeV regime. For $p_{\mathrm{T}}^{\mathrm{jet}} > 1$ TeV the JES uncertainty is estimated from single hadron response measurements in-situ and in beam tests. The JES uncertainty for forward jets is derived from di-jet p_{T} balance measurements. The effect of pileup on JES is corrected for as a function of the measured number of primary vertices (N_{PV}) and the expected numbers of pileup events (μ), and an uncertainty is evaluated using in-situ techniques. In 2012, there are two additional components of pileup uncertainty. One component accounts for the residual p_{T} dependence of the pileup correction as a function of N_{PV} and μ, while the other accounts for the residual dependence on the underlying event of the jet energy scale following the jet area-based pileup correction that is currently used. Additional JES uncertainties due to specific event topologies, such as selections of event samples with an enhanced content of jets originating from light quarks or gluons, as well as the uncertainty on the calorimeter response to b-jets, are also evaluated. For a sample of inclusive jets under the average conditions of $\mathrm{N}_{\mathrm{PV}} = 10$ and $\mu = 8.5$ with an RMS of three for both N_{PV} and μ, the total JES uncertainty is evaluated to be below 2%.

The Jet Energy Resolution (JER) uncertainty is evaluated by smearing the jets p_{T} by $+1\sigma$ of a measured uncertainty in a Monte Carlo sample.

The reconstruction, identification, isolation, and trigger efficiencies for electrons and muons, as well as their momentum scales and resolutions, are estimated using $Z \to \ell\ell$, $J/\psi \to \ell\ell$ and $W \to \ell\nu$ events. With the exception of the uncertainty on the electron selection efficiency, which varies up to 5% as a function of p_{T} and η, the resulting uncertainties per lepton are all at the percent level. Uncertainties of the electron reconstruction and identification efficiency are divided into four nuisance parameters based on correlated or uncorrelated characteristics.

The efficiency of the b-tagging algorithm is calibrated using samples containing muons reconstructed in the vicinity of jets [117]. The uncertainties related to b-jet identification are decomposed into six uncorrelated components using the so called eigenvector method. The resulting uncertainty on the b-jet tagging efficiency varies between 2% and 30%

as a function of jet p_{T} for b-jets. The b-tagging efficiencies for c-jets and light jets are also evaluated by using a sample of D^{*+} mesons reconstructed within a jet in the $D^{*+} \to D^0(\to K^-\pi^+)\pi^+$ final state, and inclusive jet samples, respectively [118, 119]. The resulted size of the uncertainty on the c-jet tagging efficiency is found between 1% and 25% depending on jet p_{T}. The uncertainty of the light jet tagging efficiency resulted in the range from 1% to 30%.

The changes in jet energy and lepton energy/momentum due to systematic variations are propagated to $E_{\mathrm{T}}^{\mathrm{miss}}$ and $E_{\mathrm{T}}^{\mathrm{miss}}$; the changes in the high-p_{T} object energy/momentum and in the $E_{\mathrm{T}}^{\mathrm{miss}}$ quantities are, therefore, fully correlated. Additional contributions to the $E_{\mathrm{T}}^{\mathrm{miss}}$ and $E_{\mathrm{T}}^{\mathrm{miss}}$ uncertainty arise from jets with $p_{\mathrm{T}} < 20$ GeV as well as from low-energy calorimeter deposits not associated with reconstructed physics objects [67]. In addition, uncertainties are assigned to the scale and resolution of the remaining $p_{\mathrm{T}}^{\mathrm{miss}}$ component not associated with charged leptons. It is decomposed into the parallel and perpendicular components with respect to the direction of the hard $p_{\mathrm{T}}^{\mathrm{miss}}$. These uncertainties are calculated by comparing the properties of $p_{\mathrm{T}}^{\mathrm{miss}}$ in Z events in data and MC simulation, as a function of the sum of the hard p_{T} objects in the event.

In 8 TeV data, to improve the modelling of the pileup condition, an event-by-event weight is applied on MC samples according the number of interactions per bunch crossing (μ). In 7 TeV data, the MC modelling of the pileup condition is satisfactory, thus no such reweighting is applied. The related systematic uncertainty is given by the variation of the μ rescaling to 0.8 and 1.0.

The uncertainty on the integrated luminosity for the 2012 data is $\pm$ 2.8% and $\pm$1.8% for 2011 data. It is derived following the methodology detailed in Ref. [120].

These uncertainties common to the four analysis, are summarised in Tab. 4.19 with the naming convention adopted in the statistical calculation. The experimental systematics are applied to all samples, with the exception of the luminosity uncertainty which is only applied on fully MC predicted processes.

4.7.3 Experimental systematic uncertainty estimation

The impact of the sources of uncertainties are assessed by varying the components one by one. The procedure is illustrated in the following.

- The systematic source of interest is varied by 1σ,
- All the Monte Carlo samples are re-reconstructed with this change and the analysis is repeated without changing anything else,

Source of Uncertainty	Name in the statistical calculation	Comments
Jet Energy Scale (JES)	ATLAS_JES_201X_Detector1	In-situ method: detector description
	ATLAS_JES_201X_Modelling1	In-situ method: physics modelling
	ATLAS_JES_201X_Statistical11	In-situ method: statistical modelling
	ATLAS_JES_Eta_Modelling	η inter-calibration: physics modelling
	ATLAS_JES_2012_Eta_StatMethod	η inter-calibration: statistical method (in 2012)
	ATLAS_JES_2011_Eta_TotalStat	η inter-calibration: statistical method (in 2011)
	ATLAS_JES_FlavComp	Jet flavour (gluon/quark) composition
	ATLAS_JES_FlavResp	Calorimeter response to gluon jet
	ATLAS_JES_BJET	Calorimeter response to b-jet
	ATLAS_JES_2012_PilePt	Pileup correction: jet p_{T} dependence (in 2012)
	ATLAS_JES_2012_PileRho	Pileup correction: UE modelling dependence (in 2012)
	ATLAS_JES_MU	Pileup correction in terms of μ
	ATLAS_JES_NPV	Pileup correction in terms of N_{PV}
	ATLAS_JES_NonClosure_XXX	Difference in simulation conditions
JER	ATLAS_JER	
Electrons	ATLAS_EL_EFF_ID_CORRLOW	Reconstruction/identification efficiency
	ATLAS_EL_EFF_ID_HIGHPT	Reconstruction/identification efficiency
	ATLAS_EL_EFF_RECOID80015	Reconstruction/identification efficiency
	ATLAS_EL_EFF_RECO_CORR	Reconstruction/identification efficiency
	ATLAS_EF_EFF_ISO	Isolation efficiency
	ATLAS_EL_ESCALE	Energy Scale
	ATLAS_EL_RES	Energy Resolution
Muons	ATLAS_MU_EFF	Reconstruction efficiency
	ATLAS_MU_EFF_ISO	Isolation efficiency
	ATLAS_MU_ESCALE	Energy Scale
	ATLAS_MU_ID_RES	Energy Resolution on inner detector tracks
	ATLAS_MU_MS_RES	Energy Resolution on muon spectrometer tracks
Trigger	ATLAS_EL_TRIGGER_VH	Single electron trigger efficiency
	ATLAS_MU_TRIGGER_VH	Single muon trigger efficiency
	ATLAS_DIL_TRIGGER_VH	Di-lepton trigger efficiency
b-jet tagging	ATLAS_Btag_BxEFF	Efficiency for b-jet (x=1-6)
	ATLAS_Btag_CEFF_201X	Efficiency for c-jet
	ATLAS_Btag_LEFF	Efficiency for light jet
$E_{\mathrm{T}}^{\mathrm{miss}}$ soft term	ATLAS_MET_SCALESOFT	$E_{\mathrm{T}}^{\mathrm{miss}}$ soft term energy scale
	ATLAS_MET_RESOSOFT	$E_{\mathrm{T}}^{\mathrm{miss}}$ soft term energy resolution
	ATLAS_TRACKMET_RESOPARASOFT	$p_{\mathrm{T}}^{\mathrm{miss}}$ energy resolution
	ATLAS_TRACKMET_RESOPERPSOFT	$p_{\mathrm{T}}^{\mathrm{miss}}$ energy resolution
	ATLAS_TRACKMET_SCALESOFT	$p_{\mathrm{T}}^{\mathrm{miss}}$ energy scale
Pileup	ATLAS_MU_RESCALE_lvlv_2012	μ rescaling
Luminosity	ATLAS_LUMI_201X	2.8% (1.8%) in 2012 (2011)
Fake Factor	FakeRate_EL_XXX_HWW	Electron fake rate of jets
	FakeRate_MU_XXX_HWW	Muon fake rate of jets
	FakeRateXXX_QCD_XXX_HWW	Fake rate for QCD estimate

TABLE 4.19: Common experimental sources of systematic uncertainty.

- The impact of the systematic source is evaluated as the impact on the number of events in the signal regions extracted from the statistical fit described in Sec. 5.2.

This procedure is repeated in each analysis to evaluate the uncertainties in its specific phase space. The impact of both the theoretical and experimental uncertainties in each analysis will be presented in the following sections showing the relative events yield for both signal and background.

The 3ℓ analysis is further described in Sec. 4.7.4, details of the 2ℓ and 4ℓ analyses can be found in Ref. [71].

4.7.4 3ℓ analysis

As discussed in Sec. 5.2, in the 3ℓ analysis a fit of the shape of the distributions of the BDT Score and of the $\Delta R_{\ell_0,\ell_1}$ is performed. Fig. 5.2 show the signal and the background content in each bin used to extract the results.

The contributions of theory uncertainties in 3ℓ analysis on the VH signal is around 5% for each SR. It arises from uncertainties on the Higgs branching ratio, on the QCD factorisation and renormalisation scales and on PDFs.

The QCD renormalisation and factorisation scales on $WZ/W\gamma^*$ are varied up and down independently by a factor of two. The relative uncertainties (QCDscale_Bkg_WZ) are determined for each bin of the BDT Score in the 3SF and 1SFOS taking the larger one from the comparison of different variations (3-5%). The impact on the final expected limit is negligible. The following PDF uncertainties on the acceptance are evaluated in each signal region bin for the background processes:

- pdf_Bkg_gg_ACCEPT: PDF acceptance uncertainties on t-quark backgrounds,
- pdf_Bkg_qq_ACCEPT: PDF acceptance uncertainties on WZ, ZZ^*, VVV and Z/γ^* backgrounds.

Each PDF, renormalisation and factorisation scales systematic uncertainty is computed independently for each process as the largest difference between the nominal sample and the ones with "alternative" hypotheses. As example, PDF uncertainties are evaluated by taking the largest difference between the nominal CT10 [96] PDF set and either the MSTW2008 [98] or the NNPDF2.3 [10] PDF set.
The effect of Monte Carlo modelling on the $WZ/W\gamma^*$ background (referred as MCModelling _Bkg_WZ) is estimated comparing samples generated with MC@NLO + Herwig to the nominal sample generated with Powheg + Pythia. From the comparison of the event yield a 11% uncertainty in the 3SF+1SFOS, and 3% effect in the $WZ/W\gamma^*$ CR have quoted. The impact on the extrapolation parameter is 10%. The effect is negligible in the 0SFOS if compared with the Monte Carlo statistical uncertainties. The final effect of the Monte Carlo modelling uncertainty is about 2% in the 3SF+1SFOS limit, while it is negligible in the total 3ℓ combined limit. The theoretical uncertainty on the total background from the VVV normalisation contributes with about 1-2% in 3SF and 1SFOS and less then 1% in 0SFOS where VVV represents one of the main backgrounds. A charge flip systematic is applied in 0SFOS to account for the $WZ/W\gamma^*$ μee contribution. Systematic uncertainties on JES and JER are one of the main experimental components on both signal and the total background.

Source	VH (125 GeV) (%)	WW (%)	$WZ/W\gamma^*$ (%)	ZZ^* (%)	$Z\gamma$ (%)	Z/γ^* (%)	top (%)	VVV (%)	$ggF/VBF/ttH$ (%)	total. bkg (%)
VH Acceptance	9.9	0	0	0	0	0	0	0	0	0
Higgs branching ratio	4.2	0	0	0	0	0	0	0	4.2	0
VH NLO EW correction	1.9	0	0	0	0	0	0	0	0	0
QCD scale	1.2	0	1.4	0	0	0	0	0	7.2	0.96
MC Modelling	0	0	10	0	0	0	0	0	0	7
PDF and α_s	2.1	0	0	2.2	0.51	0.3	0.4	6	7.2	0.33
VVV Kfactor	0	0	0.19	0	0	0	0.45	33	0	1.1
Luminosity	2.8	2.8	0	0	0	0	0	2.8	2.8	0.11
b-jet tagging	0.9	0.44	0	0.8	4.5	0.62	7.4	0.81	1.7	0.55
Trigger	0.39	0.49	0.26	0.22	0.32	1.1	0.16	0.28	0.7	0.16
Electrons	1.6	4.1	0.89	2	4.6	7.3	2.3	1.9	2.2	0.98
Muons	2.2	1.4	0.46	0.76	0.44	0.72	2.3	2.1	2.5	0.4
JER	2	0	0.64	7.5	6.7	3.9	4.5	2.4	1.5	1.6
JES	1.5	17	1.9	8.3	17	24	15	1.2	7.1	2.8
MET soft terms	0	0	0.29	7	15	6.5	2.9	0.91	6.9	1.8
μ rescale	2	13	0.85	11	4.3	15	4.1	3.4	1.4	1.4
Charge Flip	0	0	0	0	0	0	0	0	0	0

TABLE 4.20: 8 TeV relative uncertainties associated with each experimental and theoretical systematic source on the signal and different background components in the 3SF analysis. Numbers smaller than 0.1 are rounded as 0 in this table.

Source	VH (125 GeV) (%)	WW (%)	$WZ/W\gamma^*$ (%)	ZZ^* (%)	$Z\gamma$ (%)	Z/γ^* (%)	top (%)	VVV (%)	$ggF/VBF/ttH$ (%)	total. bkg (%)
VH Acceptance	9.9	0	0	0	0	0	0	0	0	0
Higgs branching ratio	4.2	0	0	0	0	0	0	0	4.2	0
VH NLO EW correction	1.9	0	0	0	0	0	0	0	0	0
QCD scale	1	0	1.5	0	0	0	0	0	7.1	0.94
MC Modelling	0	0	10	0	0	0	0	0	0	6.6
PDF and α_s	2.2	0	0	2.2	0.51	0.29	0.59	6.2	7.1	0.35
VVV Kfactor	0	0	0.19	0	0	0	0.45	33	0	1.9
Luminosity	2.8	2.8	0	0	0	0	0	2.8	2.8	0.17
b-jet tagging	0.82	0.7	0	0.71	1.8	0.47	8.9	0.72	1.5	0.79
Trigger	0.26	0.23	0.17	0	0.39	0.31	0.14	0.19	0.38	0
Electrons	2.2	2.9	0.48	2.9	5.4	4.1	2.4	2.2	3.5	0.35
Muons	1.8	1.4	0.23	0.92	2	12	1.3	1.8	1.9	0.68
JER	1.6	11	0.96	10	11	14	4.7	0.32	5.2	0.14
JES	1.9	0	0.59	2.4	8.5	16	13	1.4	6.3	1.8
$E_{\mathrm{T}}^{\mathrm{miss}}$ soft terms	0	0	0.25	9.5	11	11	1.5	0.62	7.5	1.9
μ rescale	1.4	8	0.98	2.4	6.5	15	1.8	1.7	3.5	0.32
Charge Flip	0	0	0	0	0	0	0	0	0	0

TABLE 4.21: 8 TeV relative uncertainties associated with each experimental and theoretical systematic source on the signal and different background components in the 1SFOS analysis. Numbers smaller than 0.1 are rounded as 0 in this table.

Tab. 4.20, Tab. 4.21 and Tab. 4.22 show the post-fit contribution of systematic uncertainties, grouped by categories, on the signal, each background component and on the total background.

Source	VH (125 GeV) (%)	WW (%)	$WZ/W\gamma^*$ (%)	ZZ^* (%)	Z/γ^* (%)	top (%)	VVV (%)	$ggF/VBF/ttH$ (%)	total. bkg (%)
VH Acceptance	9.9	0	0	0	0	0	0	0	0
Higgs branching ratio	4.2	0	0	0	0	0	0	4.2	0
VH NLO EW correction	1.9	0	0	0	0	0	0	0	0
QCD scale	1	0	0	0	0.13	0	0	7.2	0
MC Modelling	0	0	0	0	0	0	0	0	0
PDF and α_s	2.2	0	0.97	0.32	1.4	0.37	7	7.2	1.6
VVV Kfactor	0	0	0.19	0	0	0.45	3	0	0.52
Luminosity	2.8	2.8	0	0	0	0	2.8	2.8	0.68
b-jet tagging	0.8	0.17	0.22	1.1	0.61	7.8	0.7	1	2.6
Trigger	0.27	0.41	0.19	0.2	0.24	0	0.13	0.59	0
Electrons	2.2	4.7	0.9	1.6	3.1	0.65	2.2	2.9	1.1
Muons	1.7	1.3	0.31	1.2	1.3	0.69	1.7	2.2	0.24
JER	1.3	0	1.7	1.1	0.74	0.81	0.45	3	0.7
JES	2.6	0	0.89	0.99	1	13	1.9	0.38	4
MET soft terms	0	0	0.88	0.4	4.3	1.8	0	4.4	0.59
μ rescale	0.82	12	1.5	5.1	14	0.59	2.2	5.6	1.2
Charge Flip	0	0	5	0	0	0	0	0	1.4

Table 4.22: 8 TeV relative uncertainties associated with each experimental and theoretical systematic source on the signal and different background components in the 0SFOS analysis. Numbers smaller than 0.1 are rounded as 0 in this table.

Source	VH (125 GeV) (%)	WW (%)	$WZ/W\gamma^*$ (%)	ZZ^* (%)	$Z\gamma$ (%)	Z/γ^* (%)	top (%)	VVV (%)	$ggF/VBF/ttH$ (%)	total. bkg (%)
VH Acceptance	9.9	0	0	0	0	0	0	0	0	0
Higgs branching ratio	4.2	0	0	0	0	0	0	0	4.2	0
VH NLO EW correction	1.8	0	0	0	0	0	0	0	0	0
QCD scale	1.1	0	1.7	0	0	0	0	0	7.4	1.1
MC Modelling	0	0	10	0	0	0	0	0	0	7
PDF and α_s	2.6	0	0	1.3	0.21	0.33	0.73	6.1	7.4	0.1
VVV Kfactor	0	0	0.11	0	0	0	0.2	33	0	0.49
Luminosity	1.8	1.8	0	0	0	0	0	1.8	1.8	0
b-jet tagging	0.26	0.54	0.12	0.11	0.62	0.25	7.6	0.18	0.21	0.28
Trigger	0.2	0.5	0.15	0	0.19	0.12	0.12	0.14	0.1	0
Electrons	1.5	6.1	0.56	1.4	2.7	7.2	1.7	1.6	1.6	0.98
Muons	0.56	0	1.4	3.1	0.32	0.71	0.98	2.3	1.7	1.1
JER	0.49	0	2.6	5.4	5	5.2	43	0	2.3	3.6
JES	0.89	0	1.9	21	16	16	23	1.8	4.1	4
MET soft terms	0	0	0.98	4.3	10	4.2	2	0.72	4.9	1.1
Charge Flip	0	0	0	0	0	0	0	0	0	0
MET mismodelling	0	0	3	0	0	0	0	0	0	2

TABLE 4.23: 7 TeV relative uncertainties associated with each experimental and theoretical systematic source on the signal and different background components in the 3SF analysis. Numbers smaller than 0.1 are rounded to 0.

4.7.5 Systematic uncertainties in the 7 TeV analysis

The sources of systematic uncertainties in the $\sqrt{s} = 7$ TeV analysis are very similar to those described for the 8 TeV data analysis in Sec. 4.7. The differences with respect to the 8 TeV data systematic sources are the introduction of two systematic contributions ATLAS_JES_NonClosure and ATLAS_JES_Eta_TotalStat. ATLAS_JES_NonClosure which accounts for residual transverse momentum or energy differences between reconstructed simulation and data after the application of the JES corrections to the nominal MC [121, 122]. ATLAS_JES_Eta_TotalStat, which accounts to the statistical limitations in the MC JES η inter-calibration. For the 3ℓ analysis a $E_{\mathrm{T}}^{\mathrm{miss}}$ mis-modelling systematic has also been evaluated.

The impact from the different sources on the event yield after the fit is presented in Tab. 4.23, Tab. 4.24 and Tab. 4.25.

Source	VH (125 GeV) (%)	WW (%)	$WZ/W\gamma^*$ (%)	ZZ^* (%)	$Z\gamma$ (%)	Z/γ^* (%)	top (%)	VVV (%)	$ggF/VBF/ttH$ (%)	total. bkg (%)
VH Acceptance	9.9	0	0	0	0	0	0	0	0	0
Higgs branching ratio	4.2	0	0	0	0	0	0	0	4.2	0
QCD scale	1.1	0	2	0	0	0	0	0	7.1	1.2
VH NLO EW correction	1.8	0	0	0	0	0	0	0	0	0
MC Modelling	0	0	10	0	0	0	0	0	0	5.9
PDF and α_s	2.6	0	0.11	2.2	0.21	0.29	0.47	6.3	7.3	0.19
VVV Kfactor	0	0	0.11	0	0	0	0.2	33	0	0.89
Luminosity	1.8	1.8	0	0	0	0	0	1.8	1.8	0
b-jet tagging	0.27	2.4	0.12	0.14	0.22	0.69	5.5	0.31	0.49	0.43
Trigger	0.1	0.16	0	0.14	0	0	0.18	0	0	0
Electrons	2.1	14	1.2	1.2	12	12	11	2.1	2.2	1.7
Muons	0.45	0.37	0.86	0.56	9.6	0.7	0.97	0.44	1.2	1.2
JER	0.47	0	1.3	20	29	16	5.3	1	30	3.5
JES	1.1	54	1.6	27	12	30	17	0.97	32	6.3
MET soft terms	0	36	1.2	21	14	9.6	7.6	1	4.8	3.6
Charge Flip	0	0	0	0	0	0	0	0	0	0
MET mismodelling	0	0	3	0	0	0	0	0	0	1.7

Table 4.24: 7 TeV relative uncertainties associated with each experimental and theoretical systematic source on the signal and different background components in the 1SFOS analysis. Numbers smaller than 0.1 is rounded as 0 in this table.

Source	VH (125 GeV) (%)	WW (%)	$WZ/W\gamma^*$ (%)	ZZ^* (%)	Z/γ^* (%)	top (%)	VVV (%)	$ggF/VBF/ttH$ (%)	total. bkg (%)
VH Acceptance	9.9	0	0	0	0	0	0	0	0
Higgs branching ratio	4.2	0	0	0	0	0	0	4.2	0
VH NLO EW correction	1.8	0	0	0	0	0	0	0	0
QCD scale	1.1	0	0	0	0	0	0	6.7	0
MC Modelling	0	0	0	0	0	0	0	0	0
PDF and α_s	2.6	0	0.91	0.1	0.13	0.34	7	6.6	0.9
VVV Kfactor	0	0	0.11	0	0	0.2	2.8	0	0.27
Luminosity	1.8	1.8	0	0	1.7	0	1.8	1.8	0.59
b-jet tagging	0.26	0.54	0.24	0	0.42	4	0.27	0	0.77
Trigger	0.11	0.24	0	0.16	0	0	0	0.16	0
Electrons	2.1	2.7	1.1	1.3	2	1.7	2.1	1.7	1.3
Muons	0.45	0.29	0.23	0.21	0.34	0.97	0.44	0.33	0.21
JER	0.41	0	2.6	0.61	0.33	32	0.48	0	5
JES	1.1	0	1.2	0.74	0.22	9.8	1.3	2.9	1.5
MET soft terms	0	49	0.83	0.57	0.22	9.1	0.14	0	1.7
Charge Flip	0	0	5	0	0	0	0	0	1.6
MET mismodelling	0	0	0	0	0	0	0	0	0

Table 4.25: 7 TeV relative uncertainties associated with each experimental and theoretical systematic source on the signal and different background components in the 0SFOS analysis. Numbers smaller than 0.1 is rounded as 0 in this table.

Chapter 5

Results

A statistical treatment of the results in each considered channel is required in order to obtain information on the physics processes under investigation. The events yield in the SRs and CRs, the MC prediction, the statistical and systematic uncertainties, the theoretical uncertainties together with possible correlations need to be taken into account properly.
This Chapter presents the event yield measured after the selections for each channel and the statistical tools adopted to extract the results from the data. The significance of signal events will be given in the end of the Chapter.

5.1 Event yield and Normalisation Factors

As described in Sec. 5.2, each background prediction is scaled by a normalisation factor (Tab. 5.1).

The outcome of the selections described in Chapter 4 is summarised in Tab. 5.2 and Tab. 5.3.

As confirmed by the expected number of events at the end of the selections, the most sensitive SR for the VH production[1] is the 3ℓ one, driven by the 0SFOS channel with an expected significance of about 0.7, including the 3SF+1SFOS contribution the 3ℓ SR reaches an expected significance of about 0.8. On the other hand the 4ℓ SR gives an expected significance of 0.4 and 0.6 is expected in the 2ℓ SR. Each contribution is important in order to obtain a global picture of VH production.

[1] Assuming a Higgs mass $m_H \sim 125$ GeV.

(a) 8 TeV data sample

Channel	4ℓ	3ℓ	2ℓ	
Category	2SFOS, 1SFOS	3SF, 1SFOS, 0SFOS	DFOS	SS2jet, SS1jet
Process				
$WZ/W\gamma^*$	—	$1.08^{+0.08}_{-0.06}$	—	0.94 ± 0.10
ZZ^*	$1.03^{+0.11}_{-0.10}$	$1.28^{+0.22}_{-0.20}$	—	—
OS WW	—	—	—	0.80 ± 0.33
$W\gamma$	—	—	—	1.06 ± 0.12
$Z\gamma$	—	$0.62^{+0.15}_{-0.14}$	—	—
Z/γ^*	—	$0.80^{+0.68}_{-0.53}$ (μ-misid) $0.33^{+0.12}_{-0.11}$ (e-misid)	$0.90^{+0.18}_{-0.16}$	0.86 ± 0.30
Top	—	$1.36^{+0.34}_{-0.30}$	$1.05^{+0.16}_{-0.14}$	1.04 ± 0.08

(b) 7 TeV data sample

Process			
$WZ/W\gamma^*$	—	$1.02^{+0.12}_{-0.11}$	—
ZZ^*	$1.59^{+0.36}_{-0.31}$	$1.78^{+0.51}_{-0.42}$	—
OS WW	—	—	—
$W\gamma$	—	—	—
$Z\gamma$	—	$0.45^{+0.09}_{-0.09}$	—
Z/γ^*	—	$0.68^{+0.16}_{-0.15}$ (e-misid)	$1.11^{+0.38}_{-0.34}$
Top	—	$1.25^{+0.66}_{-0.52}$	$0.93^{+0.16}_{-0.14}$

Table 5.1: Summary of background normalisation factors in the (a) 8 TeV and (b) 7 TeV data samples. The uncertainties include both the statistical and systematic components (Sec. 5.2). "—" denotes that the background process, when considered, is normalised by MC simulation [71].

(a) 8 TeV data sample

Process	4ℓ		3ℓ			2ℓ		
Category	2SFOS	1SFOS	3SF	1SFOS	0SFOS	DFOS	SS2jet	SS1jet
Higgs boson								
VH $(H \to WW^*)$	0.203±0.030	0.228±0.034	0.73±0.10	1.61±0.18	1.43±0.16	2.15±0.30	1.04±0.18	2.04±0.30
VH $(H \to \tau\tau)$	0.0084±0.0032	0.012±0.004	0.057±0.011	0.152±0.023	0.248±0.035	—	0.036±0.008	0.27±0.04
ggF	—	—	0.076±0.015	0.085±0.018	—	2.4±0.5	—	—
VBF	—	—	—	—	—	0.180±0.025	—	—
ttH	—	—	—	—	—	—	—	—
Background								
V	—	—	0.22±0.16	1.9±0.6	0.37±0.15	14±4	8±4	15±5
VV	1.17±0.20	0.31±0.06	19±3	28±4	4.7±0.6	10.1±1.6	11.2±2.1	26±4
VVV	0.12±0.04	0.10±0.04	0.8±0.3	2.2±0.7	2.93±0.29	—	—	0.47±0.05
Top	0.014±0.011	—	0.91±0.26	2.4±0.6	3.7±0.9	24±4	0.75±0.19	1.3±0.5
Others	—	—	—	—	—	2.3±0.9	0.71±0.30	0.60±0.24
Total	1.30±0.23	0.41±0.09	22±4	34±6	11.7±1.8	50±5	21±5	44±6

TABLE 5.2: Number of predicted events in the SRs and their composition in the 8 TeV data sample. Background processes that contribute less than 1% of the total background, and Higgs boson production modes that contribute less than 1% of the $VH(H \to WW^*)$ process, are not included in the table. The uncertainties on the event yields include both the statistical and systematic components [71].

7 TeV data sample

Process	4ℓ		3ℓ			
Category	2SFOS	1SFOS	3SF	1SFOS	0SFOS	DFOS
Higgs boson						
$V(H \to WW^*)$	0.0226±0.0033	0.0208±0.0031	0.129±0.013	0.325±0.034	0.291±0.031	0.28±0.05
$V(H \to \tau\tau)$	0.0031±0.0012	0.0014±0.0008	0.0163±0.0035	0.041±0.006	0.067±0.010	0.0075±0.0032
ggF	—	—	0.0045±0.0015	0.0045±0.0019	0.0048±0.0027	0.32±0.09
VBF	—	—	—	—	—	0.021±0.004
$t\bar{t}$H	—	—	—	0.006±0.004	0.0041±0.0032	—
Background						
V	—	—	0.36±0.30	0.59±0.34	0.36±0.22	3.4±1.3
VV	0.37±0.14	0.031±0.013	4.1±0.6	5.7±1.0	1.3±0.2	0.89±0.27
VVV	0.014±0.005	0.0095±0.0033	0.082±0.028	0.21±0.07	0.338±0.031	—
Top	0.006±0.004	—	0.12±0.14	0.4±0.3	0.44±0.29	3.2±0.8
Others	—	—	—	—	—	—
Total	0.39±0.15	0.041±0.016	4.6±1.1	7.0±1.9	2.5±0.7	7.5±1.7

TABLE 5.3: Number of predicted events in the SRs and their composition in the 7 TeV data sample. Background processes that contribute less than 1% of the total background, and Higgs boson production modes that contribute less than 1% of the $VH(H \to WW^*)$ process, are not included in the table. The uncertainties on the event yields include both the statistical and systematic components [71].

5.2 Statistical procedure

The statistical interpretation, which is based on the method in Ref. [61], employs a binned likelihood function. The function is constructed as the product of Poisson probability terms (P_s), obtained from the number of expected signal (S_{ij}), and background (B_{ij}) events and from the observed (N_{ij}) data in each i-th signal region considered:

$$L(\mu, \boldsymbol{\theta}) = \prod_{i}^{N_{SR}} \prod_{j}^{N_{bin}} P_s(N_{ij} \mid \mu S_{ij}(\boldsymbol{\theta}) + B_{ij}(\boldsymbol{\theta})) \times A(\boldsymbol{\theta}) \tag{5.1}$$

N_{SR} is the number of signal regions considered, N_{bin}, as explained later, corresponds to the number of considered bins in the shape analysis for 3ℓ SRs, $\boldsymbol{\theta} = \{\theta_1, \theta_2...\}$ is a vector of the nuisance parameters (NPs) that take into account the background normalisation and the systematic uncertainties. A *signal strength* parameter μ (Eq. 5.2), measuring the signal contribution relative to the Standard Model expectations, represents the Parameter of Interest. Together with the NPs (Eq. 5.2), it is a free parameters and it is fitted from likelihood maximisation procedure. The signal and background expectations are functions of the nuisance parameters $\boldsymbol{\theta}$. The form of these functions depends on the source.

1. In the case of Gaussian systematics $Y = Y_{exp}(1 + \theta\Delta Y)$;
2. Lognormal systematics take the form $Y = Y_{exp}(1 + \Delta Y)^{\theta}$;
3. For the Poisson systematics $Y = Y_{exp}\theta$.

Where Y_{exp} is the nominal value of the signal (S) or background (B) and ΔY is its variation. Systematics uncertainties NPs are taken into account with Gaussian auxiliary constraints and lognormal Monte Carlo expectation parametrisation. Each θ_j represents a different systematic source and since one source can affect multiple signal and background rates in a correlated way the same θ_j can be used everywhere to represent it. The correlation is implemented in the fit procedure where it is needed, for example most of the experimental systematics are correlated between different samples. When correlated, a single systematic source affecting more than one sample is treated as a single NP in the fit.

The background normalisation NPs, are constrained by including the additional measurements from control regions, presented in Sec. 4.5, that provide information on the background rates. $A(\boldsymbol{\theta})$ is an *auxiliary constraint*, that, in case of only one control region defined, can be written as

$$A(\tau) = P_s(N_{CR} \mid \tau B_{CR}) \tag{5.2}$$

where N_{CR} and B_{CR} are the numbers of observed and expected events, respectively, and τ is the normalisation factor. The fitted values for the background NFs are used to present the background expectations in the tables and plots shown in Chapter 4. The minor backgrounds, which do not have floating NPs, as well as data-driven W+jets estimates, are added to the Poisson expectations in Eq. 5.2. When combining all the sub-analyses 107 NPs are present in the fit: 92 from statistical and systematic uncertainties and 15 from background NFs.

The signal is defined as the VH production in which the Higgs boson decays to a W boson pairs. A small contribution from $H \to \tau\tau$ channel is accepted by the event selection and is also included in the statistical interpretation as signal. The ggF and VBF productions are treated as background processes with a the cross section fixed to the SM. The number of events from the background sources found in the different SRs are allowed to fluctuate within the systematic uncertainties, which have been discussed in Sec. 4.7. Further uncertainties, extracted from the fits to the CRs, are assigned to the background processes.

In the 4ℓ analysis two SRs are considered, 4ℓ-2SFOS and 4ℓ-1SFOS. In the 2ℓ analysis, 2ℓ-DFOS is a single SR, 2ℓ-SS1jet and 2ℓ-SS2jet are further split for each flavour combination (ee, $\mu\mu$, $e\mu$, μe). In the 3ℓ analysis, the different signal and background shapes, of the BDT Score in the 3ℓ-3SF and 3ℓ-1SFOS, and of the $\Delta R_{\ell_0,\ell_1}$ in 3ℓ-0SFOS, to gain the maximum sensitivity. The BDT Score is separated into six bins with bounds (-1.0, 0.0, 0.4, 0.6, 0.8, 0.9, 1.0) while $\Delta R_{\ell_0,\ell_1}$ is divided in four bins with bounds (0.0, 0.5, 1.0, 1.5, 5.0). In the BDT Score analysis, the signal region is split in 3ℓ-3SF and 3ℓ-1SFOS, defined by different flavour compositions. These two regions are further subdivided into six regions according to the BDT Score bin boundaries above. Fig. 5.2 and Fig. 5.3 show the distributions the variables with the binning used to extract the results. While the binning was optimised to give the best statistical sensitivity, the number of bins used was limited by the available MC statistics.

To properly take into account both the statistical and systematic variations in the shape of the distributions each bin is given its own statistical and systematic error and correlations due to systematic effects are taken into account within the global fit through common nuisance parameters. The systematic uncertainties are extrapolated from control region to signal region in the fit as well. In the shape analysis, each bin is treated as a separate SR so that one can consider the shape fit as a cut and count analysis in each bin. In this case the likelihood function is built from the product over the number of BDT Score and $\Delta R_{\ell_0,\ell_1}$ bins N_{bin}.

The systematic uncertainties are propagated in each BDT Score and $\Delta R_{\ell_0,\ell_1}$ bin for each source, and properly correlated adopting the same NPs in each bin. Since the rate of each signal and background source is modified independently in each bin according to the predicted variation for the MC, a systematic effect will change both the normalisation and the shape at the same time with the proper correlation predicted by the MC.

5.3 Statistical results

The signal extraction is performed using the profile likelihood ratio method, which consists of maximising a binned likelihood function $\mathcal{L}(\mu, \boldsymbol{\theta} \mid \boldsymbol{n})$, where $\boldsymbol{n}$ represents the observed events in each SR and CR.
The test statistic q_μ is defined as

$$q_\mu = -2\ln\frac{\mathcal{L}(\mu, \hat{\boldsymbol{\theta}}_{\boldsymbol{\mu}})}{\mathcal{L}_{\max}} = -2\ln\Lambda. \tag{5.3}$$

The symbol $\hat{\boldsymbol{\theta}}_{\boldsymbol{\mu}}$ indicates the nuisance parameter values at the maximum of the likelihood for a given μ. The denominator is the maximum value of $\mathcal{L}$ obtained floating both μ and θ. When the denominator is maximised, μ takes the value of $\hat{\mu}$. The p_0 value is computed for the test statistic q_0 evaluated at $\mu = 0$ in Eq. 5.3, and is defined to be the probability to obtain a value of q_0 larger than the observed value under the background-only hypothesis. There are no bounds on $\hat{\mu}$, although q_0 is defined to be negative if $\hat{\mu} \leq 0$.
The equivalent formulation, expressed in terms of the number of standard deviations, σ, is referred to as the local significance Z_0. In this case it is computed in the context of the statistical framework in which the asymptotic limit is valid and the parameters follow a Gaussian distribution, while in the tables of Chapter 4 the significance is computed assuming a Poisson counting experiment.
Applying the selections described in Sec. 4.3, the expected significance can be computed for a range of different values of the Higgs boson mass. The significance does not change much, as shown in Fig. 5.1, since the $H \to WW^*$ decay channel has a rather poor mass resolution for $m_H \lesssim 2m_{\boldsymbol{W}}$. The main limitation to the sensitivity to $VH(H \to WW^*)$ process is the $H \to WW^*$ branching ratio. The signal acceptance for all production modes and decays are computed assuming the SM Higgs boson with $m_H = 125.36$ GeV, corresponding to the combination of the masses measured in the $H \to \gamma\gamma$ and $H \to 4\ell$ decays by ATLAS [123]. The acceptance for this mass results from an interpolation between the acceptances computed at $m_H = 125$ GeV and 130 GeV.
For a Higgs boson with a mass $m_H \sim 125$ GeV a 0.9 significance is expected.

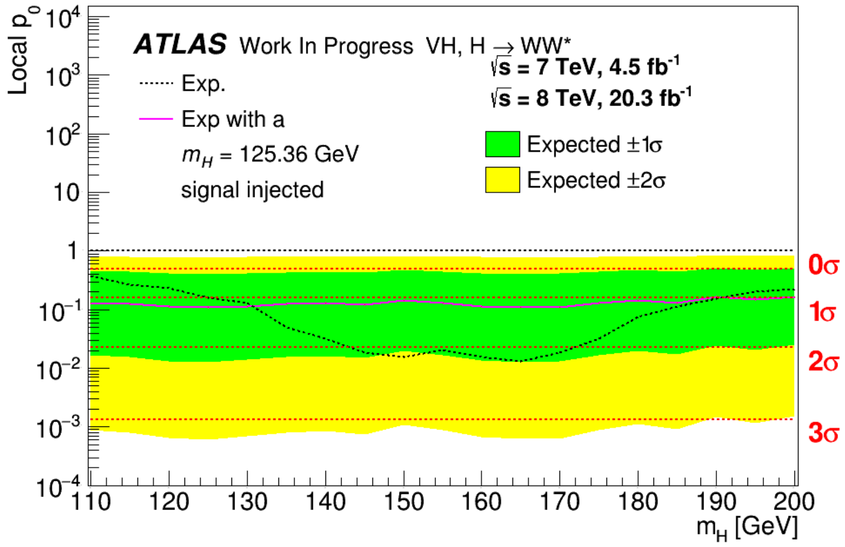

FIGURE 5.1: Search for Higgs boson production in association with a W or a Z boson in the $H \to WW^*$ decay. The dashed line shows the expected values given the presence of a signal at each x-axis value. The expected values for $m_H = 125.36$ GeV (signal injected) are given by a purple line [71].

5.3.1 Characterisation of the excess

The observed events at the end of the selections are reported in Tab. 5.4, the main signal target is also reported as well the predicted total background. A global excess with respect to the only-background hypothesis is observed.
In Fig. 5.2 and Fig. 5.3 the 3ℓ variables relevant for the statistical procedure are shown.

8 TeV data sample

Process	4ℓ		3ℓ			2ℓ		
Category	2SFOS	1SFOS	3SF	1SFOS	0SFOS	DFOS	SS2jet	SS1jet
$VH\ (H \to WW^*)$	0.203±0.030	0.228±0.034	0.73±0.10	1.61±0.18	1.43±0.16	2.15±0.30	1.04±0.18	2.04±0.30
Total Background	1.30±0.23	0.41±0.09	22±4	34±6	11.7±1.8	50±5	21±5	44±6
Observed events	0	3	22	38	14	63	25	62

7 TeV data sample

Process	4ℓ		3ℓ			2ℓ
Category	2SFOS	1SFOS	3SF	1SFOS	0SFOS	DFOS
$V(H \to WW^*)$	0.0226±0.0033	0.0208±0.0031	0.129±0.013	0.325±0.034	0.291±0.031	0.28±0.05
Total Background	0.39±0.15	0.041±0.016	4.6±1.1	7.0±1.9	2.5±0.7	7.5±1.7
Observed events	1	0	5	6	2	7

TABLE 5.4: Number of observed and predicted events in the SRs in the 8 TeV and 7 TeV data sample. SS analysis is not performed in 7 TeV data sample. The total background and the Higgs signal target $VH(H \to WW^*)$ are included in the table. The uncertainties on the event yields include both the statistical and systematic components [71].

The expected sensitivity (Z_0) to the SM Higgs boson with mass $m_H = 125.36$ GeV, the observed Z_0 for $H \to WW^*$ decays and the measured μ value using the 4ℓ, 3ℓ and 2ℓ

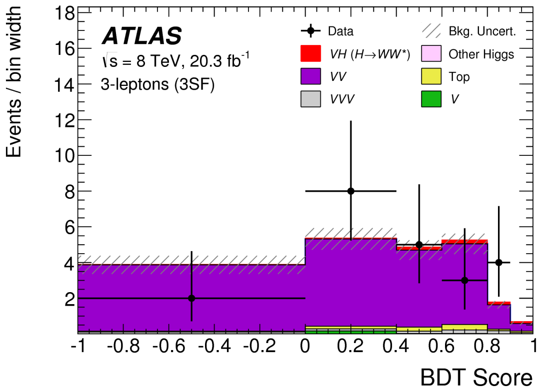

(a)

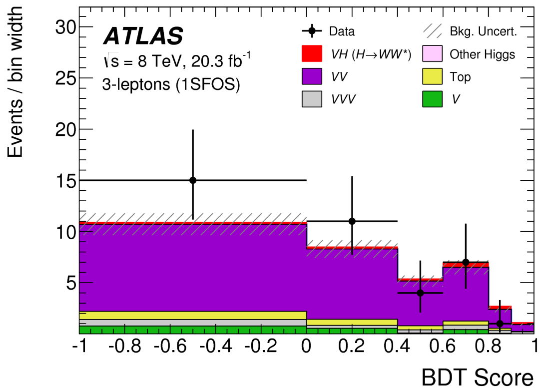

(b)

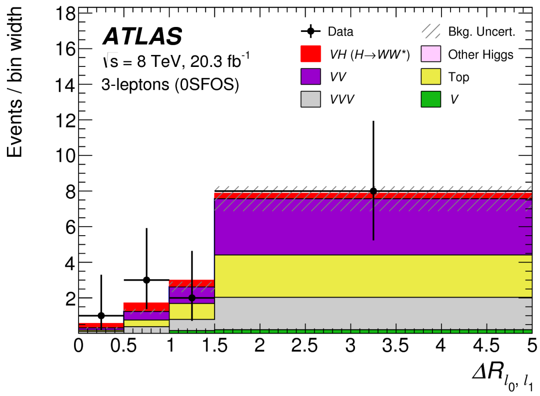

(c)

FIGURE 5.2: Distributions of relevant quantities for the 3ℓ analyses, using 8 TeV data: (a) BDT Score in 3ℓ-3SF and (b) in 3ℓ-1SFOS, and (c) the angular separation in R of the two opposite-sign leptons with smaller ΔR distance, $\Delta R_{\ell_0\ell_1}$, in 3ℓ-0SFOS. Data (dots) are compared to the background plus $VH(H\to WW^*)$ (m_H=125 GeV) signal expectation (stacked filled histograms). The hatched area on the histogram represents the total uncertainty on the background estimate including the statistical and systematic uncertainties added in quadrature [71].

categories are shown in Tab. 5.4. A global excess with respect to a background-only hypotesis is observed except of in 4ℓ-2SFOS, 3ℓ-3SF and 3ℓ-1SFOS SRs and this reflects to a negative μ obtained in such SRs from the global fit. Anyway the measured μ in 4ℓ, 3ℓ and 2ℓ channels are still compatible with SM expectation at 95% C.L. (Fig. 5.7) and it is mostly affected by the limited statistics at the end of selections.
The numbers in Tab. 5.4 are computed adding the contributions from the ggF and VBF production to the signal component and the relative strengths of the VH, ggF and VBF productions are fixed to the SM values and constrained with their theoretical uncertainties. Fig. 5.5 presents expected and observed p_0 as a function of the mass hypothesis. A deviation from a background-only hypothesis corresponding at 2.4σ has been observed for a Higgs boson mass of $m_H = 125.36$ GeV.

Given the missing observation of VH production mode in the analysis, it is useful to

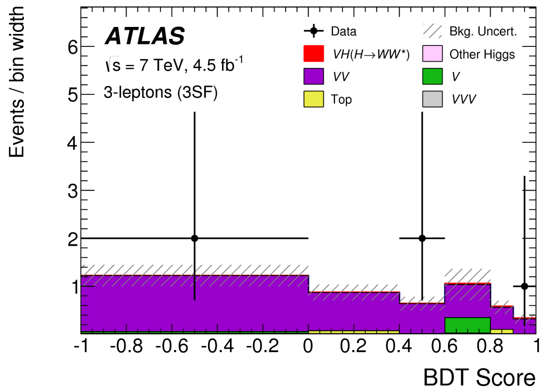

(a)

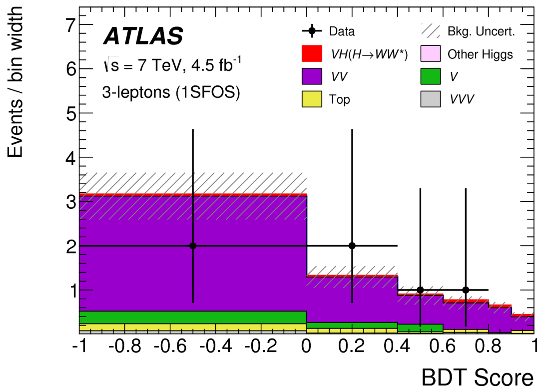

(b)

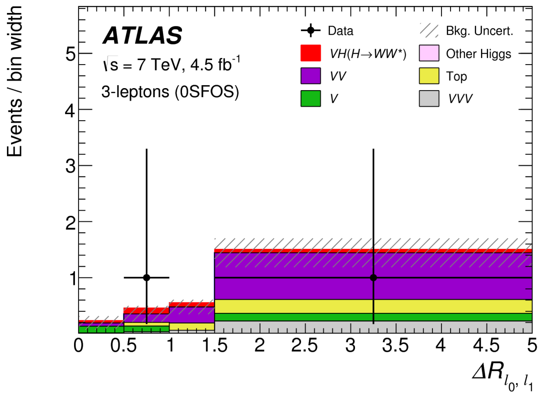

(c)

FIGURE 5.3: Distributions of relevant quantities for the 3ℓ analyses, using 7 TeV data: (a) BDT Score in 3ℓ-3SF and (b) in 3ℓ-1SFOS, and (c) the angular separation in R of the two opposite-sign leptons with smaller ΔR distance, $\Delta R_{\ell_0\ell_1}$, in 3ℓ-0SFOS. Data (dots) are compared to the background plus $VH(H\rightarrow WW^*)$ (m_H=125 GeV) signal expectation (stacked filled histograms). The hatched area on the histogram represents the total uncertainty on the background estimate including the statistical and systematic uncertainties added in quadrature [71].

report exclusion limits on the related cross section for 110 GeV $< m_H <$ 200 GeV. The hypothesis of a SM Higgs boson of mass m_H is excluded at 95% C.L. if the value $\mu = 1$ is excluded for that mass. Fig. 5.6 presents the 95% upper limits on μ as a function of the Higgs boson mass hypothesis for the WH and ZH production modes and their combination, VH. When extracting the upper limit on WH production the ZH contribution is treated as a background and measured in the ZH optimised categories. The opposite applies to the extraction of the limit on the ZH production, where WH is considered as a background. In absence of the signal, the analysis is expected to exclude the VH production of a SM Higgs boson in the range 142 GeV $< m_H <$ 174 GeV while, due to the observation of an excess of events, no mass range is excluded. The expectation in case a Higgs boson of mass $m_H = 125.36$ GeV is present in the data is also shown to check the consistency between this result and the already observed boson.

Category	Signal significance Z_0 Exp. Z_0	Obs. Z_0	Observed signal strength μ μ	Tot. err. +	Tot. err. −	Syst. err. +	Syst. err. −
4ℓ	0.41	1.9	**4.9**	4.6	3.1	1.1	0.40
2SFOS	0.19	0	**−5.9**	6.8	4.1	0.33	0.72
1SFOS	0.36	2.5	**9.6**	8.1	5.4	2.1	0.64
3ℓ	0.79	0.66	**0.72**	1.3	1.1	0.40	0.29
1SFOS and 3SF	0.41	0	**−2.9**	2.7	2.1	1.2	0.92
0SFOS	0.68	1.2	**1.7**	1.9	1.4	0.51	0.29
2ℓ	0.59	2.1	**3.7**	1.9	1.5	1.1	1.1
DFOS	0.54	1.2	**2.2**	2.0	1.9	1.0	1.1
SS2jet	0.17	1.4	**7.6**	6.0	5.4	3.2	3.2
SS1jet	0.27	2.3	**8.4**	4.3	3.8	2.3	2.0

FIGURE 5.4: Signal significance Z_0, and the $H \to WW^*$ signal strength μ evaluated in the signal regions, combining 8 TeV and 7 TeV data. The expected (exp.) and observed (obs.) values are shown. The two plots represent the observed significance and the observed μ. In the μ plot the statistical uncertainty (stat.) is represented by the thick line, the total uncertainty (tot.) by the thin line. All values are computed for a Higgs boson mass of 125.36 GeV [71].

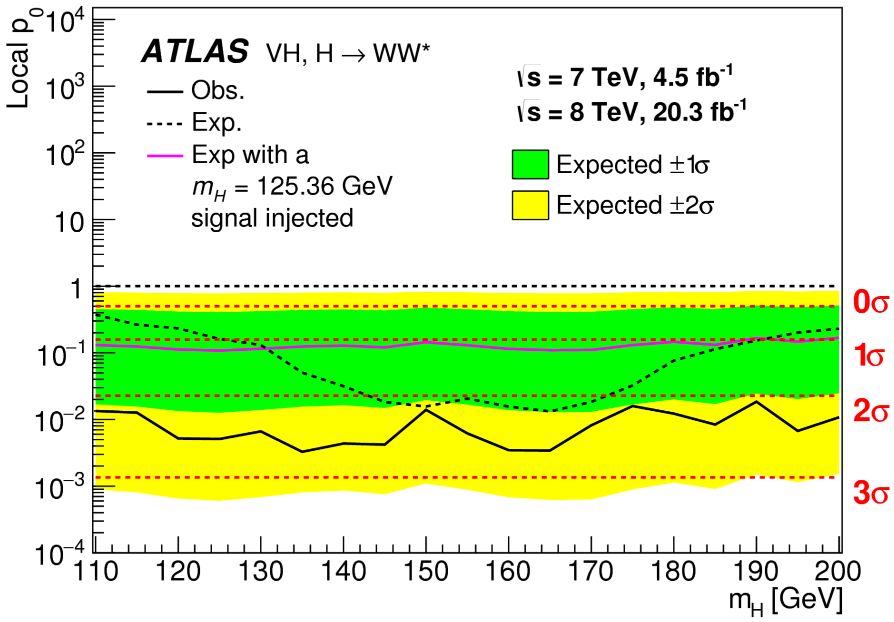

FIGURE 5.5: Search for Higgs boson production in association with a W or a Z boson in the $H \to WW^*$ decay. The observed values are shown as a solid line. The dashed line shows the expected values given the presence of a signal at each x-axis value. The expected values for $m_H = 125.36$ GeV (signal injected) are given by a purple line [71].

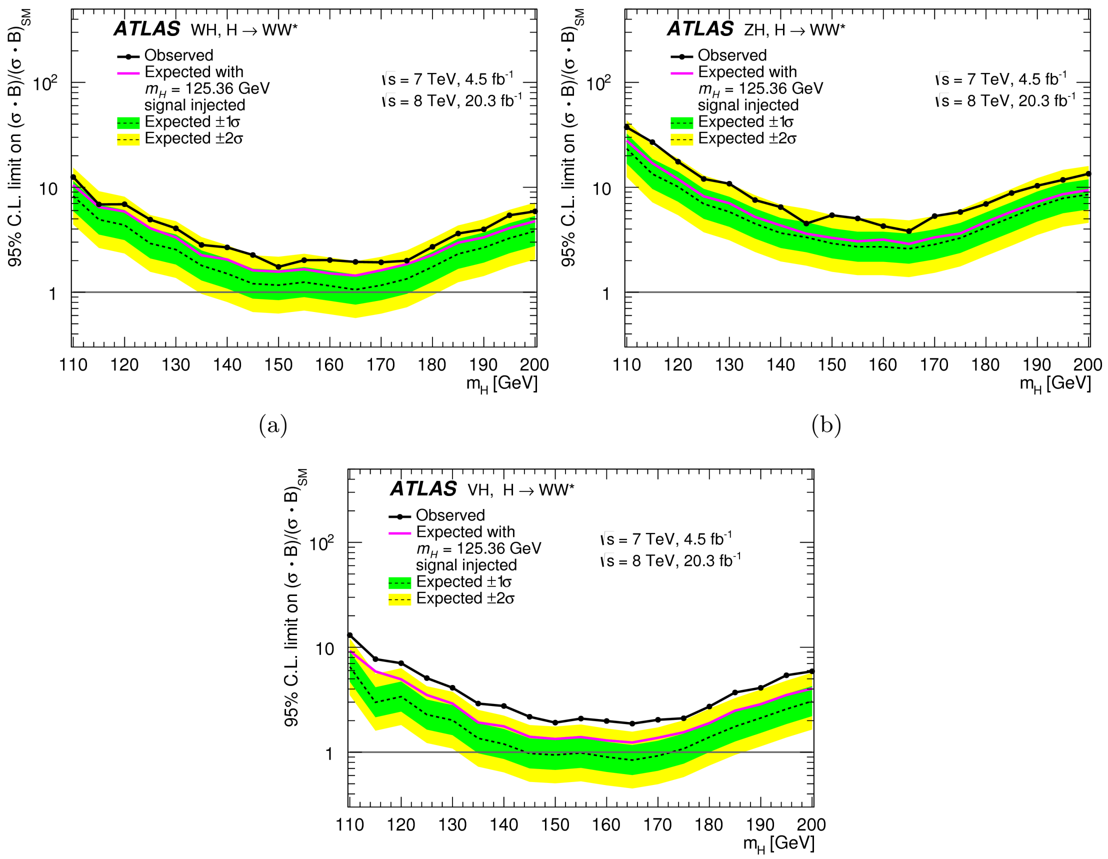

(a) (b) (c)

FIGURE 5.6: The CLs exclusion for the SM production of a Higgs boson with mass in the range $110-200$ GeV: the expected and observed exclusion is shown for (a) the WH production, (b) the ZH production, and (c) their combination VH. The continuous lines represent the observation and the dashed lines the expectation for an Higgs boson at that mass. The inner shaded band represents the $\pm1\sigma$ uncertainty on the expected values, and the larger shaded band represents the $\pm2\sigma$ uncertainty. The purple line is the expectation curve in case a Higgs boson of mass $m_H = 125.36$ GeV is present in the data.

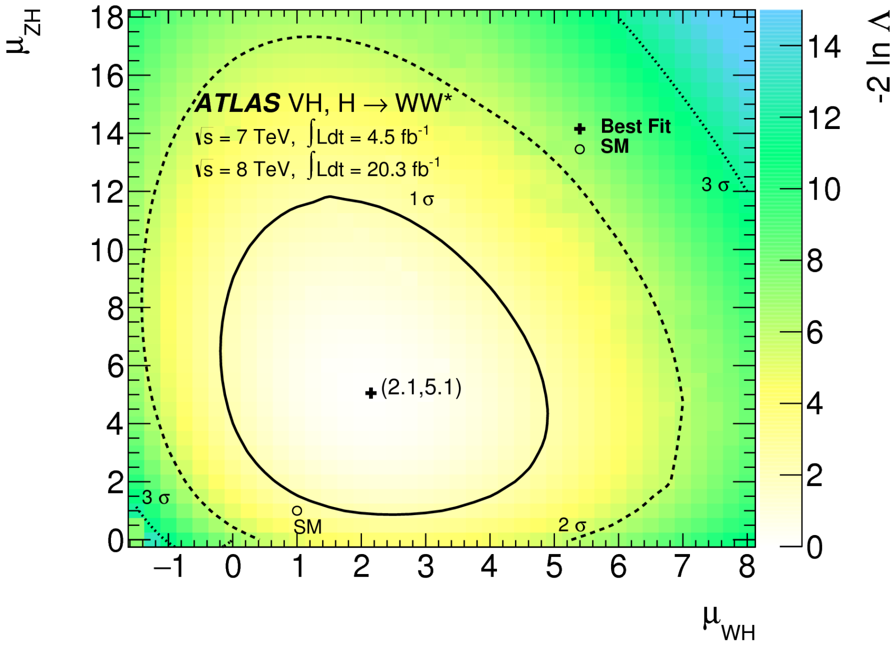

FIGURE 5.7: The value of the test statistic as a function of μ_{WH} and μ_{ZH}, for m_H = 125.36 GeV. The contours correspond to the values of (μ_{WH}, μ_{ZH}) associated with the 68%, 90% and 95% confidence levels. The black cross indicates the best fit to the data and the open circle represents the SM expectation $(\mu_{WH}$, $\mu_{ZH})$=(1,1) [71].

Chapter 6

What about Run-2?

First collisions at 13 TeV were observed on the evening of May 20th 2015, when LHC started its Physics Run-2. The 13 TeV centre-of-mass energy leads to higher cross sections, moreover, in order to achieve same and even better performances as in Run-1, ATLAS detector has been improved in the long shotdown before restarting.

An overview of the main differences between Run-2 and Run-1 of ATLAS and LHC will be given in this Chapter and the 13 TeV on-going analysis will be briefly introduced.

6.1 New scenario

The first and most clear characteristic in the Run-2 is the centre-of-mass energy of 13 TeV that leads to the increase of cross-sections for all processes, some are reported in Fig. 6.1. Electroweak processes present roughly an increase of a factor two, VH signal and diboson backgrounds are included among these ones. Processes involving t-quarks increase approximately by a factor three to four.

The proton bunch spacing within trains is halved from 50 ns to 25 ns, for a large fraction of the year 2015 (Fig. 6.2). The detector read-out, however, is optimised for this change, which leads to the expectation of only a small increase of out-of-time pileup.

The luminosity of $1.3 \times 10^{34}\text{cm}^{-2}\text{s}^{-1}$ with respect to $7.73 \times 10^{33}\text{cm}^{-2}\text{s}^{-1}$ in 2012, will allow to collect 100 fb^{-1} by the end of 2018. The main upgrade for the ATLAS detector is the addition of a further silicon pixel layer, IBL for Insertable B-Layer [124], 3.3 cm far from the beam and the addition of a Fast Track (FTK) trigger system. IBL is installed in the ATLAS detector between a new beam pipe with a smaller radius and the previously existing pixel detector. Due to the significantly improved impact parameter resolution,

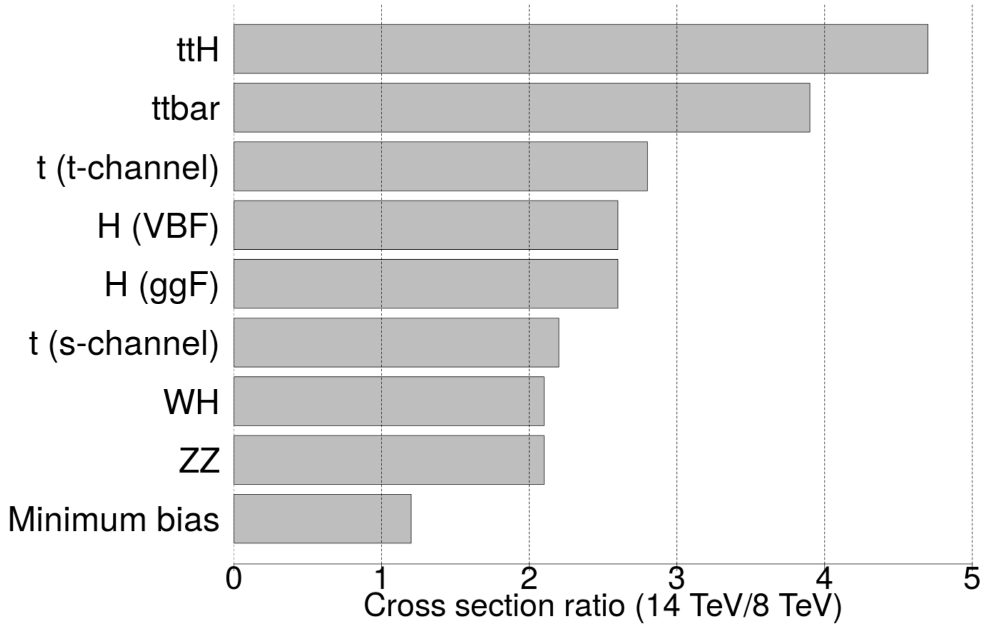

FIGURE 6.1: Cross-section increase for some processes in the Run-2 of LHC with respect to to Run-1.

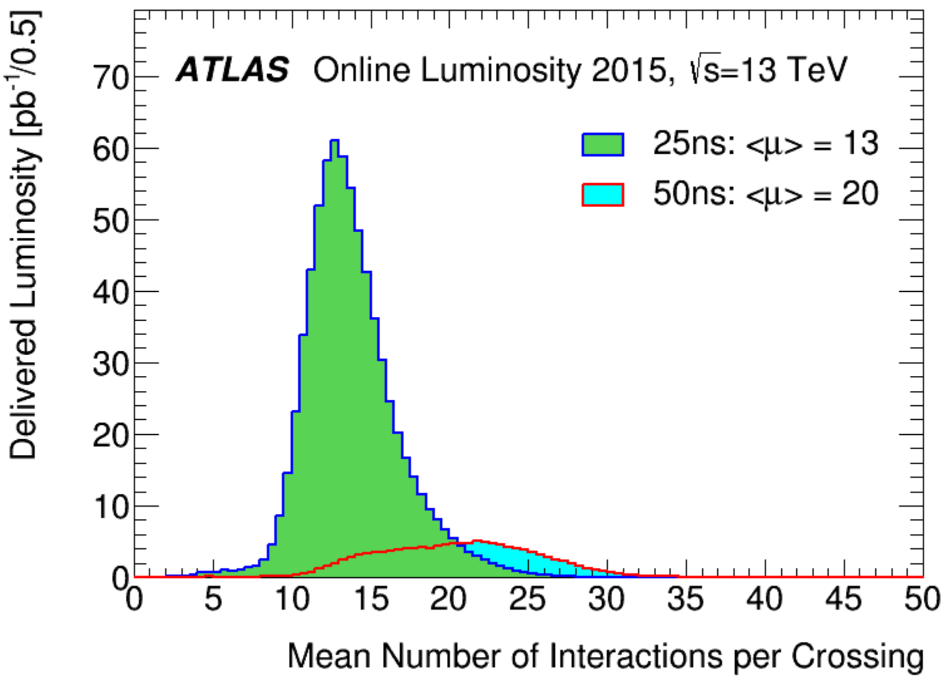

FIGURE 6.2: Luminosity-weighted distribution of the mean number of interactions per crossing for the 2015 *pp* collision data recorded from 3 June - 22 September at 13 TeV centre-of-mass energy. All data delivered to ATLAS during stable beams is shown, and the integrated luminosity and the mean mu value are given in the figure [42].

the IBL has a major impact on the b-tagging performance. In addition, the tracking and b-tagging algorithms have been revisited [125, 126]. In the track reconstruction domain one of the main changes is an improved handling of pixel hits shared between multiple tracks in the core of high transverse momentum, p_{T}, jets [127], based on a Neural Network pixel hit clustering [128]. The improvements to the b-tagging algorithms lead to a 10% relative improvement in the b-tag efficiency for same light-jet rejection.

Several algorithms have been developed to quantify MET [129]. In addition to $\mathbf{E}_{\mathrm{T}}^{\mathrm{miss}}$ and $\mathbf{p}_{\mathrm{T}}^{\mathrm{miss}}$ as in Run-1 [67, 69], a track-based soft term (TST) MET is now available and it is the primary method of MET reconstruction in Run-2. TST MET uses a track-based soft term, but combines this with calorimeter-based measurements for the hard objects. This presents a good compromise between the calorimeter- and track-based approaches, it takes into account the contribution of neutral particles in the computation and it is robust even with increased pileup.

6.2 On-going 3ℓ analysis

The Run-1 analysis is the baseline for the on-going studies, given that the analysis is in a very early stage, the whole analysis will be not described in detail but few items will be illustrated such as new relevant improvement to MC samples, a preliminary cutflow and the general behaviour of signal and backgrounds.

In the new analysis, VH hard processes are simulated with Powheg [130] and parton shower with Pythia8. This strategy will avoid the introduction of an acceptance systematics, which affected mostly the theoretical systematics of Run-1 in the 3ℓ channel (Sec.4.7).

The effect of a Run-1-like selection applied to 13 TeV MC samples is shown in Tab. 6.1, a strategy for main backgrounds normalisation and control regions has not yet been defined. As a first estimation diboson backgrounds still remain the major component in 3SF+1SFOS category, in the 0SFOS category t-quark processes exceed diboson backgrounds. Samples with higher statistics are required for processes involving a Z boson and jets, the statistical uncertainty at the end of the cutflow prevent to draw conclusions on such background.

$\sqrt{s} = 13$ TeV, $\mathcal{L} = 10 fb^{-1}$, 3ℓ	WH	WZ / $W\gamma^*$ / $W\gamma$	ZZ^*	WW	Z+jets Nominal	$t\bar{t}$	SingleTop	ggF/VBF	Total Bkg
Preselection	5.780 ± 0.050	1931 ± 18	683 ± 18	2.05 ± 0.75	815 ± 110	180.9 ± 6.4	11.82 ± 0.66	0.110 ± 0.030	3652 ± 115
SR1+SR2	4.360 ± 0.040	1924 ± 17	680 ± 18	1.54 ± 0.69	815 ± 110	139.4 ± 5.6	8.79 ± 0.57	0.050 ± 0.020	3596 ± 114
at most 1 jet	3.510 ± 0.040	1324 ± 14	513 ± 12	0.69 ± 0.46	609 ± 101	54.0 ± 3.5	5.77 ± 0.46	0.040 ± 0.020	2533 ± 104
bjetVeto	3.440 ± 0.040	1291 ± 14	494 ± 12	0.69 ± 0.46	591 ± 99	26.4 ± 2.4	4.15 ± 0.39	0.030 ± 0.020	2433 ± 102
$MET > 15$ GeV (for Training)	3.270 ± 0.040	1201 ± 14	316 ± 10	0.69 ± 0.46	413 ± 84	25.5 ± 2.4	3.87 ± 0.38	0.020 ± 0.010	1987 ± 87
$MET_{STVF} > 30$ GeV $MET_{TrkHWW;Clj} > 20$ GeV	2.830 ± 0.030	954 ± 12	145.4 ± 7.1	0.69 ± 0.36	191 ± 59	21.5 ± 2.2	3.40 ± 0.36	0.020 ± 0.010	1322 ± 61
Z Veto	2.050 ± 0.030	66.0 ± 3.3	36.4 ± 4.0	0.27 ± 0.21	56 ± 34	9.7 ± 1.5	1.89 ± 0.27	0.020 ± 0.010	175 ± 35
$M_{\ell,\ell;min} > 12$ GeV $M_{\ell,\ell;max} < 200$ GeV	1.890 ± 0.030	52.7 ± 2.9	33.7 ± 3.7	0.21 ± 0.21	53 ± 34	9.3 ± 1.4	1.67 ± 0.26	0.020 ± 0.010	156 ± 35
$\Delta R_{\ell_-,\ell_1} < 2.$	1.790 ± 0.030	40.7 ± 2.6	22.4 ± 3.1	0.21 ± 0.21	30 ± 26	7.0 ± 1.3	1.19 ± 0.21	0.020 ± 0.010	107 ± 26
Z depleted region	1.420 ± 0.020	7.9 ± 1.0	2.67 ± 0.78	0.51 ± 0.31	-	41.6 ± 3.1	3.04 ± 0.33	0.060 ± 0.020	55.6 ± 3.4
at most 1 jet	1.130 ± 0.020	5.22 ± 0.83	1.87 ± 0.57	0.51 ± 0.31	-	17.4 ± 2.0	1.60 ± 0.24	0.050 ± 0.020	26.6 ± 2.3
bJet Veto	1.100 ± 0.020	5.22 ± 0.83	1.69 ± 0.54	0.51 ± 0.31	-	6.5 ± 1.2	1.13 ± 0.20	0.050 ± 0.020	15.1 ± 1.6
$M_{\ell,\ell;min} > 6$ GeV $M_{\ell,\ell;max} < 200$ GeV	1.050 ± 0.020	4.59 ± 0.78	1.69 ± 0.54	0.30 ± 0.23	-	5.9 ± 1.1	1.10 ± 0.20	0.050 ± 0.020	13.6 ± 1.5
$\Delta R_{\ell_-,\ell_1} < 2.$	0.970 ± 0.020	2.67 ± 0.59	0.97 ± 0.41	-	-	3.61 ± 0.90	0.67 ± 0.16	0.040 ± 0.020	7.9 ± 1.2

TABLE 6.1: 13 TeV 3ℓ analysis: number of expected events for the signal and total MC at each step of the event selection similar to the one described in Tab. 4.7. Statistical errors are reported.

Chapter 7

Conclusions

In this thesis I described the analyses of data from the ATLAS detector at the LHC using the $H \to WW^*$ channel in the search for the associated production mode with a gauge boson (W or Z). Up to 4.5 fb^{-1} of data collected at centre-of-mass energy of 7 TeV and 20.3 fb^{-1} at 8 TeV are used. Four channel were studied, from two leptons in the final state up to four leptons. In each channel a selection was optimised in order to reject the main backgrounds. In the 3ℓ channel further sub-signal-regions were defined according to the number of Same Flavour Opposite Sign leptons in the final state: 0SFOS, 1SFOS, 3SF. This channel is designed to investigate the WH production in which all W bosons in the event decay to electrons or muons (plus neutrinos).

I contributed developing the Multivariate Analysis in the 3ℓ-1SFOS and 3ℓ-3SF and following its deployement from the early stages to the production of final plots that have been published [71]. In particular I defined the training from an optimisation study where the configuration with the smallest number of variables and best separation has been chosen. The training region has been chosen as wide as possible, requiring minimal selections to preserve the MC statistics for both signal and backgrounds, in order to exploit the kinematic differences among signal and background and to avoid the overtraining of the BDT. After the definition of the analysis on the Monte Carlo simulated events, I followed all the validations of the BDT Score and of the background modelling in the CRs with data events. After this validation I finally produced the plots for the 3ℓ SRs. My own contribution, together with the other analyses and the statistical combination of all the channels, gave a complete picture of the VH associated production in the $H \to WW^*$ decay channel of the Higgs boson.

A deviation from a background-only hypotesis corresponding at 2.4σ was observed for a Higgs boson mass of $m_H = 125.36$ GeV. VH results are also included in the whole ATLAS measurement of the Higgs boson production and decay rates and coupling strengths reported in Ref. [131].

Appendix A

What is a Multivariate Analysis?

Each generation of high-energy physics experiments is grander in scale than the previous, more powerful, more complex, and more demanding in terms of data handling and analysis. The greatest challenge in these pursuits is to extract the extremely rare signals, if any, from the huge backgrounds that arise from known physics processes. The use of advanced analysis techniques is crucial in achieving this goal.
In this Appendix a brief description of the multivariate approaches will be given with particular emphasis on the Decision Trees widely used in HEP.

A.1 General overview

Classification of objects or events is, by far, the most important analysis task in HEP [132, 133, 134]. Common examples are the identification of electrons, photons, τ leptons, b-quark jets, and so on, and the discrimination of signal events from background processes. Optimal discrimination between classes is crucial to obtain signal-enhanced samples for precision physics measurements. Characterising an object or an event generally involves multiple quantities referred to as feature variables. These may be, for example, the four-vectors of particles, energy deposited in calorimeter cells, derived kinematic quantities, and global event characteristics. In general, the variables can also be correlated. To extract results with maximum precision, it is necessary to treat these variables in a fully multivariate way. The feature variables that describe an object or an event can be represented by a vector $\mathbf{x} = (x_1, x_2, ..., x_d)$ in a d-dimensional feature space. The objects or events of a particular type or class can be expected to occupy specific contiguous regions in the feature space. When correlations exist between variables, the effective dimensionality of the problem is smaller than d. Given $\mathbf{x}$, the goal is to construct a function $y = f(\mathbf{x})$ with properties that are useful for subsequent decision making and inference.

The availability of vast amounts of data, along with challenging scientific and industrial problems characterised by multiple variables, paved the way for the development of automated algorithms for learning from data. The primary goal of learning is to respond correctly to future data. In conventional statistical techniques, one starts with a mathematical model and finds parameters of the model either analytically or numerically by using some optimisation criteria. This model then provides predictions for future data. In machine learning, an approximating function is inferred automatically from the given data without requiring a priori information about the function. In machine learning, the most powerful approach to obtain the approximation $f(\mathbf{x}, \mathbf{w})$ of the unknown function $f(\mathbf{x})$ is supervised learning, in which a training data set that comprises feature vectors (inputs) and the corresponding targets (that is, desired outputs) is used. The training data set $y, \mathbf{x}$, where y are the targets [from the true function $f(\mathbf{x})$], encodes information about the input-output relationship to be learned. In HEP, the training data set generally comes from Monte Carlo simulations. The function $f(\mathbf{x})$ is usually discrete for classification, i.e. $0, 1$ or $-1, 1$ for binary classification.

In all approaches to functional approximation (or function fitting), the information loss incurred in the process has to be minimised. The information loss is quantified by a loss function, $L\{y, f(\mathbf{x}, \mathbf{w})\}$. In practice, the minimisation is more robust if one minimises the loss function averaged over the training data set. A learning algorithm, therefore, directly or indirectly,minimises the average loss (known as the risk), which is quantified by a risk function, $R(\mathbf{w})$, that measures the cost of mistakes made in the predictions and finds the best parameters $\mathbf{w}$. The empirical risk (an approximation to true risk) is defined as the average loss over all (N) predictions [132],

$$R(\mathbf{w}) = \frac{1}{N} \sum_{i=1}^{N} L\{y_i, f(\mathbf{x}_i, \mathbf{w})\}. \tag{A.1}$$

A commonly used risk function is the mean-square error,

$$R(\mathbf{w}) = E(\mathbf{w}) = \frac{1}{N} \sum_{i=1}^{N} \{y_i - f(\mathbf{x}_i, \mathbf{w})\}^2. \tag{A.2}$$

A.2 Decision Trees

Decion trees (DTs) are based on sequential cuts applied to the feature variables in order to define and classify hyper-cubes in the phase-space of parameters. At each step in the sequence, the best cut is searched for and used to split the data, and this process is continued recursively on the resulting partitions until a given terminal criterion is satisfied. The DT algorithm starts at the so-called root node (Fig. A.1), with the entire training data set containing signal and background events. At each iteration of the algorithm, and for each node, one finds the best cut for each variable and then the best cut overall. The data are split by use of the best cut (the cut that gives the largest reduction in impurity), thereby forming two branch nodes. One stops splitting when no further reduction in impurity is possible (or when the number of events is judged too small to proceed further). The measure that is commonly used to quantify impurity is the so-called Gini index [114, 132],

$$\text{Gini} = (s+b)P(1-P) = \frac{sb}{s+b}, \tag{A.3}$$

where $P = s/(s+b)$ is the signal purity, and s and b are the signal and background counts at any step in the process. To determine the increase in quality when a node is split into two branches, one maximises

$$\text{Gini}_{\text{father}} - \text{Gini}_{\text{left son}} - \text{Gini}_{\text{right son}}.$$

A common strategy is to set a criterion to terminate the splitting and, if a leaf has purity greater than 1/2 (or whatever is set), then it is called a signal leaf and if the purity is less than 1/2, it is a background leaf. Events are classified signal if they land on a signal leaf and background if they land on a background leaf. The resulting tree is a decision tree. The operative description of this method corrresponds to the minimisation of the expectation value [133]: $E(e^{-yF(\mathbf{x})})$, where y = 1 for signal, y = -1 for background, $F(\mathbf{x}) = \sum_{i=1}^{N_{trees}} f_i(\mathbf{x})$, where the classifier $f_i(\mathbf{x}) = 1$ if an event lands on a signal leaf, and $f_i(\mathbf{x}) = -1$ if an event lands on a background leaf. DTs are very popular because of the transparency of the procedure and interpretation. They have additional advantages: (a) tolerance to missing variables in the training data and test data; (b) insensitivity to irrelevant variables, given that the best variable on which to cut is chosen at each split and, therefore, ineffective ones are not used; and (c) invariance to one-to-one transformation of variables, which makes preprocessing of data unnecessary. However, DTs also have serious limitations: (a) instability with respect to the training sample (a slightly different training sample can produce a dramatically different tree); (b) suboptimal performance due to the piecewise constant nature of the model, which means that the predictions are constant within each bin (the region represented by a leaf) and discontinuous at its boundaries; and (c) poor global generalisation because the recursive splitting results in the use of fewer and fewer training data per bin and only a small fraction of the feature variables may be used to model the predictions for individual bins. Most of these limitations, fortunately, have been overcome with the use

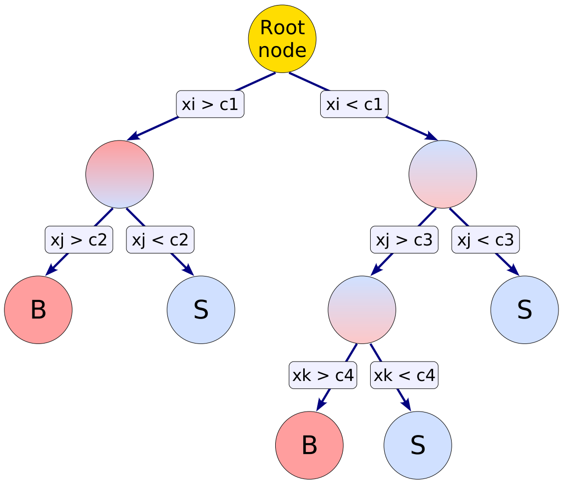

FIGURE A.1: Schematic view of a decision tree. Starting from the root node, a sequence of binary splits using the discriminating variables x_i is applied to the data. Each split uses the variable that at this node gives the best separation between signal and background when being cut on [114].

of ensemble learning techniques:

- *Boosting [133]*. The boosting algorithm is one of the most powerful learning techniques introduced during the past decade. The boosting algorithm is a procedure that combines many "weak" classifiers to achieve a final powerful classifier. Boosting can be applied to any classification method. After the creation of the first tree, if a training event is misclassified, i.e, a signal event lands on a background leaf or a background event lands on a signal leaf, then the weight of that event (w_i) is increased (boosted). A second tree is built using the new weights, no longer equal. Again misclassified events have their weights boosted and the procedure is repeated (Fig. A.2). Typically, one may build 1000 or 2000 trees this way. A score (T_m) is now assigned to an event as follows. The event is followed through each tree in turn. If it lands on a signal leaf it is given a score of 1 and if it lands on a background leaf it is given a score of -1. The renormalised sum of all the scores, possibly weighted, is the final score of the event. High scores mean the event is most likely signal and low scores that it is most likely background.
  A common boosting method is the so-called ϵ-Boost, or sometimes "shrinkage". After the mth tree, change the weight of each event i, $i = 1, ..., N$:

  $$w_i \to w_i e^{2\epsilon I(y_i \neq T_m(\mathbf{x}_i))},$$

  where ϵ is a constant of the order of 0.01 (usually referred as *shrinkage*), and $I(y_i, T_m(\mathbf{x}_i))$ is 1 if $y_i \neq T_m(\mathbf{x}_i)$ and it is 0 otherwise. Renormalise the weights,

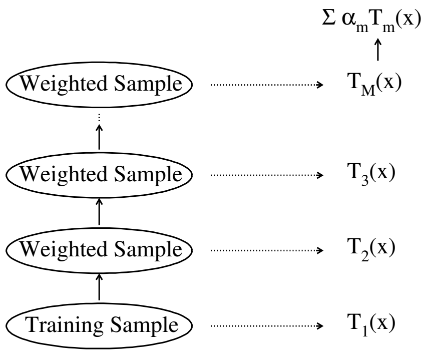

FIGURE A.2: Schematic of a boosting procedure, α_m can either depends on the mth tree or be a constant value [133].

$w_i \rightarrow w_i / \sum_{i=1}^{N} w_i$. The score for a given event is

$$T(\mathbf{x}) = \frac{1}{N_{tree}} \sum_{m=1}^{N_{tree}} \epsilon T_m(\mathbf{x}), \tag{A.4}$$

which is the renormalised, but unweighted, sum of the scores over individual trees[1].

- *Bagging.* Bagging (bootstrap aggregating) is a simple average of the outputs of M predictors, usually classifiers, where each is trained on a different bootstrap sample (i.e., a randomly selected subset) drawn from a training sample of N events. In Eq. A.4, α_m needs to take into account an additional $1/M$ in the case of bagging.
- *Random Forest.* Many classifiers are trained, each with a randomly chosen subset of feature variables at each split providing a random forest of DTs. The output for each event is the average output of all trees in the random forest. Further randomisation can be introduced through the use of bootstrap samples as in the case of bagging.

[1]In a more general definition $\epsilon \rightarrow \alpha_m$ where α can be a non constant value.

Appendix B

Checks on the 3ℓ-MVA analysis

The modelling of BDT Score is fundamental in the shape analysis, in this Appendix further checks on the BDT Score shape are shown.

B.1 Normalisation of the main background

The main background in the 3ℓ-MVA analysis is $WZ/W\gamma^*$. As explained in Sec. 4.5, a dedicated control region is defined and included in the final fit (Sec. 5.2) in order to gain information on the normalisation of such background. The NF should be in principle an intrinsec property of the of the Monte Carlo generator relative to the phase-space in which MC is used and in particular the NF should be indipendent of the BDT Score.
In Tab. B.1 the NF computed in different sub-phase-spaces according to the BDT Score is shown, the values are compatible within the errors.

BDT region	WZ SF
BDT $\in$ [-1.0;1.0]	1.09 $\pm$ 0.07
BDT $\in$ [-1.0;-0.8]	1.0 $\pm$ 0.07
BDT $\in$ [-0.8;1.0]	0.97$\pm$ 0.12
BDT $\in$ [-0.5;1.0]	0.92$\pm$ 0.2
BDT $\in$ [0.0;1.0]	0.92$\pm$ 0.3

Table B.1: Normalisation factor for the $WZ/W\gamma^*$ background in different BDT Score regions.

B.2 BDT Score distributions along the cutflow

The BDT Score modelling is also checked in a wider phase-space than the one considered for the shape analysis. The effects of cuts applied to select the final signal region are shown in Fig. B.1 and Fig. B.2. The overall agreement is guaranteed by the goodness of Kolmogorv-Smirnov test whose probability is shown above each plot.

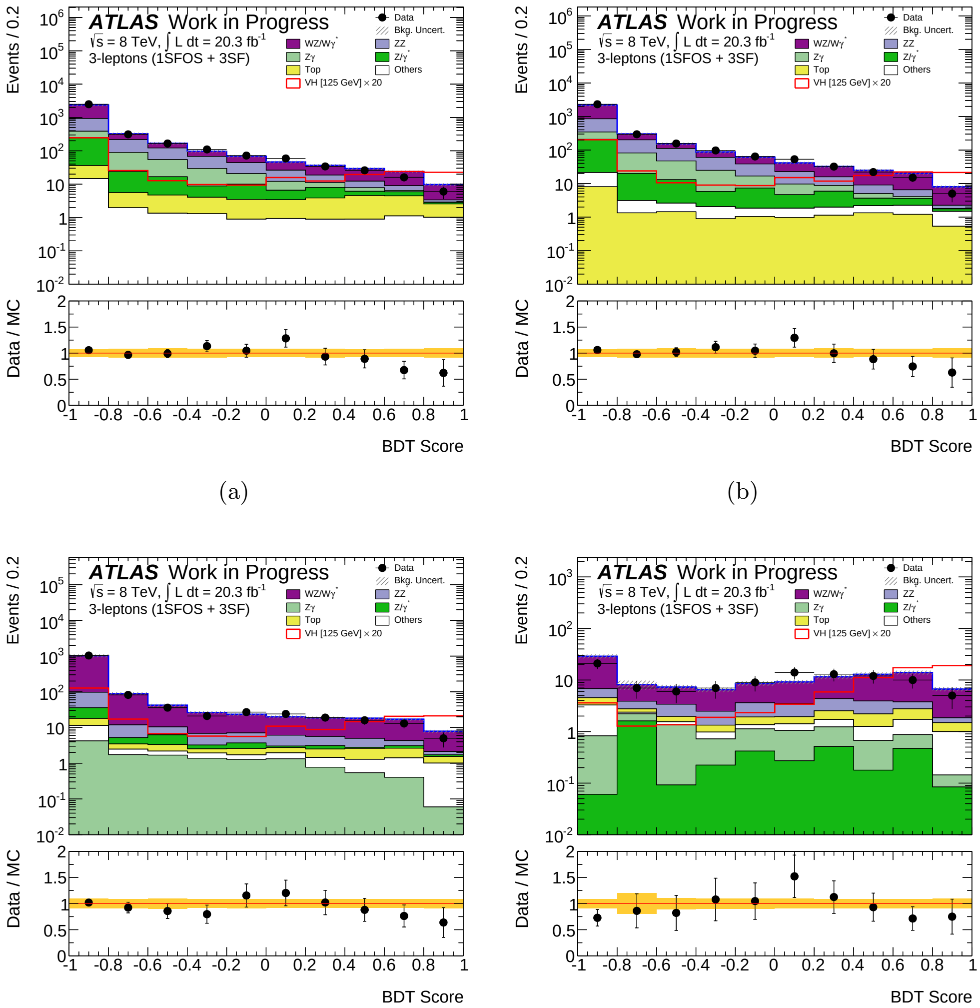

(a) (b)

(c) (d)

FIGURE B.1: Distributions of BDT Score variable: (a) after requiring at most 1 jet, (b) after top-veto, (c) after MET selection, (d) after Z-mass veto. Data (dots) are compared to the background + signal (m_H=125 GeV) expectation from simulation (stacked filled histograms), where the background components are normalised by applying the NFs derived from the final fit. The Data/MC ratio does not include the contribution from the expected signal (m_H=125 GeV).

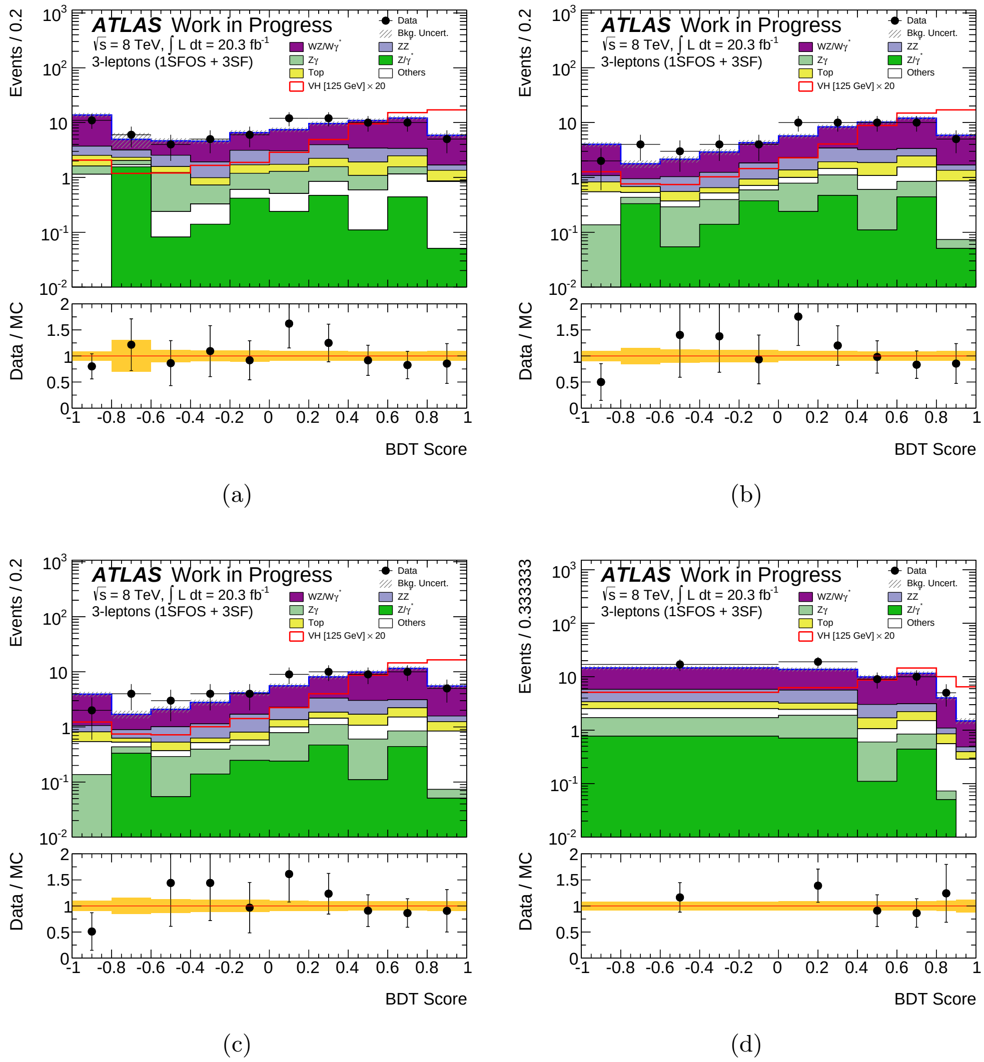

FIGURE B.2: Distributions of BDT Score variable: (a) after min/max Mll cut, (b) after $\Delta R_{\ell_0\ell_1}$ cut, (c) after "SS-leptons OR" and "$\ell\nu\ell\nu$ OR", (d) after "SS-leptons OR" and "$\ell\nu\ell\nu$ OR" with the binning used for the shape analysis. Data (dots) are compared to the background + signal (m_H=125 GeV) expectation from simulation (stacked filled histograms), where the background components are normalised by applying the NFs derived from the final fit. The Data/MC ratio does not include the contribution from the expected signal (m_H=125 GeV).

Acronyms

ATLAS	**A** **T**oroidal **L**HC **A**pparatu**S**
BDT	**B**oosted **D**ecision **T**rees
BSM	**B**eyond the **S**tandard **M**odel
CERN	**C**onseil **E**uropéen pour la **R**echerche **N**ucléaire
CMS	**C**ompact **M**uon **S**olenoid
CL	**Confidence** **L**evel
CR	**C**ontrol **R**egion
CSC	**C**athode **S**trip **C**hambers
DFOS	**D**ifferent **F**lavour **O**pposite **S**ign
DT	**D**ecision **T**ree
EMCal	**E**lectro**M**agnetic **Cal**orimeter
EW	**E**lectro**W**eak
FCal	**F**orward **Cal**orimeter
FTK	**F**ast **T**rac**K**
FSR	**F**inal **S**tate **R**adiation
ggF	**g**luon-**g**luon **F**usion
GSF	**G**aussian-**S**um **F**ilters
HCal	**H**adronic **Cal**orimeter
HEC	**H**adronic **E**nd-cap **C**alorimeter
HEP	**H**igh **E**nergy **P**hysics
IBL	**I**nsertable **B**-**L**ayer
ID	**I**nner **D**etector
JER	**J**et **E**nergy **R**esolution
JES	**J**et **E**nergy **S**cale
JVF	**J**et **V**ertex **F**raction

KS	**K**olmogorov-**S**mirnov
LAr	**L**iquid **Ar**gon
LEP	**L**arge **E**lectron-**P**ositron
LHC	**L**arge **H**adron **C**ollider
MDT	**M**onitored **D**rift **T**ubes
MET	**M**issing **E**nergy **T**ransverse
MLE	**M**aximum-**L**ikelihood **E**stimator
MS	**M**uon **S**ystem
MVA	**M**ulti**V**ariate **A**nalysis
NF	**N**ormalisation **F**actor
NLO	**N**ext-to **L**eading **O**rder
NNLL	**N**ext-to-**N**ext-to **L**eading **L**ogarithm
NNLO	**N**ext-to-**N**ext-to **L**eading **O**rder
NP	**N**uisance **P**arametr
OS	**O**pposite **S**ign
PDF	**P**arton **D**ensity **F**unction
POI	**P**arameter **O**f **I**nterest
PS	**P**arton **S**howering
	or **P**roton **S**ynchrotron
PSB	**P**roton **S**ynchrotron **B**ooster
QCD	**Q**uantum **C**hromo**D**ynamics
QED	**Q**uantum **E**lectro**D**ynamics
RMS	**R**oot **M**ean **S**quare
RoI	**R**egion **o**f **I**nterest
RPC	**R**esistive **P**late **C**hambers
SCT	**S**emi**C**onductor **T**racker
SFOS	**S**ame **F**lavour **O**pposite **S**ign
STVF	**S**oft **T**erm **V**ertex **F**raction
SM	**S**tandard **M**odel
SPS	**S**uper **P**roton **S**ynchrotron
SR	**S**ignal **R**egion
SS	**S**ame **S**ign
TGC	**T**hin **G**ap **C**hambers

TST **T**rack-based **S**oft **T**erm

TMVA **T**oolkit **M**ulti**V**ariate Data **A**nalysis

TRT **T**ransition **R**adiation **T**racker

VBF **V**ector **B**oson **F**usion

VEV **V**acuum **E**xpectation **V**alue

List of Figures

List of Tables

Bibliography

[1] F. Halzen and A. D. Martin, *Quarks and Leptons: An Introductory Course in Modern Particle Physics*. Wiley, 1st ed., 1984. Cited at pages 1, 10.

[2] W. Hollik, *Quantum field theory and the Standard Model*, [arXiv:1012.3883]. Cited at pages 1, 4, 11.

[3] G. Altarelli, *Collider Physics within the Standard Model: a Primer*, [arXiv:1303.2842]. Cited at pages 1, 4, 18.

[4] K. A. Olive et al., *(particle data group)*, *Chin. Phys.* **C38** (090001 (2014)). Cited at pages 3, 11, 12, 31.

[5] J. Bronner, *Measurement of Higgs Boson Production via Vector Boson Fusion in Decays into W Bosons with the ATLAS Detector*, CERN-THESIS-2014-031. Cited at page 3.

[6] D. V. S. Michael E. Peskin, *An introduction to quantum field theory*. Frontiers in Physics. Addison-Wesley Pub. Co, 1995. Cited at page 2.

[7] J. D. Jackson, *Classical Electrodynamics Third Edition*. Wiley, 3 ed., 1998. Cited at page 3.

[8] G. Altarelli, *A QCD primer*, [hep-ph/0204179]. Cited at page 4.

[9] D. H. Perkins, *Introduction to High Energy Physics*. Cambridge University Press, 4th ed., 2000. Cited at page 4.

[10] R. D. Ball et al., *Parton distributions with LHC data*, *Nuc. Phys. B* **867** (2013), no. 2 244 – 289. Cited at pages 5, 89.

[11] "Web Page: Neural Network Parton Distribution Functions." http://nnpdf.hepforge.org/. Cited at page 5.

[12] U. Amaldi et al., *A Comprehensive Analysis of Data Pertaining to the Weak Neutral Current and the Intermediate Vector Boson Masses*, *Phys. Rev.* **D36** (1987) 1385. Cited at page 6.

[13] F. Englert and R. Brout, *Broken symmetry and the mass of gauge vector mesons*, *Phys. Rev. Lett.* **13** (1964) 321–323. Cited at page 6.

[14] P. W. Higgs, *Broken symmetries and the masses of gauge bosons*, *Phys. Rev. Lett.* **13** (1964) 508–509. Cited at page 6.

[15] P. W. Higgs, *Spontaneous symmetry breakdown without massless bosons*, *Phys. Rev.* **145** (May, 1966) 1156–1163. Cited at page 6.

[16] G. Guralnik, C. Hagen, and T. Kibble, *Global conservation laws and massless particles*, *Phys. Rev. Lett.* **13** (1964) 585–587. Cited at page 6.

[17] G. Altarelli et al., *Elementary Particles, Subvolume A - Theory and Experiments*. Springer, 1 ed., 2008. Cited at pages 6, 10.

[18] J. D. Bjorken and S. D. Drell, *Relativistic quantum fields*. Mcgraw-Hill College, first edition ed., 1965. Cited at page 7.

[19] CMS Collaboration, *The Discovery of the Higgs Boson with the CMS Detector and its Implications for Supersymmetry and Cosmology*, [`arXiv:1309.0721`]. Cited at page 9.

[20] S. Heinemeyer et al., *Handbook of LHC Higgs Cross Sections: 3. Higgs Properties*, [`arXiv:1307.1347`]. Cited at pages 12, 14, 15, 41, 48, 85.

[21] "Web Page: LHC Higgs Cross Section WG Picture Gallery." `https://twiki.cern.ch/twiki/bin/view/LHCPhysics/LHCHXSWGCrossSectionsFigures`. Cited at pages 12, 14, 15.

[22] D. Ghosh, R. Godbole, M. Guchait, K. Mohan, and D. Sengupta, *Looking for an Invisible Higgs Signal at the LHC*, *Phys. Lett.* **B725** (2013) 344–351, [`arXiv:1211.7015`]. Cited at page 13.

[23] B. W. Lee, C. Quigg, and H. B. Thacker, *Weak interactions at very high energies: The role of the higgs-boson mass*, *Phys. Rev. D* **16** (Sep, 1977) 1519–1531. Cited at page 14.

[24] LEP Working Group for Higgs boson searches, *Search for the standard model Higgs boson at LEP*, *Phys. Lett.* **B565** (2003) 61–75, [hep-ex/0306033]. Cited at pages 14, 17.

[25] G. K. Gordon Kane, *Perspectives on LHC physics*. World Scientific, 2008. Cited at page 16.

[26] Tevatron New Physics Higgs Working Group, CDF Collaboration, D0 Collaboration, *Updated Combination of CDF and D0 Searches for Standard Model Higgs Boson Production with up to 10.0 fb^{-1} of Data*, [arXiv:1207.0449]. Cited at page 17.

[27] ATLAS Collaboration, *Observation of a new particle in the search for the Standard Model Higgs boson with the ATLAS detector at the LHC*, *Phys. Lett.* **B716** (2012) 1–29, [arXiv:1207.7214]. Cited at pages 17, 18.

[28] CMS Collaboration, *Observation of a new boson at a mass of 125 GeV with the CMS experiment at the LHC*, *Phys. Lett.* **B716** (2012) 30–61, [arXiv:1207.7235]. Cited at pages 17, 18.

[29] ATLAS and CMS Collaborations, *Combined Measurement of the Higgs Boson Mass in pp Collisions at $\sqrt{s} = 7$ and 8 TeV with the ATLAS and CMS Experiments*, *Phys. Rev. Lett.* **114** (2015) 191803, [arXiv:1503.07589]. Cited at page 18.

[30] M. E. Peskin, *On the Trail of the Higgs Boson*, [arXiv:1506.08185]. Cited at page 18.

[31] J. Rosner, M. Bardeen, W. Barletta, L. Bauerdick, R. Bernstein, et al., *Planning the Future of U.S. Particle Physics (Snowmass 2013): Chapter 1: Summary*, [arXiv:1401.6075]. Cited at page 18.

[32] ATLAS Collaboration, *The ATLAS Experiment at the CERN Large Hadron Collider*, *Journal of Instrumentation* **3** (2008), no. 08 S08003. Cited at pages 21, 25, 26, 29, 31, 32.

[33] CMS Collaboration, *The CMS experiment at the CERN LHC*, *Journal of Instrumentation* **3** (2008), no. 08 S08004. Cited at page 21.

[34] ALICE Collaboration, *The ALICE experiment at the CERN LHC*, *Journal of Instrumentation* **3** (2008), no. 08 S08002. Cited at page 21.

[35] LHCb Collaboration, *The LHCb Detector at the LHC*, *Journal of Instrumentation* **3** (2008), no. 08 S08005. Cited at page 21.

[36] L. Evans and P. Bryant, *LHC Machine*, *Journal of Instrumentation* **3** (2008), no. 08 S08001. Cited at pages 21, 22.

[37] H. Wiedemann, *Particle Accelerator Physics*. Springer, 3rd ed., 2007. Cited at page 22.

[38] LHC Study Group, *The Large Hadron Collider: conceptual design*, Tech. Rep. CERN-AC-95-05-LHC, CERN, Geneva, Oct, 1995. Cited at page 22.

[39] "Web Page: TE-EPC-LPC in LHC." `http://te-epc-lpc.web.cern.ch/te-epc-lpc/machines/lhc/general.stm`. Cited at page 22.

[40] J. D. Long, *Observation and Measurements of the Higgs Boson with the* $H \to WW^{(*)} \to \ell\nu\ell\nu$ *Decay*, CERN-THESIS-2015-046. Cited at pages 23, 125.

[41] "Web Page: ATLAS Data Summary." `https://atlas.web.cern.ch/Atlas/GROUPS/DATAPREPARATION/DataSummary/`. Cited at page 24.

[42] "Web Page: LuminosityPublicResults." `https://twiki.cern.ch/twiki/bin/view/AtlasPublic/LuminosityPublicResults`. Cited at pages 24, 25, 107.

[43] ATLAS Collaboration, *Expected Performance of the ATLAS Experiment - Detector, Trigger and Physics*, [`arXiv:0901.0512`]. Cited at pages 25, 36.

[44] "Web Page: ATLAS Experiment - Photos." `http://www.atlas.ch/photos/index.html`. Cited at pages 26, 27, 28, 30, 32.

[45] ATLAS Collaboration, *ATLAS inner detector: Technical Design Report, 1*. Technical Design Report ATLAS. CERN, Geneva, 1997. Cited at page 25.

[46] ATLAS Collaboration, *ATLAS inner detector: Technical Design Report, 2*. Technical Design Report ATLAS. CERN, Geneva, 1997. Cited at page 25.

[47] ATLAS Collaboration, *ATLAS calorimeter performance: Technical Design Report*. Technical Design Report ATLAS. CERN, Geneva, 1996. Cited at page 27.

[48] ATLAS Collaboration, *ATLAS muon spectrometer: Technical Design Report*. Technical Design Report ATLAS. CERN, Geneva, 1997. Cited at page 30.

[49] T. Argyropoulos et al., *Cathode strip chambers in ATLAS: Installation, commissioning and in situ performance*, *IEEE Trans. Nucl. Sci.* **56** (2009) 1568–1574. Cited at page 31.

[50] G. Cattani and the RPC group, *The resistive plate chambers of the atlas experiment: performance studies*, *Journal of Physics: Conference Series* **280** (2011), no. 1 012001. Cited at page 31.

[51] K. Nagai, *Thin gap chambers in ATLAS*, *Nucl. Instrum. Meth.* **A384** (1996) 219–221. Cited at page 31.

[52] "Web Page: Standard Model Results ." `https://twiki.cern.ch/twiki/bin/view/AtlasPublic/StandardModelPublicResults`. Cited at page 33.

[53] ATLAS Collaboration, *Performance of the ATLAS Trigger System in 2010*, *Eur.Phys.J.* **C72** (2012) 1849 CERN-PH-EP-2011-078, [`arXiv:1110.1530`]. Cited at page 35.

[54] R. Fruhwirth, *Application of Kalman filtering to track and vertex fitting*, *Nucl.Instrum.Meth.* **A262** (1987) 444–450 HEPHY-PUB-87-503. Cited at page 36.

[55] ATLAS Collaboration, *Electron bremsstrahlung recovery in ATLAS*, *Nucl.Phys.Proc.Suppl.* **172** (2007) 208–211. Cited at page 36.

[56] R. Fruhwirth, *Track fitting with nonGaussian noise*, *Comput.Phys.Commun.* **100** (1997) 1–16 HEPHY-PUB-658-96. Cited at page 36.

[57] R. Frühwirth and A. Strandlie, *Track fitting with ambiguities and noise: A study of elastic tracking and nonlinear filters*, *Comput.Phys.Commun.* **120** (1999), no. 2-3 197–214. Cited at page 36.

[58] ATLAS Collaboration, *Measurement of the muon reconstruction performance of the ATLAS detector using 2011 and 2012 LHC proton–proton collision data*, *Eur. Phys. J.* **C74** (2014), no. 11 3130, [arXiv:1407.3935]. Cited at page 37.

[59] ATLAS Collaboration, *Electron reconstruction and identification efficiency measurements with the ATLAS detector using the 2011 LHC proton-proton collision data*, *Eur. Phys. J.* **C74** (2014), no. 7 2941, [arXiv:1404.2240]. Cited at page 37.

[60] ATLAS Collaboration, *Electron efficiency measurements with the ATLAS detector using the 2012 LHC proton-proton collision data*, ATLAS-CONF-2014-032. Cited at page 37.

[61] ATLAS Collaboration, *Observation and measurement of Higgs boson decays to WW^* with the ATLAS detector*, [arXiv:1412.2641]. Cited at pages 38, 41, 45, 47, 53, 84, 97.

[62] ATLAS Collaboration, *Properties of Jets and Inputs to Jet Reconstruction and Calibration with the ATLAS Detector Using Proton-Proton Collisions at $\sqrt{s} = 7$ TeV*, ATLAS-CONF-2010-053. Cited at page 38.

[63] M. Cacciari, G. P. Salam, and G. Soyez, *The anti-k_t jet clustering algorithm*, *JHEP* **0804** (2008) 063. Cited at page 38.

[64] ATLAS Collaboration, *Commissioning of the ATLAS high-performance b-tagging algorithms in the 7 TeV collision data*, ATLAS-CONF-2011-102. Cited at page 38.

[65] ATLAS Collaboration, *Calibration of the b-tagging efficiency for c jets with the ATLAS detector using events with a W boson produced in association with a single c quark*, ATLAS-CONF-2013-109. Cited at page 38.

[66] ATLAS Collaboration, *Calibration of the performance of b-tagging for c and light-flavour jets in the 2012 ATLAS data*, ATLAS-CONF-2014-046. Cited at page 38.

[67] ATLAS Collaboration, *Performance of Missing Transverse Momentum Reconstruction in Proton-Proton Collisions at 7 TeV with ATLAS*, *Eur. Phys. J.* **C72** (2012) 1844. Cited at pages 39, 87, 108.

[68] ATLAS Collaboration, *Performance of Missing Transverse Momentum Reconstruction in ATLAS studied in Proton-Proton Collisions recorded in 2012 at 8 TeV*, Tech. Rep. ATLAS-CONF-2013-082, CERN, Geneva, Aug, 2013. Cited at page 39.

[69] ATLAS Collaboration, *Pile-up Suppression in Missing Transverse Momentum Reconstruction in the ATLAS Experiment in Proton-Proton Collisions at sqrts = 8 TeV*, ATLAS-CONF-2014-019. Cited at pages 39, 108.

[70] ATLAS Collaboration, *Measurement of the missing transverse momentum based on tracks in proton-proton collisions at sqrt(s) = 900 GeV centre-of-mass energy with the ATLAS detector*, ATLAS-CONF-2010-020. Cited at page 39.

[71] ATLAS Collaboration, *Study of $(W/Z)H$ production and Higgs boson couplings using $H \to WW^*$ decays with the ATLAS detector*, [arXiv:1506.06641v1]. Cited at pages 42, 49, 50, 52, 63, 64, 67, 78, 85, 88, 95, 96, 100, 101, 102, 103, 105, 110, 125.

[72] A. Elagin, P. Murat, A. Pranko, and A. Safonov, *A New Mass Reconstruction Technique for Resonances Decaying to di-tau*, *Nucl.Instrum.Meth.* **A654** (2011) 481–489, [arXiv:1012.4686]. Cited at page 45.

[73] ATLAS Collaboration, *Search for the Standard Model Higgs boson in the decay channel $H \to ZZ(*) \to 4\ell$ with 4.8 fb^{-1} of pp collision data at $\sqrt{s} = 7$ TeV with ATLAS*, *Phys. Lett.* **B710** (2012) 383–402. Cited at page 46.

[74] ATLAS Collaboration, *Measurements of the properties of the Higgs-like boson in the four lepton decay channel with the ATLAS detector using 25 fb^{-1} of proton-proton collision data*, ATLAS-CONF-2013-013. Cited at page 46.

[75] T. Sjostrand, S. Mrenna, and P. Z. Skands, *A Brief Introduction to PYTHIA 8.1*, *Comput. Phys. Commun.* **178** (2008) 852–867. Cited at pages 48, 50.

[76] S. Dittmaier et al., *Handbook of LHC Higgs Cross Sections: 1. Inclusive Observables*, [arXiv:1101.0593]. Cited at pages 48, 85.

[77] S. Dittmaier, S. Dittmaier, C. Mariotti, G. Passarino, R. Tanaka, et al., *Handbook of LHC Higgs Cross Sections: 2. Differential Distributions*, [arXiv:1201.3084]. Cited at pages 48, 85.

[78] M. Ciccolini, S. Dittmaier, and M. Kramer, *Electroweak radiative corrections to associated WH and ZH production at hadron colliders*, *Phys. Rev.* **D68** (2003) 073003. Cited at page 48.

[79] O. Brein, A. Djouadi, and R. Harlander, *NNLO QCD corrections to the Higgs-strahlung processes at hadron colliders*, *Phys. Lett.* **B579** (2004) 149–156. Cited at page 48.

[80] A. Djouadi, J. Kalinowski, and M. Spira, *HDECAY: A Program for Higgs boson decays in the standard model and its supersymmetric extension*, *Comput. Phys. Commun.* **108** (1998) 56–74. Cited at page 48.

[81] M. L. Mangano et al., *ALPGEN, a generator for hard multi-parton processes in hadronic collisions*, *JHEP* **0307** (2003) 001. Cited at pages 48, 50.

[82] G. Corcella et al., *HERWIG 6: An event generator for hadron emission reactions with interfering gluons (including super-symmetric processes)*, *JHEP* **0101** (2001) 010. Cited at pages 48, 50.

[83] J. Alwall et al., *Comparative study of various algorithms for the merging of parton showers and matrix elements in hadronic collisions*, *Eur. Phys. J.* **C53** (2008) 473. Cited at page 48.

[84] T. Gleisberg et al., *Event generation with SHERPA 1.1*, *JHEP* **0902** (2009) 007. Cited at pages 48, 50.

[85] N. Kidonakis, *NNLL threshold resummation for top-pair and single-top production*, *Phys. Part. Nucl.* **45** (2014), no. 4 714–722, [arXiv:1210.7813]. Cited at page 48.

[86] P. Nason, *Recent Developments in POWHEG*, *PoS* **RADCOR2009** (2010) 018, [arXiv:1001.2747]. Cited at page 48.

[87] B. P. Kersevan and E. Richter-Was, *The Monte Carlo event generator AcerMC version 2.0 with interfaces to PYTHIA 6.2 and HERWIG 6.5*, [0405247]. Cited at pages 48, 50.

[88] J. Alwall et al., *MadGraph/MadEvent v4: The new web generation*, *JHEP* **0709** (2007) 028. Cited at page 48.

[89] J. Alwall, M. Herquet, F. Maltoni, O. Mattelaer, and T. Stelzer, *MadGraph 5: Going Beyond*, *JHEP* **1106** (2011) 128. Cited at pages 48, 50.

[90] P. Z. Skands, *Tuning Monte Carlo Generators: The Perugia Tunes*, *Phys. Rev.* **D82** (2010) 074018, [arXiv:1005.3457]. Cited at page 48.

[91] T. Binoth, M. Ciccolini, N. Kauer, and M. Kramer, *Gluon-induced W-boson pair production at the LHC*, *JHEP* **0612** (2006) 046. Cited at pages 48, 50.

[92] R. C. Gray, C. Kilic, M. Park, S. Somalwar, and S. Thomas, *Backgrounds To Higgs boson searches from $W\gamma^* \to l\nu l(l)$ asymmetric internal conversion*, [arXiv:1110.1368]. Cited at page 48.

[93] T. Binoth, N. Kauer, and P. Mertsch, *Gluon-induced QCD corrections to $pp \to ZZ \to \ell\bar{\ell}\ell'\overline{\ell'}$* , [arXiv:0807.0024]. Cited at pages 48, 50.

[94] J. M. Butterworth, J. R. Forshaw, and M. H. Seymour, *Multiparton interactions in photoproduction at HERA*, *Z. Phys.* **C72** (1996) 637–646. Cited at pages 48, 49.

[95] T. Binoth, G. Ossola, C. Papadopoulos, and R. Pittau, *NLO QCD corrections to tri-boson production*, *JHEP* **0806** (2008) 082. Cited at page 49.

[96] H.-L. Lai, M. Guzzi, J. Huston, Z. Li, P. M. Nadolsky, et al., *New parton distributions for collider physics*, *Phys. Rev.* **D82** (2010) 074024. Cited at pages 49, 89.

[97] P. M. Nadolsky et al., *Implications of CTEQ global analysis for collider observables*, *Phys. Rev.* **D78** (2008) 013004, [arXiv:0802.0007]. Cited at page 49.

[98] A. Sherstnev and R. S. Thorne, *Parton distributions for the LHC*, *Eur. Phys. J* **C55** (2009) 553. Cited at pages 49, 89.

[99] ATLAS Collaboration, *Search for the Standard Model Higgs boson in the $H \to WW^{(*)} \to \ell\nu\ell\nu$ decay mode using 1.7 fb^{-1} of data collected with the ATLAS detector at $\sqrt{s} = 7\,TeV$*, ATLAS-CONF-2011-134. Cited at page 49.

[100] ATLAS Collaboration, *The ATLAS Simulation Infrastructure*, *Eur. Phys. J.* **C70** (2010) 823–874. Cited at page 49.

[101] S. Agostinelli et al., *GEANT4: A Simulation toolkit*, *Nucl.Instrum.Meth.* **A506** (2003) 250–303. Cited at page 49.

[102] ATLAS Collaboration, *The simulation principle and performance of the ATLAS fast calorimeter simulation FastCaloSim*, ATL-PHYS-PUB-2010-013. Cited at page 49.

[103] T. Sjostrand, S. Mrenna, and P. Z. Skands, *PYTHIA 6.4 Physics and Manual*, *JHEP* **05** (2006) 026, [hep-ph/0603175]. Cited at page 50.

[104] P. Nason, *A New method for combining NLO QCD with shower Monte Carlo algorithms*, *JHEP* **11** (2004) 040, [hep-ph/0409146]. Cited at page 50.

[105] S. Frixione and B. R. Webber, *Matching NLO QCD computations and parton shower simulations*, *JHEP* **06** (2002) 029, [hep-ph/0204244]. Cited at page 50.

[106] S. Alioli, P. Nason, C. Oleari, and E. Re, *A general framework for implementing NLO calculations in shower Monte Carlo programs: the POWHEG BOX*, *JHEP* **06** (2010) 043, [arXiv:1002.2581]. Cited at page 50.

[107] E. Bagnaschi, G. Degrassi, P. Slavich, and A. Vicini, *Higgs production via gluon fusion in the POWHEG approach in the SM and in the MSSM*, *JHEP* **02** (2012) 088, [arXiv:1111.2854]. Cited at page 50.

[108] P. Nason and C. Oleari, *NLO Higgs boson production via vector-boson fusion matched with shower in POWHEG*, *JHEP* **02** (2010) 037, [arXiv:0911.5299]. Cited at page 50.

[109] S. Frixione, P. Nason, and G. Ridolfi, *A Positive-weight next-to-leading-order Monte Carlo for heavy flavour hadroproduction*, *JHEP* **09** (2007) 126, [arXiv:0707.3088]. Cited at page 50.

[110] S. Alioli, P. Nason, C. Oleari, and E. Re, *NLO single-top production matched with shower in POWHEG: s- and t-channel contributions*, *JHEP* **09** (2009) 111, [arXiv:0907.4076]. [Erratum: JHEP02,011(2010)]. Cited at page 50.

[111] E. Re, *Single-top Wt-channel production matched with parton showers using the POWHEG method*, *Eur. Phys. J.* **C71** (2011) 1547, [arXiv:1009.2450]. Cited at page 50.

[112] T. Melia, P. Nason, R. Rontsch, and G. Zanderighi, *W+W-, WZ and ZZ production in the POWHEG BOX*, *JHEP* **11** (2011) 078, [arXiv:1107.5051]. Cited at page 50.

[113] I. Chakravarti, R. Laha, and J. Roy, *Handbook of methods of applied statistics*. No. v. 1 in Wiley series in probability and mathematical statistics. Wiley, 1967. Cited at pages 52, 62.

[114] A. Hocker et al., *TMVA - Toolkit for Multivariate Data Analysis*, *PoS* **ACAT** (2007) 040 CERN-OPEN-2007-007, [physics/0703039]. Cited at pages 61, 62, 63, 114, 115.

[115] ATLAS Collaboration, *Evidence for the spin-0 nature of the Higgs boson using ATLAS data*, *Phys. Lett.* **B726** (2013) 120–144. Cited at page 62.

[116] ATLAS Collaboration, *Jet energy scale and its systematic uncertainty in proton-proton collisions at sqrt(s)=7 TeV with ATLAS 2011 data*, ATLAS-CONF-2013-004. Cited at page 86.

[117] ATLAS Collaboration, *Measurement of the b-tag Efficiency in a Sample of Jets Containing Muons with 5 fb-1 of Data from the ATLAS Detector*, ATLAS-CONF-2012-043. Cited at page 86.

[118] ATLAS Collaboration, *b-jet tagging calibration on c-jets containing D^{*+} mesons*, ATLAS-CONF-2012-039. Cited at page 87.

[119] ATLAS Collaboration, *Measurement of the Mistag Rate with 5 fb^{-1} of Data Collected by the ATLAS Detector*, ATLAS-CONF-2012-040. Cited at page 87.

[120] ATLAS Collaboration, *Improved luminosity determination in pp collisions at $\sqrt{s}$ = 7 TeV using the ATLAS detector at the LHC*, *Eur. Phys. J.* **C73** (2013) 2518. Cited at page 87.

[121] ATLAS Collaboration, *Jet energy resolution in proton-proton collisions at $\sqrt{s} = 7$ TeV recorded in 2010 with the ATLAS detector*, *Eur. Phys. J.* **C73** (2013), no. 3 2306, [arXiv:1210.6210]. Cited at page 92.

[122] ATLAS Collaboration, *Jet energy measurement with the ATLAS detector in proton-proton collisions at $\sqrt{s} = 7$ TeV*, *Eur. Phys. J.* **C73** (2013), no. 3 2304, [arXiv:1112.6426]. Cited at page 92.

[123] ATLAS Collaboration, *Measurement of the Higgs boson mass from the $H \to \gamma\gamma$ and $H \to ZZ^* \to 4\ell$ channels with the ATLAS detector using 25 fb^{-1} of pp collision data*, *Phys.Rev.* **D90** (2014), no. 5 052004, [arXiv:1406.3827]. Cited at page 99.

[124] ATLAS Collaboration, *ATLAS Insertable B-Layer Technical Design Report*, Tech. Rep. CERN-LHCC-2010-013. ATLAS-TDR-19, CERN, Geneva, Sep, 2010. Cited at page 106.

[125] ATLAS Collaboration, *Expected performance of the ATLAS b-tagging algorithms in Run-2*, Tech. Rep. ATL-PHYS-PUB-2015-022, CERN, Geneva, Jul, 2015. Cited at page 108.

[126] ATLAS Collaboration, *Commissioning of the ATLAS b-tagging algorithms using $t\bar{t}$ events in early Run-2 data*, Tech. Rep. ATL-PHYS-PUB-2015-039, CERN, Geneva, Aug, 2015. Cited at page 108.

[127] ATLAS Collaboration, *Properties of Jets and Inputs to Jet Reconstruction and Calibration with the ATLAS Detector Using Proton-Proton Collisions at $\sqrt{s} = 13$ TeV*, Tech. Rep. ATL-PHYS-PUB-2015-036, CERN, Geneva, Aug, 2015. Cited at page 108.

[128] ATLAS Collaboration, *A neural network clustering algorithm for the ATLAS silicon pixel detector*, *JINST* **9** (2014) P09009, [arXiv:1406.7690]. Cited at page 108.

[129] ATLAS Collaboration, *Expected performance of missing transverse momentum reconstruction for the ATLAS detector at $\sqrt{s} = 13$ TeV*, Tech. Rep. ATL-PHYS-PUB-2015-023, CERN, Geneva, Jul, 2015. Cited at page 108.

[130] G. Luisoni, P. Nason, C. Oleari, and F. Tramontano, *$HW^{\pm}/HZ$ + 0 and 1 jet at NLO with the POWHEG BOX interfaced to GoSam and their merging within MiNLO*, *JHEP* **10** (2013) 083, [arXiv:1306.2542]. Cited at page 108.

[131] ATLAS Collaboration, *Measurements of the Higgs boson production and decay rates and coupling strengths using pp collision data at $\sqrt{s}$ = 7 and 8 TeV in the ATLAS experiment*, ATLAS-CONF-2015-007. Cited at page 111.

[132] P. C. Bhat, *Multivariate analysis methods in particle physics*, *Annual Review of Nuclear and Particle Science* **61** (2011), no. 1 281–309. Cited at pages 112, 113, 114.

[133] B. P. Roe, H.-J. Yang, J. Zhu, Y. Liu, I. Stancu, and G. McGregor, *Boosted decision trees as an alternative to artificial neural networks for particle identification*, *Nuclear Instruments and Methods in Physics Research A* **543** (May, 2005) 577–584, [physics/0408124]. Cited at pages 112, 114, 115, 116.

[134] W.-Y. Loh, *Classification and regression trees*, *Wiley Interdisciplinary Reviews: Data Mining and Knowledge Discovery* **1** (2011), no. 1 14–23. Cited at page 112.

[135] M. Delmastro, "Web Page: *Borborigmi di un fisico renitente.*" `http://www.borborigmi.org/2015/07/23/`, 2015. No citations.